Winter 2021

THE APPLICATION OF IRON-BASED MATERIALS IN AQUEOUS ENERGY STORAGE

Fenghua Guo
University of New Hampshire

THE APPLICATION OF IRON-BASED MATERIALS IN AQUEOUS ENERGY STORAGE

By

FENGHUA GUO

Baccalaureate Degree, Chemical Engineering and Technology, China University of Mining and Technology-Beijing, Beijing, China, 2013

Master's Degree, Chemical Technology, China University of Mining and Technology-Beijing, Beijing, China, 2016

DISSERTATION

Submitted to the University of New Hampshire

in Partial Fulfillment of the Requirements for the Degree of

Doctor of Philosophy

in

Chemical Engineering

December 2021

This dissertation was examined and approved in partial fulfillment of the requirements for the degree of Doctor of Philosophy in Chemical Engineering by:

Dissertation Director, Dr. Xiaowei Teng,
Professor and Chair of Chemical Engineering, University of New Hampshire

Dr. Nivedita Gupta,
Professor of Chemical Engineering, University of New Hampshire

Dr. Young Jo Kim,
Assistant Professor of Chemical Engineering, University of New Hampshire

Dr. Gonghu Li,
Professor of Chemistry, University of New Hampshire

Dr. Rudi Seitz,
Professor of Chemistry, University of New Hampshire

On

October 7th, 2021

Approval signatures are on file with the University of New Hampshire Graduate School.

Table of Contents

ACKNOWLEDGEMENTS

It is my great pleasure to express my sincere gratitude to my advisor, Dr. Xiaowei Teng. His support is essential for me to complete my dissertation. It was always intriguing to discuss with Dr. Teng about the challenges and difficulties I have faced during the past five years. His tremendous passion for research has been very inspiring. Although my study as a Ph.D. student is concluding, I am sure that I can always learn from him moving forward.

I would also like to thank the rest of my committee members: Dr. Nivedita Gupta, Dr. Young Jo Kim, Dr. Gonghu Li, and Dr. Rudi Seitz. I appreciate their efforts and support for the completion of my dissertation.

It is my previlige to receive funding from multiple sources to support my research, including the teaching assistantship from the Department of Chemical Engineering, research assistantship supported by U,S. Depaertment of Energy under Award DE-SC0018922, as well as the Dissertation Year Fellowship fron the Graduate School.

Special thanks to the technical support from Beamline 28-ID-1of the National Synchrotron Light Source II for XRD measurements, and from the University Instrument Center at the University of New Hampshire for XPS and SEM measurements.

It has been a pleasure to work with the other members of Dr. Teng's research team. Thank you to Dr. Guangxing Yang, Dr. Xiaoqiang Shan, Dr. Daniel Charles, Tongxin Zhou, SaeWon Kim, and Sathya Narayanan Jagadeesan.

Thank you to my friends who care about me and whom I care about. It hasn't been easy, but I am glad that I have had their support all through the years.

Finally, I would like to thank my father, Yu Guo, and my mother, Shouyun Li. The best thing ever happened to me was being born to be their son. I know I always have their support. Their unconditional love enlightens the way forward for me.

LIST OF TABLES

LIST OF FIGURES

ABSTRACT

THE APPLICATION OF IRON-BASED MATERIALS IN AQUEOUS ENERGY STORAGE

By

Fenghua Guo

University of New Hampshire, December 2021

Aqueous energy storage has been an important part of battery research for its cost-effective, environmentally benign, and robust nature. Iron-based materials, including iron hydroxides and iron oxides, are widely investigated as electrode materials for their extremely low cost and sufficient discharge capacity. Iron-based electrode materials were often operated in strong alkaline electrolytes, experiencing either slow reaction kinetics, severe side reactions, or significant capacity loss over cycling. This research focused on the application of iron-based materials in aqueous electrolytes with low alkalinity.

This research showed that the synthesized γ-FeOOH measured with a cocktail electrolyte of sodium sulfate and sodium hydroxide demonstrated an enhanced discharge capacity and improved capacity retention, compared with the results measured in sodium hydroxide electrolyte. The investigation on the charge storage mechanism using *in-situ* XRD, XPS, as well as electrochemical methods showed that a green rust phase formed in the discharge stage in the

cocktail electrolyte played an important role in the enhancing of electrochemical performance of γ-FeOOH, promoting Fe^{2+}/Fe^{3+} one-electron transfer reaction with an enhanced capacity. The green rust phase also reduced the formation of the electrochemically inert Fe_3O_4 phase during the discharge process, promoting cycling performance. This research on the performance of iron-based materials in cocktail electrolytes opens up a new field in utilizing iron-based materials for aqueous battery applications.

CHAPTER 1 INTRODUCTION

1.1 THE DEVELOPMENT OF BATTERY

The battery has been an important part of human society ever since its invention, and considerable developments in battery materials have been made over the years. The first electric battery was the *Volta Pile*, invented by *Alessandro Volta* in 1798.[1] Several types of batteries made their way into wide applications, including the Lead-Acid battery invented by *G. Planté* in 1859 and the Nickel-Iron battery developed initially in 1901 by *Thomas Edison* and *Jünger*.[2-4] With the wide-growing applications of portable electronics and electric vehicles in the past few decades, there has been an increasing demand for high-performance batteries. Since Sony developed the first commercial lithium-ion batteries in 1991, lithium-ion batteries have been widely used for their high volumetric energy cyclability.[5-8]

The demand for high-performance batteries is also increasing with the development of renewable energy. **Figure 1.1** shows that fossil fuels still contribute to most energy consumption; however, the amount of renewable energy production increases over the years. On the other hand, it is of vital importance to couple energy storage systems with electricity generation from renewable sources, such as solar and wind, for their intermittent nature.[9-12] Moreover, with smart grid systems, it is critical to managing electricity production to better accommodate ever-changing electricity consumption. Therefore, one of the approaches a modern grid system adopts is to couple the renewable energy generation with the energy storage system, accommodating the mismatch between electricity consumption and production.[13,14]

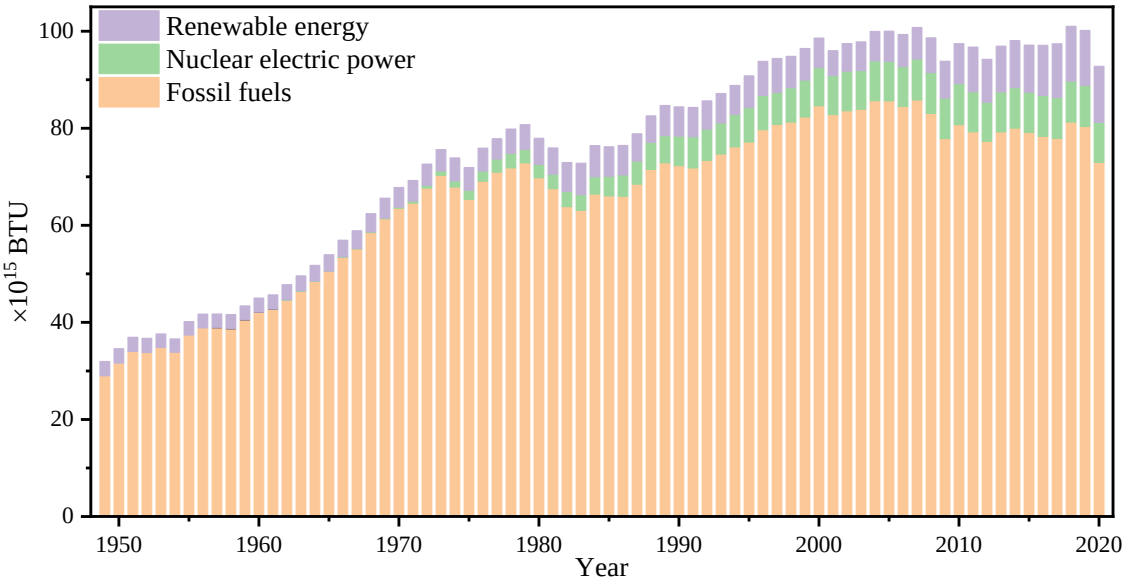

Figure 1.1 Primary energy consumption in the United States, 1949 to 2020 (source: U.S. Energy Information Administration).[15]

Intensive research efforts have been focused on nearly every aspect of a battery system to enhance its performance. These efforts include a better understanding of the fundamental electrochemical chemistry, finding new electrolytes with wide and stable potential window, and new types of electrode materials with enhanced redox activity and stability.[16-19]

1.2 MECHANISM OF A BATTERY SYSTEM

An electric battery is a device that can transform chemical energy into electrical energy upon discharging. Some of the batteries can also reversely transform electrical energy into chemical energy during the charging process. The battery was first invented by *Alessandro Volta* in 1798. In the famous *Volta Pile*, layers of zinc metal and copper were separated by cloth soaked with saltwater. The *Volta Pile* contains all the major parts of a battery: electrolyte and electrodes (including anode and cathode). The saltwater served as the electrolyte, the zinc electrode as the anode, and the copper as the cathode. *John Frederic Daniell* modified the *Volta Pile* later to

avoid gas formation on the cathode in 1836, which led to the invention of the *Daniell cell*.[20] Battery reaction involves electron transfer. But unlike a typical redox reaction where the oxidant is in direct contact with the reductant and receives the electrons from the reductant, in a battery system, the redox reaction was 'separated' into two half-reactions to occur on each electrode respectively, as shown in Equations 1.1, 1.2 and 1.3, as well as in **Figure 1.2** for a typical Zn-Cu battery.

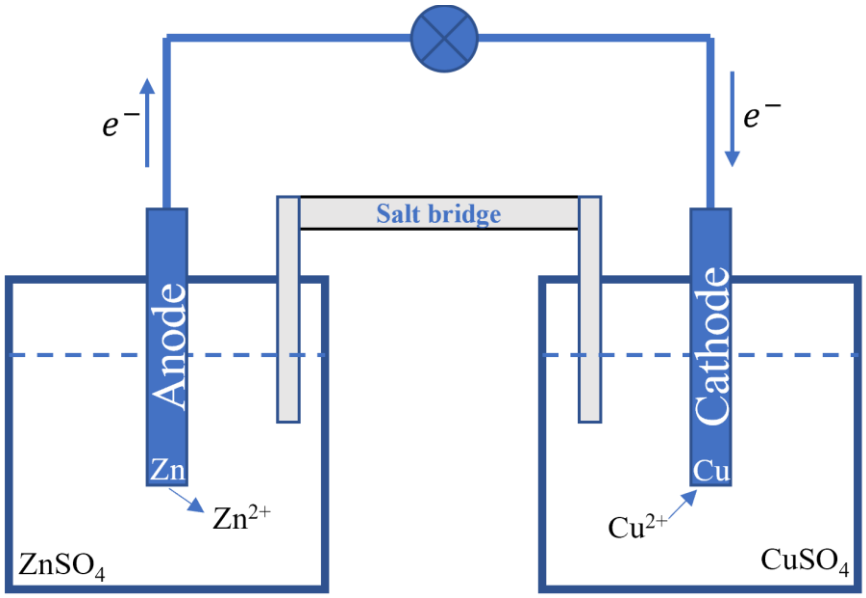

Figure 1.2 Scheme of a typical Zn-Cu battery.

Figure 1.2 shows that the electrons were transferred through an external circuit (*e.g.*, copper wire), and the charge was balanced by the ion transfer between the electrodes and electrolyte, as well as the transport of ions within the electrolyte. Ideally, the electrolyte should only support ionic transport and separate the two electrodes as an electronic insulator.

Anode: $Zn(s) \rightarrow Zn^{2+}(aq) + 2e^-$ Equation 1.1

Cathode: $Cu^{2+}(aq) + 2e^- \rightarrow Cu(s)$ Equation 1.2

Overall: $Zn(s) + Cu^{2+}(aq) \rightarrow Cu(s) + Zn^{2+}(aq)$ Equation 1.3

The overall cell reaction can be derived by combing two half-reactions. The standard electrode potential of each half-reaction and the overall reaction is an intrinsic thermodynamic property and can be calculated from the standard *Gibbs* free energy of the related cell reaction by Equation 1.4:

$$E^0_{Cell} = \frac{\Delta G^0_{Cell}}{-nF}$$ Equation 1.4

in which *n* is the charge transfer number, *F* is the Faradic constant (96485 Coulomb/mol). Since the *Gibbs* free energy at non-standard conditions can be calculated by Equation 1.5, the potential at different temperatures, pressure, and concentrations can thus be calculated by Equation 1.6 (the *Nernst* equation).

$$\Delta G = \Delta G^{\ominus} + RTlnQ_r$$ Equation 1.5

$$E_{Cell} = E^{\ominus}_{Cell} - \frac{RT}{nF} lnQ_r$$ Equation 1.6

in which *T* is the temperature in *Kelvin*, and Q_r is the reaction quotient. It is worth mentioning that the reaction involved within the *Volta Pile* is irreversible. Once the discharge process is completed, the electrode materials will be consumed, and the battery will not be re-charged. The non-rechargeable battery is categorized as a primary battery, while the secondary battery refers to rechargeable batteries, as the electrochemical reactions are reversible to allow the charging and discharging processes. Both primary and secondary batteries have significant applications in modern life. Primary batteries are popular for occasions when recharging is not necessary or challenging, such as implantable cardioverter defibrillator.[21] Secondary batteries are preferred for many other applications such as electric vehicles and portable electronic devices.

Notably, the standard cell potential at which the redox reactions happen can be calculated by reaction *Gibbs* free energy, as it is equilibrium potential. However, the potential at which a reaction practically happens is different from the equilibrium potential. The difference is called overpotential, which determines reaction kinetics by the *Butler-Volmer* equation (Equation 1.7).[22,23]

$$i = i_0 \cdot \left\{ \exp\left(\frac{\alpha_a F \eta}{RT}\right) - \exp\left(-\frac{\alpha_c F \eta}{RT}\right) \right\} \qquad \text{Equation 1.7}$$

where i is the generated current, i_0 is the exchange current, η is the difference between applied potential and equilibrium potential, α_a is the dimensionless anodic charge transfer coefficient, α_c is the dimensionless cathodic charge transfer coefficient, *F* is the Faradic constant, *R* is the gas constant, and *T* is the temperature in *Kelvin*. The reaction kinetics of an electrochemical reaction affect the reaction rates. A fast electrochemical reaction usually yields a high power density of a battery, but it also requires a high overpotential. Requirements on batteries are different depending on their applications, but in general, higher energy density, power density, and better cycle life are highly desired.[24] Therefore, tremendous efforts have been devoted to these goals, especially on developing electrolytes and electrodes.[25-27]

1.2.1 ADVANCES IN THE UNDERSTANDING OF REACTION MECHANISM

1.2.1.1 PHASE TRANSITION IN A REDOX REACTION

Fast reaction kinetics is critical for a battery's practical application. Phase changes, namely, whether or not the electrochemical reaction would cause structural changes within the electrode materials, are among the most important characteristics that would impact the reaction mechanism. With the development in material characterization techniques, especially the

development in crystallography with the wide application of X-ray diffraction, researchers can look more in detail at how the structure changes while the electrochemical reaction proceeds.

The redox reactions in the early batteries, such as the lead-acid battery and the nickel-iron battery, often involved irreversible phase changes during the conversion from the reactants to the electrochemical products. For example, in the Nickel-iron (Ni-Fe) battery, the reaction on the Fe anode during discharging involves the oxidation of a body-centered cubic metallic iron to layered $Fe(OH)_2$, as described by Equation 1.8.

$$Fe + 2OH^- \rightarrow Fe(OH)_2 + 2e^- \qquad \text{Equation 1.8}$$

This so-called conversion-type of electrochemical reaction usually has slow reaction kinetics and poor reversibility due to its large energy barrier for the phase transition and slow ion diffusion within the electrode particle. As described in previous work, a typical battery reaction that involves phase change usually results in sharp redox peaks in a cyclic voltammetry measurement or a long discharge plateau in a chronopotentiometry measurement.[28] On the other hand, the conversion-type of electrochemical reactions generally results in high energy density.

Over the past few decades, researchers have been devoted to the insertion-type of electrochemical reaction, in which the electrode material can host the insertion/extraction of ions without changing its crystal structure (no phase transition). Materials with a layered structure are among the most studied insertion-type of electrode materials, as shown in **Figure 1.3**. Graphite is a typical layered material, which is still used in Lithium-ion batteries.[29] Usually, the layered materials have a relatively large interlayer distance, and their molecular layers are held together by *van der Waals* force. Thus, the electrochemical reaction is fulfilled by the reversible insertion/extraction of ions at the interlayer space without destroying the layer structure.

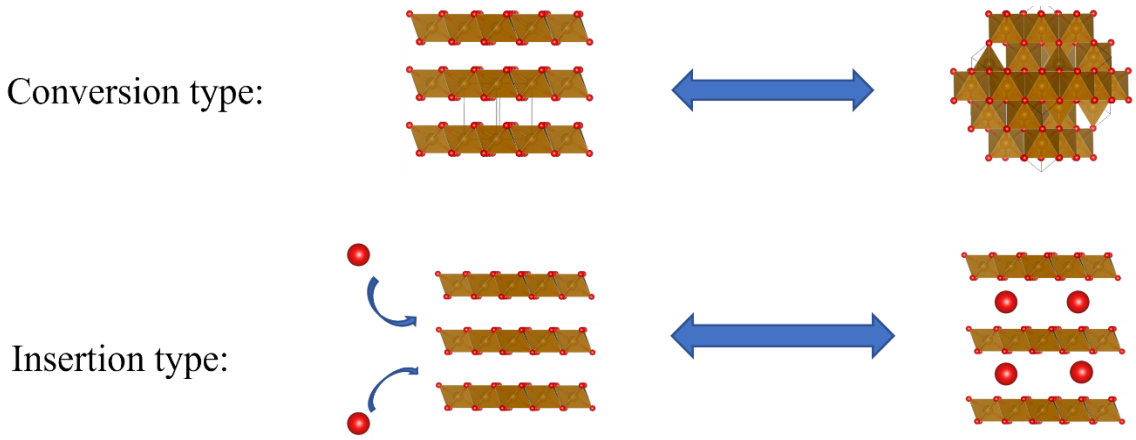

Figure 1.3 Illustration of conversion type and insertion type of reaction mechanism.

The distance between adjacent layers would be altered during the redox reaction (insertion and extraction of ions), but the main structure would still be maintained. Since there are no drastic phase changes and the ions would only have coulombic interactions instead of chemical bonding with the intra-layer atoms, electrochemical reactions with layered structure materials usually have relatively fast kinetics and better reversibility.[30,31]

Notably, although materials with a layer structure are the most used materials for the insertion-type of reaction, a layer structure is not a requirement for the insertion-type of reaction. Some other materials with large cavities in the structure could also host the insertion and extraction of ions, such as $LiFePO_4$ with an ordered olivine structure, which will be discussed later in this chapter (**Section 1.3.3**).[32] Other layered materials that have been widely investigated include layered transition metal oxides and layered double hydroxides.[30]

1.2.1.2 ION SIZE IN A REDOX REACTION

On the other hand, it is also beneficial to have inserted ions with smaller size, as in theory, it would cause few structural changes to the host materials. Lithium-ion batteries have been popularly investigated and commercially applied because lithium-ion has the smallest radius of

all metal ions. However, in aqueous electrolytes, metal ions usually accompany several water molecules, also known as hydration. Even though the lithium-ion is smaller than the sodium ion or potassium ion, it is more strongly hydrated with water molecules and thus possesses a larger hydrated radius (Stockes radius) than Na^+ and K^+ ions.[33,34] Thus, it is expected that sodium ions or potassium ions are used as intercalated ions in aqueous systems.

One challenge with the application of Lithium-ion batteries is the uneven distribution of lithium reserves around the globe and the high price, limiting its application in energy storage devices. Therefore, researchers have been studying Na^+ and K^+ charge carriers over the years, even for non-aqueous energy storage systems.[35,36] Although Na^+ and K^+ have significantly larger radii than Li^+, as shown in **Table 1.1**, and are also heavier in atom weight, it is still beneficial in terms of cost, especially for large-scale energy storage devices.

Table 1.1 Radius of different ions.

Ion	Li^+	Na^+	K^+	Cl^-	SO_4^{2-}
Radius (Å)	0.76[37]	1.06[37]	1.64[38]	1.81[39]	2.15[39]

Notably, anions are generally not considered ideal for the insertion-type of electrochemical reactions because anions typically have large radii (**Table 1.1**) compared to cations. However, the application of layered materials with large interlayer spacing in anion-intercalation batteries is also being investigated, especially in chloride-ion batteries (CIB). It is also worth mentioning that although insertion-type of materials are getting popular over the years for the merits mentioned previously, the drawbacks are also apparent: the insertion-type of battery materials typically have a smaller capacity compared with conversion-type of batteries, as the redox reaction are usually not complete.

1.2.1.3 PARTICLE MORPHOLOGY IN REDOX REACTION

Another essential factor that can affect the reaction kinetics is the morphology of the electrode particle, particularly the particle size. The reaction kinetics also can be improved mainly by reducing the diffusion length for ions during an electrochemical reaction. With the development in imaging techniques, especially the wide application of electron microscopy, researchers could better control the morphology of the materials. Whether the electrode materials go through an insertion- or conversion-type of reaction, the ion transport between the electrode and electrolyte interface is inevitable, and the ion diffusion within the particle was often the rate-limiting step. In general, a shorter diffusion length for the ions in the particles would result in better reaction kinetics. Therefore, nano-sized electrode materials have been heavily investigated for their improved transport properties during battery reactions.[40,41]

The control of particle morphology goes beyond particle size. Efforts have been made on synthesizing materials with different morphologies such as 2D nanosheets and hollow nanostructure. 2D nanosheets are beneficial in many different ways, especially for their large specific surface area, which favors fast reaction kinetics.[42,43] Hollow nanostructure also results in a large surface area and short diffusion length.[44]

1.2.1.4 PSEUDO CAPACITANCE IN REDOX REACTION

It is worth mentioning that with the wide application of nano-sized electrode materials and materials that could have fast reaction kinetics, supercapacitors have become a new type of electrochemical energy storage device that emerges over the years.[45,46] In a supercapacitor, also called a pseudo capacitor, charges are stored at the electrode surface with a much faster electrochemical reaction rate than traditional batteries where the charges are stored mainly inside the particles. On the other hand, the capacity of supercapacitors is still higher than traditional

capacitors, where the charges are only absorbed in the surface via a non-Faradic process (double-layer capacitance). Notably, both supercapacitor and capacitor show a linear relationship between the capacity and applied potential, while their charge storage mechanisms are not identical.[47,48]

1.2.2 ADVANCES IN THE UNDERSTANDING OF THE ROLE OF ELECTROLYTES

Electrolytes are an essential part of a battery system, serving as the host for the charge carriers and allowing ionic transport between the cathode and the anode. An electrolyte should also be an electronic insulator to avoid shorting.

Another critical feature of an electrolyte is its stable potential window. A battery should be operated within the stable potential window of the electrolyte to avoid the continuous decomposition of the electrolyte. Therefore, the potential window of the electrolyte often determines the potential window of an electrochemical device, influencing the energy density of the device (Equation 1.9),

$$E = \frac{1}{2} \times C \times \frac{(\Delta V)^2}{3600} \qquad \text{Equation 1.9}$$

where C is the volumetric capacitance, and ΔV is the potential window.[49,50] The potential window of water-based electrolytes is usually limited by the stable potential window of water, which is 1.23 V according to the Pourbaix Phase Diagram of the water.[51] Researchers have been investigating different types of electrolytes over the years to develop electrolytes with a large stable potential window.[52-54]

1.2.2.1 LIQUID ELECTROLYTES

Liquid electrolytes have a long history of applications in batteries. Typically, the electrolyte consists of solvent and salt. Depending on the solvent, the electrolyte can be categorized as an aqueous electrolyte where the solvent is water or an organic liquid electrolyte where the solvent is one or more kinds of organic compounds.

AQUEOUS ELECTROLYTES

Aqueous electrolyte refers to electrolytes that use water as solvent. Aqueous electrolytes have been utilized since the *Volta Pile*, in which saltwater is used as an electrolyte. The lead-acid battery was the first rechargeable aqueous battery invented by *G. Planté* in 1859, of which the electrolyte was sulfuric acid. The famous Nickel-Iron Battery developed by *Thomas Edison* and *Jünger* in 1901 used potassium hydroxide solution as an electrolyte. Aqueous electrolytes have been widely used since the early stage of battery application, as they are generally environmentally friendly, cost-effective, relatively easy to produce, and of high ionic conductivity.

Despite the merits, aqueous energy storage devices have some limitations that bottleneck their application. The thermodynamically stable potential window for water is only 1.23 V, beyond which the gas evolution reaction described by Equations 1.10 and 1.11 (Alkaline environment) would happen. The limited operational potential window of aqueous energy storage devices results in a relatively low energy density, limiting their applications in the fields where high energy density is critical.

$$4OH^- \rightarrow O_2 + 2H_2O + 4e^- \qquad \text{Equation 1.10}$$

$$E_0 = 1.23 - 0.0591 \cdot pH$$

$$4H_2O + 4e^- \rightarrow 2H_2 + 4OH^-$$ Equation 1.11

$$E_0 = -0.0591 \cdot pH$$

There have been great efforts to extend the potential window in aqueous energy storage. An easy way to avoid the gas evolution reaction is to change the pH of the electrolyte.[55,56] In some cases where hydrogen evolution reaction (HER) is the limiting side reaction, it usually is beneficial to increase the pH so the HER could be suppressed to a lower potential. But this method would not enlarge the potential window since the oxygen evolution reaction would be shifted to a lower potential at the same time as described by Equation 1.10, and the potential window remains at 1.23 V. Notably, the practical potential window of an aqueous electrochemical device is usually higher than the equilibrium potential window of water (1.23 V) since overpotential is always incurred to the electrochemical reactions when the reaction proceeds under off-equilibrium conditions.

Besides pH, recent efforts have been devoted to developing the kinetically inert interphase to gas evolution reactions at electrode and electrolyte interface. *Shan*'s work showed that hydroxylated interphase formed on the Mn_5O_8 electrode surface upon the interaction between water and Mn^{2+} components during the electrochemical cycling. Such interphase significantly increases the energy barrier for water decomposition and results in a stable potential window of 2.5 V in a half-cell reaction.[57]

Another approach to expand the aqueous potential window is to develop new types of aqueous electrolytes. Recently, researchers found that aqueous electrolytes with an extremely high concentration of salts exhibited a much-enlarged stable potential window. *Suo*'s initiative work on the 'water-in-salt' system showed that the potential window could be expanded to ~3.0 V by

the formation of a solid-electrolyte interphase (SEI) and reduced activity of water in a highly concentrated aqueous electrolyte (> 20 M of lithium bis(trifluoromethane sulfonyl)imide), which is a considerable improvement comparing with the 1.23 V stable potential window of water.[52]

ORGANIC LIQUID ELECTROLYTES

Some electrolytes using organic solvents could offer a potential window over 3.0 V due to their stable chemical properties under a high electric field.[58] One of the most commonly used salts in organic electrolytes for lithium-ion batteries is Lithium Hexafluorophosphate ($LiPF_6$).[59] Notably, an SEI layer would form in the presence of organic electrolytes after the initial cycle at the surface of the anode, protecting the electrolyte from further decomposition.[59,60] SEI formation plays an important role in the properties of a battery, especially cyclability and columbic efficiency. The challenge of lithium metal as an anode is lithium dendrites formation that would damage the SEI layer.[61,62] Many researchers have been working on a better understanding of the SEI layer.[60, 63-65] In general, the SEI layer was formed with the decomposition product of the solvent and the salts. The layer is an electrical insulator that can block the solvent molecules from contacting the electrode to permit lithium-ion transport.

The higher energy density batteries with organic electrolytes are popularly used in portable electronic devices, such as cell phones and laptops, where high volumetric energy density is critical. However, despite the wide potential window and high energy density that organic electrolytes provide, their drawbacks include their high cost and flammable and toxic nature.

1.2.2.2 SOLID-STATE ELECTROLYTES

Besides liquid electrolytes, researchers also focused on solid-state electrolytes, which are less flammable and could handle a much larger potential window than the organic electrolyte.

Similar to liquid electrolytes, solid-state electrolytes are ionic conductors and electronic insulators and can facilitate the transport of charge carriers between anode and cathode. Solid-state ionic conductors were discovered in the 19th century, and their first application as a solid-state electrolyte was in 1960s.[66] It is worth mentioning that when the solid-state electrolytes are employed in a battery device, a separator that is commonly required in liquid electrolytes is no longer needed because solid-state electrolytes can also serve as separators.

While a solid-state electrolyte offers a large potential window, its ionic conductivity is generally inferior to liquid electrolytes since the ions are more 'confined' in the solid-state. Many efforts have been reported on improving the ionic conductivity of solid-state electrolytes, where a plausible ionic conductivity in the range of 10^{-3} S cm^{-1} is achieved. Such performance is close to the typical ionic conductivity of organic liquid electrolytes (around 10^{-2} S cm^{-1}).[67,68]

In summary, understanding how electrolytes interact with electrodes helps discover new types of electrolytes that are stable over a wide potential window and ionically conductive. As a result, novel electrolyte systems improve the electrochemical performance of the existing battery materials and allow more materials to be used as battery electrodes if their redox potentials fall into a more expanded potential window.

1.2.3 ADVANCES IN THE DESIGNING OF ELECTRODE MATERIALS

Electrode materials play a vital role in the storage capacity, cycle life, and coulombic efficiency of a battery device. With a more thorough understanding of reaction mechanisms, researchers have been making progress in finding and designing battery materials that have a higher energy density, higher power density, and improved cyclability.

1.2.3.1 CATHODE MATERIALS

The performance of a battery device is often bottlenecked by the lack of high-capacity transition metal oxide cathode materials because anode materials, such as lithium metal or graphite, usually possess a much higher storage capacity than cathode counterparts. Transition metal-based materials are among the most studied cathode materials due to their multiple valence states during the redox reactions. For example, $Mn^{2+}/Mn^{3+}/Mn^{4+}$ are the typical valence states for Mn-based materials, and the chemistry caused by the insertion/extraction of Li^+ with spinel Mn_3O_4 is the redox couple between Mn^{2+} and Mn^{3+}, the insertion /extraction of Li^+ with layered α-MnO_2 was accompanied with the redox couple between Mn^{3+} and Mn^{4+}. Most transition metals also have a large abundance, as iron and magnesium have 4.7% and 1.9% in the earth's crust, respectively. Many transition metal elements, particularly iron and manganese, have low toxicity and are environmentally benign.[69]

Over the past few decades, with the tremendous development in the lithium-ion battery, many transition metal oxides and hydroxides with the layered structures have been extensively studied, including δ-MnO_2, layered V_2O_5, and layered double hydroxide (LDH).[70-73] δ-MnO_2 has an interlayer spacing of around 7 Å, while interlayer spacing for V_2O_5 is as high as 11.5 Å, and can be further enlarged by additional intercalation of water molecules and even organic molecules.[74-76] The weak Van der Waals forces between the adjacent 2D layers and the large interlayer spacing are ideal for ion intercalation in the layered materials. On the other hand, LDHs have the general formula of $\left[M_x^{2+}N_y^{3+}(OH)_{2(x+y)}\right](A^{n-})_{y/n} \cdot mH_2O$, where M_x^{2+} and N_y^{3+} are metal ions and can be from the same species. A^{n-} are the anion groups that reside between the hydroxide layers and neutralize the positive charged hydroxide layers. Different from the aforementioned layered δ-MnO_2 and V_2O_5, where cation intercalation and deintercalation occur during

electrochemical reactions, LDHs are widely used as an anion host during energy storage reactions.[77,78]

A major challenge in utilizing transition metal oxides and hydroxides as battery electrodes is their intrinsic poor electric conductivity, which would result in low storage capacity and poor cyclability. Researchers have been studying different methods to improve their conductivity. The most used approach is physically mixing the transition metal oxides or hydroxides with conducting materials like active carbon. In addition, doping transition metal oxides or hydroxides with more conductive species during material synthesis is another approach to improve the conductivity of the electrode materials, such as doping Ni or Co species in the manganese- or vanadium-based oxides.[79-83] Such binary or ternary transition metal oxides or hydroxides could potentially improve the conductivity by synergistic effect.[84,85] Moreover, synthesizing materials with certain morphologies such as 1D nanowires also could improve the electronic conductivity because the bulk-like properties in the elongated direction offer a low percolation threshold for electron transport.[86] Besides the oxides, transition metal phosphides, transition metal sulfides, and transition metal nitrides have also been studied over the years for their generally better conductivity.[87-89]

1.2.3.2 ANODE MATERIALS

Graphite and lithium metal are the most used anode materials in lithium-ion batteries. Lithium metal is an ideal anode due to its low reduction potential (-3.05 V vs. SHE) among alkali metals and high theoretical capacity (3860 mAh g^{-1}).[59, 90, 91] However, the formation of Lithium dendrites is problematic, including the consumption of lithium and causing short circuits inside the battery. Layered graphite becomes a more popular anode material than lithium metal for its large surface and ability to host lithium-ions between layers, as described in Equation 1.12.[59,92]

$$C_6 + xLi^+ + xe^- \rightleftharpoons C_6Li_x$$ Equation 1.12

It is worth mentioning that great efforts have been spent on reducing the formation of lithium dendrites over the years to better utilize lithium metal as the anode.[61,93] Some researches showed that electrolytes with a high concentration of lithium salts would reduce or even eliminate the formation of lithium dendrites.[94,95] Some additives to the electrolytes, including fluoroethylene carbonate, nanodiamond, triblock polyether (Pluronic P123), and some others, also showed significant effects on reducing the formation of lithium dendrites.[96]

There also have been efforts to develop anode materials beyond lithium metal and graphite. Other carbon-based materials such as carbon nanotubes have also been investigated as anodes and showed promising performance due to their unique 1D morphology.[97] A few other materials have been investigated as the anode, including zinc and iron metals. Traditionally, Zn was used in Zn-MnO_2 primary batteries with an alkaline electrolyte due to the irreversible reactions on the manganese oxide electrodes, such as the formation of electrochemical-inert Mn_3O_4. However, in a mild acidic electrolyte, Zn^{2+} can reversibly intercalate/deintercalated in the cathode materials, making the Zn-MnO_2 battery become rechargeable where zinc metal functions as the anode. Iron-based materials were also widely used as anode both in organic electrolyte systems and aqueous systems. One of the first applications of the iron-based anode was the metallic iron used in Ni-Fe alkaline batteries because Fe/Fe^{2+} and Fe^{2+}/Fe^{3+} redox couples happen at relatively low potentials. However, it is worth mentioning that some iron-based materials can also be used as cathode materials, such as Prussian blue, which will be discussed later in this chapter (**Section 1.3.3**).

1.3 THE APPLICATION OF IRON-BASED ELECTRODE MATERIALS

Although iron is the fourth most abundant element on earth's crust and iron-based materials are also environmentally benign, there are challenges for their application as electrode material. The application of iron in Nickel-Iron alkaline batteries is a good example. First, the redox reaction between Fe^0 and Fe^{2+} involves the two-electron transfer and phase changes, which leads to intrinsically slow reaction kinetics. Secondly, the reduction potential from Fe^{2+} to Fe is very close to the hydrogen evolution reaction, which inevitably resulted in the gas formation accompanying the battery reaction when in aqueous electrolytes. Finally, like other transition-metal-based materials, iron oxides and hydroxides are in general of poor conductivity.

Over the past few decades, many works have been done on using iron-based materials as supercapacitors using Fe^{2+}/Fe^{3+} redox couple by employing a high concentration of the alkaline solution, controlling the particle morphology, or coupling iron materials with conductive substrates.[98-100] Beyond the traditional iron oxides and hydroxides, other iron-based materials have also been widely used as electrode materials, including $LiFePO_4$, as well as Prussian blue.

1.3.1 FUNDAMENTAL CHEMISTRY OF IRON IN AQUEOUS ELECTROLYTE

Better utilization of iron-based materials requires a fundamental understanding of iron-based materials' behavior in aqueous electrolytes, especially in alkaline solutions. The Pourbaix diagram of iron in **Figure 1.4** (the concentration of soluble species were assumed to be 10^{-4} M) shows that iron species are generally soluble under acidic conditions, insoluble under a neutral or basic environment, and become soluble again in highly alkaline solutions. As a result, most studies on iron battery chemistry have been conducted under basic or neutral environments. Iron can have multiple valence states, including Fe^0, Fe^{2+}, and Fe^{3+}. And the redox reaction usually

happens between Fe^0/Fe^{2+} and Fe^{2+}/Fe^{3+}. For example, as shown in Equations 1.13, 1.14, and 1.15, metallic iron can be oxidized to $Fe(OH)_2$ or to Fe_3O_4, depending on the conditions.

$$Fe + 2OH^- \rightarrow Fe(OH)_2 + 2e^- \quad \text{Equation 1.13}$$

$$E_0 = -0.047 - 0.0591pH$$

$$3Fe(OH)_2 + 2OH^- \rightarrow Fe_3O_4 + 4H_2O + 2e^- \quad \text{Equation 1.14}$$

$$E_0 = -0.197 - 0.0591pH$$

$$3Fe + 8OH^- \rightarrow Fe_3O_4 + 4H_2O + 8e^- \quad \text{Equation 1.15}$$

$$E_0 = -0.085 - 0.0591pH$$

Both $Fe(OH)_2$ and Fe_3O_4 could be further oxidized to $Fe(OH)_3$, as shown in Equations 1.16 and 1.17.

$$Fe(OH)_2 + OH^- \rightarrow Fe(OH)_3 + e^- \quad \text{Equation 1.16}$$

$$E_0 = 0.271 - 0.0591pH$$

$$Fe_3O_4 + OH^- + 4H_2O \rightarrow 3Fe(OH)_3 + e^- \quad \text{Equation 1.17}$$

$$E_0 = 1.208 - 0.0591pH$$

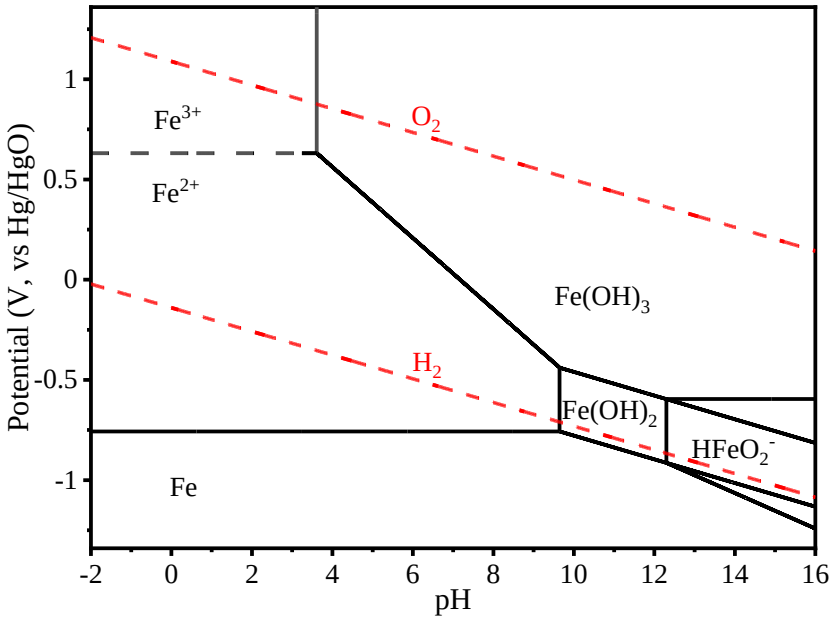

Figure 1.4 Simplified Pourbaix diagram of iron.[51]

Notably, the area between the red lines (Equations 1.10 and 1.11) is the thermodynamically stable potential window of water. As shown in Equation 1.13, metallic iron formation from the reduction of $Fe(OH)_2$ happens at a slightly lower potential than the hydrogen evolution reaction (Equation 1.11). This also explains the long-standing issues with the iron electrode, namely, the formation of iron is inevitably accompanied by hydrogen production from water reduction.

In Ni-Fe alkaline battery, the reactions at the negative terminal are dominated by Fe^0/Fe^{2+} redox couple. Although further discharging to form FeOOH is possible, Fe_3O_4 often forms following Equation 1.14. The Fe_3O_4 has a close-packed crystal structure and is electrochemically inert, lowering the cyclability of the iron anode.

Other than a pure alkaline solution, the more complicated electrolyte systems have also been studied, showing that iron-based materials undergo various redox reactions. *Genn*'s work showed different oxidization products formed in the presence of various anion groups, in which a

different intermediate species called green rust (GR) formed during the oxidization from Fe^{2+} to Fe^{3+}, as shown in Equations 1.18 and 1.19.[101]

$$6Fe(OH)_2 + SO_4^{2-} \leftrightarrow Fe_6(OH)_{12}SO_4 + 2e^- \quad \text{Equation 1.18}$$

$$E_h = -0.57 - 0.0296\log\,(SO_4^{2-})$$

$$Fe_6(OH)_{12}SO_4 + 6OH^- \leftrightarrow 6\gamma - \text{FeOOH} + SO_4^{2-} + 6H_2O + 4e^- \quad \text{Equation 1.19}$$

$$E_h = 0.59 + 0.0148\log(SO_4^{2-}) - 0.0887pH$$

GR has a layer structure where the brucite-like iron hydroxide layers are separated by the interlayer species, including water molecules and intercalated anion groups. It is an LDH, where the M_x^{3+} and N_y^{2+} are from the same metal atom. Depending on the intercalated anion groups and the corresponding difference in the structure, GR can be further categorized into GR1 and GR2.[102] GR1 refers to the green rusts where the intercalated anion groups are planar anions such as Cl^- and CO_3^{2-} and resides as one layer between the hydroxide layers, whereas GR2 refers to the green rust where the intercalated anions are non-planar anions such as SO_4^{2-} and resides as two layers between the hydroxide layers. GRs can be synthesized by the oxidization of ferrous hydroxide or the reduction of iron oxyhydroxide.[103,104] It has been used for heavy metals remediation.[105,106] But its role in energy storage has yet to be reported.

1.3.2 IRON OXIDES/HYDROXIDES

Like most transition metals, iron has multiple valance states. FeO or $Fe(OH)_2$ consists of Fe^{2+}. Fe_2O_3 or FeOOH consists of Fe^{3+}, and both Fe_2O_3 and FeOOH have multiple crystalline phases. Fe_3O_4 consists of both Fe^{2+} and Fe^{3+}. FeO/$Fe(OH)_2$ can be easily oxidized into Fe_3O_4, Fe_2O_3, or FeOOH when exposed to air, and the latter two products are relatively stable in the atmosphere.

Of the aforementioned iron oxides/hydroxides, only $Fe(OH)_2$ and γ-FeOOH had a layered structure with the layer spacing was around 5 Å. However, employing these layered materials as electrodes for intercalation charge storage reaction remains a challenge since both are less stable during the redox process. Other close-packed iron oxides/hydroxides are typically not used as insertion-type of battery materials but still commonly used in conversion-type battery reactions in aqueous and non-aqueous systems.

Iron oxides/hydroxides also face the challenge of poor electric conductivity. Combining iron oxides/hydroxides nanoparticles with more conductive materials improves electrochemical performance.[107-109] For example, *Qu*'s research showed that the specific capacitance of electrochemically obtained Fe_3O_4 grown on reduced graphene oxide (RGO) is much higher than Fe_3O_4 without RGO.[99]

1.3.3 OTHER IRON-BASED ELECTRODE MATERIALS

Iron-based materials are not limited to oxides or hydroxides. Other iron-based materials, including Prussian blue and its analogs, as well as $LiFePO_4$, are important electrode materials with more complicated crystalline structures and charge storage mechanisms.[110,111] Unlike other iron-based materials that are commonly used as anode materials, Prussian blue and $LiFePO_4$ are usually used as cathode materials.

Prussian blue has a general formula of $A_x Fe^{3+}[Fe^{2+}(CN)_6]_y \cdot \square_{1-y} \cdot zH_2O$, and with a face-centered cubic arrangement of iron atoms, where Fe^{3+} and Fe^{2+} atoms are connected by -*C*≡*N*- ligands, *A* is alkali metals reside at interstitial sites, □ represents the $Fe^{2+}(CN)_6$ vacancy sites occupied by water molecules, and H_2O is the uncoordinated interstitial water molecules.[112,113] The iron atoms can be replaced with other metal atoms to form Prussian blue analogs. Although

it did not have a layered structure, Prussian blue analogs could host charges via the intercalation storage mechanism, owing to their large spacing for alkali cations insertion. Prussian blue analogs have been studied using different intercalated ions, including Na^+ and K^+, under both aqueous and organic electrolytes. However, their battery performance is limited by poor cyclability and low coulombic efficiency, strongly related to their molecular structures. *You*'s work showed that a lower number of $Fe^{2+}(CN)_6$ vacancies in the structure would result in a much better cyclability.[112]

$LiFePO_4$ is another iron-based electrode material widely investigated and applied in industrial applications as an insertion-type of cathode material. $LiFePO_4$ has an olivine structure, where Fe atoms sit at the center of FeO_6 octahedra units, P atoms sit at the center of PO_4 tetrahedra, and Li atoms sit at the center of LiO_6 octahedra units.[114] Li atom could leave the structure with the olivine structure kept upon delithiation. Apart from the benefit of being cost-effective, $LiFePO_4$ has the advantage of a relatively stable structure, resulting from the strong bonding among oxygen, iron, and phosphorus atoms and the small volume changes of $LiFePO_4$ between the charge/discharge processes (6.77%). There are also several limitations of $LiFePO_4$, including poor electronic and ionic conductivities. Unlike layered materials that can provide a 2D diffusion pathway for lithium ions, the diffusion of lithium ions in $LiFePO_4$ can only be a 1D diffusion.[32] Researchers have minimized the diffusion limitation and improved the conductivity by reducing the particle size and coating carbon with $LiFePO_4$ particles.[115] Some researchers also tried to replace lithium-ion with sodium-ion. $NaFePO_4$ with the same olivine structures have been used in sodium-ion batteries, showing promising results.[116,117]

CHAPTER 2 EXPERIMENTAL METHODS

2.1 MATERIAL SYNTHESIS

γ-FeOOH was synthesized by a method modified from a literature-reported way.[118] 8 mL of ammonium hydroxide solution (28-30%, Certified ACS plus, Fisher Chemical) was first diluted 10 times by volume, then 8 mL of the diluted solution was continuously injected by a syringe pump (HSW Inc.) at 0.16 mL/min into a 250 mL solution of 0.01 M $FeCl_2$ (99.5%, metal basis, Alfa Aesar) and 0.1 M NaCl (≥99.5%, Sigma Aldrich), along with bubbling with compressed air. The precipitant was collected 30 min after the injection finished by centrifuging and then washed with deionized water (18.2 MΩ, Millipore, Inc.) twice and ethanol (190 Proof, ACS Grade, Pharmco) once, then vacuum dried. The vacuum product was then heated 100℃ for 3 hours under the standard atmosphere, then soaked in deionized water for one week with stirring. The product was then collected by centrifuge, washed 3 times with deionized water, and vacuum dried to get the final product.

2.2 MATERIAL CHARACTERIZATION

Multiple techniques, including Scanning Electron Microscope (SEM) and X-ray Photoelectron Spectroscopy (XPS), and X-ray diffraction (XRD) were utilized for the material characterization to have a better understanding of the morphologies, valance states, as well as the crystal structures of the materials being studied. Particularly, the application of XRD in material characterization helped researchers understand the energy storage mechanism by analyzing the crystal structure of electrode material and its evolution during electrochemical reactions. For example, XRD measurements can illustrate whether the battery reaction is a conversion- or insertion-type reaction mechanism.

Depending on the intensity of the X-ray source and the crystallinity of the target material, it takes a different amount of time for the detector to collect enough counts to generate reliable XRD patterns, usually in minutes. However, with the application of X-ray sources that can generate a high X-ray flux, it is possible to obtain high-quality XRD data within seconds. It is thus possible to collect the XRD patterns while the electrochemical reactions occurring (so-called *in-situ* measurement). *In-situ* XRD measurement is highly beneficial to understanding the reaction mechanism. Its ability to detect the unstable reaction intermediates during the redox reaction provides a leap forward in understanding reaction pathways, which wouldn't be possible by *ex-situ* measurements.

In this project, *in-situ* XRD was conducted at Beamline 28-ID-1, *National Synchrotron Light Source II* (*NSLS-II*), located in *Brookhaven National Laboratory*, and the scheme of the experimental setup is shown in **Figure 2.1**.

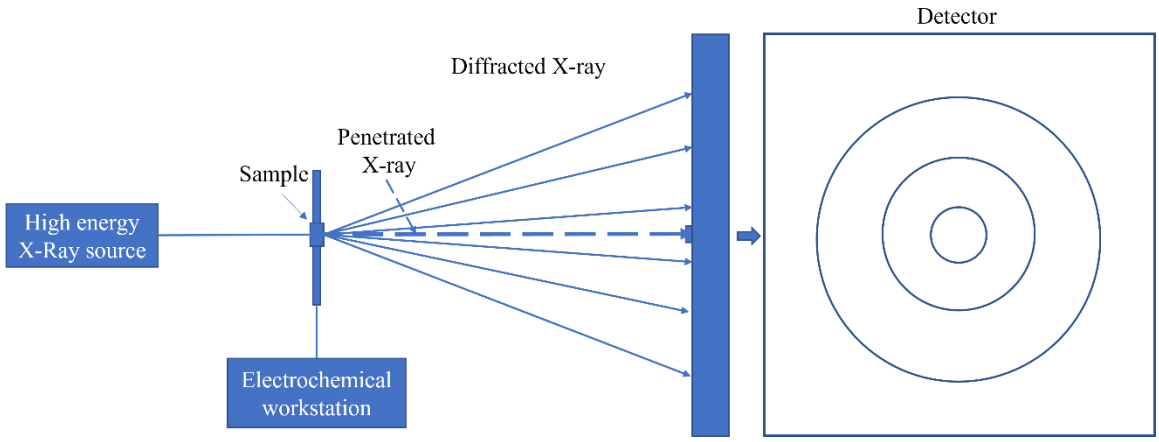

Figure 2.1 Scheme of *in-situ* XRD measurement setup.

The high-energy X-rays source can not only have X-rays with smaller wavelength, but also provide high flux X-rays. The high flux of X-rays ensured a quick acquisition of XRD patterns. The scan rate for both measurements were 0.5 mV· s^{-1}, the XRD patterns were collected with a

potential interval of 12.3 mV for the measurement with the electrolyte consisting of 0.1 M NaOH and 0.45 M Na_2SO_4, and 25.2 mV for the measurement with the electrolyte consisting of 0.25 M NaOH. It was possible to track the phase changes in detail during the electrochemical reactions with such a high resolution on potential.

It is worth mentioning that the detector used in this research was a 2D detector, which makes it possible to collect the diffracted X-ray at different angles all at once. Thus, unlike single crystals where the diffracted X-ray from the same series of atom planes that meet *Bragg*'s law (Equation 2.1) would be a spot on the detector, the diffracted X-ray from the same series of atom planes would be in all directions for powder X-ray diffraction and generate a circle on the detector.

$$d = \frac{n\lambda}{2sin\theta} \qquad \text{Equation 2.1}$$

λ is the wavelength, and n is a positive integer.

It is essential to point out that during *in-situ* XRD measurement, electrode materials, electrolytes, the supporting carbon paper, and Kapton tape used for sealing are penetrated and scattered by X-ray. Therefore, it is necessary to subtract the background signal (signal from any substance except the electrode materials) before analyzing the data.

As mentioned previously, electrode materials in the form of nanoparticles can generally reduce the diffusion length and are usually preferred. For nanoparticles, the crystalline size can be estimated by analyzing the XRD patterns using Equation 2.2, the *Scherrer* equation.[119-121]]

$$D_{hkl} = \frac{K \cdot \lambda}{B_{hkl} \cdot cos\theta} \qquad \text{Equation 2.2}$$

Where *hkl* is the *Miller* index of the targeted lattice plane, D_{hkl} is the crystallite size perpendicular to the lattice plane, B_{hkl} is the corrected full width at half maximum (FWHM) of

the diffraction peak in radians, K is the dimensionless shape factor, λ is the wavelength, and θ is the *Bragg* angle.

2.3 ELECTROCHEMICAL MEASUREMENTS

2.3.1 THREE-ELECTRODE HALF-CELL MEASUREMENTS

2.3.1.1 THE SETUP

An electrochemical reaction can be separated into two half-reactions, which can be studied separately using a three-electrode half-cell system. The scheme of a typical three-electrode half-cell is illustrated in **Figure 2.2**,

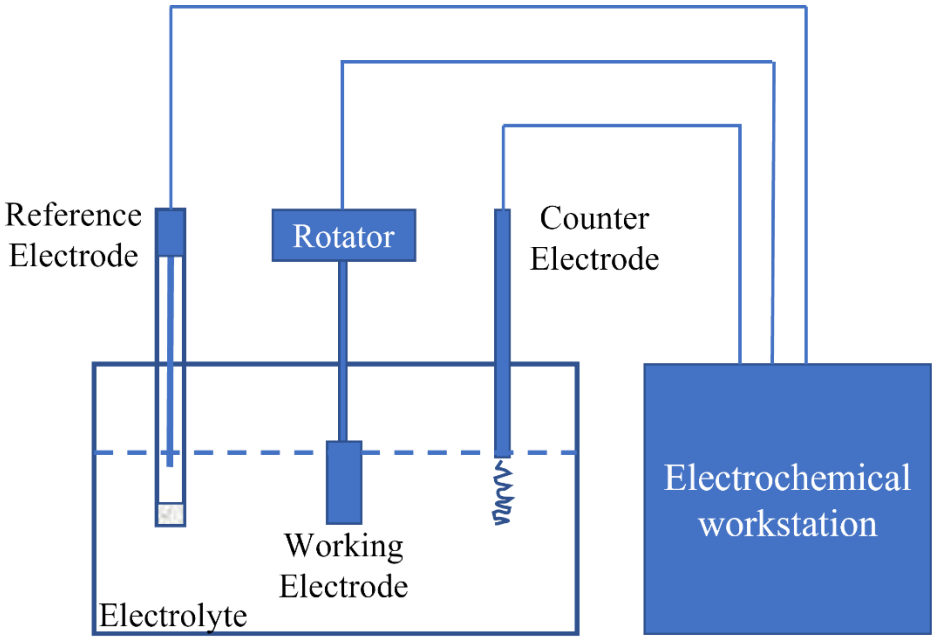

Figure 2.2 Scheme of a three-electrode half-cell system.

As shown in **Figure 2.2**, a three-electrode system includes the working electrode, counter electrode, and reference electrode. Materials to be investigated would be loaded on the working electrode connected to a rotator to reduce the transport limitation if needed. The counter

electrode is made of conducting material and inert to electrochemical reactions. The most used counter electrodes are platinum wire and graphite. The function of the counter electrode is to balance the charge transfer on the working electrode and complete the current circuit. Finally, the reference electrode serves as a reference point in determining the potential of the working electrode. The three-electrode half-cell measurements were conducted with CHI electrochemical workstation using a Hg/HgO reference electrode. Notably, the Hg/HgO reference electrode contains 1 M NaOH electrolyte, and thus 0 V vs. Hg/HgO corresponds to 0.14 V vs. Standard Hydrogen Electrode (SHE). Pt wire was used as the counter electrode.

2.3.1.2 THE PREPARATION OF ELECTRODES

A mixture of active material and carbon black (acetylene, 99.9+%, metal basis, Alfa Aesar) with a mass ratio of 7:3 was prepared for the working electrode prepared for CV and CP measurements. Since FeOOH itself has poor conductivity, the addition of carbon black improves the electric conductivity of the resulting mixture. Then an ink of the mixture in water was prepared and sonicated for half an hour before use to ensure a homogenous suspension. Next, the active material was loaded on the working electrode by drop-casting the ink suspension on glassy carbon, then vacuum dried before drop-casting again with 20 μL of Nafion solution (0.05% by mass, diluted from original ~ 5% Nafion 117 contaioning solution, Sigma Aldrich), and then vacuum dried before use. For CV measurements, the amount of active material loaded on the working electrode was 7 μg. For CP measurements, it was 28 μg. During the CV measurements, the rotating disc was used at a speed of 500 RPM.

2.3.1.3 THE PREPARATION OF ELECTROLYTES

The electrolytes were prepared with deionized water (18.2 $M\Omega \cdot cm$) and high purity chemicals, including sodium hydroxide (99.99%, metal basis, Alfa Aesar), sodium sulfate (99.9955%, metal

basis, Alfa Aesar). Notably, electrolytes containing NaOH were made right before use, and the cocktail electrolytes containing both NaOH and Na_2SO_4 were prepared and stored in a volumetric glass flask for 3 days before use (except for the electrolyte prepared for *in-situ* X-ray Diffraction measurement, where the electrolytes were prepared and used without stored in glass flask). The cocktail electrolytes may contain a trace amount of silicate ions, as the electrolyte could react with the silicon dioxide from the glass flask. It is reported that silicate ions would form a protective layer on the surface of iron oxides/hydroxides, which may result in better performance.[122-124]

2.3.1.4 CYCLIC VOLTAMMETRY (CV) AND CHRONOPOTENTIOMETRY (CP)

Depending on the electrode material properties, different electrochemical methods can be applied. In this research, Cyclic Voltammetry (CV) and Chronopotentiometry (CP) are the two methods that are used to investigate the electrochemical properties of the targeted materials.

In a typical CV measurement, the working electrode is applied with a constant changing potential between two potential points at a specific scan rate. The difference between applied potential and the equilibrium potential, namely the overpotential, is the driven force for the generated current, described in the *Butler–Volmer* equation (Equation 1.7, in **Section 1.2**).

CV measurements are widely used to investigate the kinetics of an electrochemical reaction. In this research, the electrochemical kinetics analysis was done based on the CV measurements conducted with a rotating disc loaded with microgram level of material, where the external diffusion limitations can be significantly minimized.

CP measurement is the most used electrochemical method in battery research, where a constant current is applied to the working electrode, and the corresponding changes of potential are recorded.

2.3.2 ASYMMETRIC FULL-CELL MEASUREMENTS

Full-cell measurements are usually used for studying the long-term performance of battery devices. Unlike the three-electrode system for half-cell measurements, full-cell measurements test two-electrode systems only containing the cathode and anode electrodes without a reference electrode. During the two-electrode test, the applied potential is the potential difference between anode and cathode, which is not equivalent to the absolute electrode potential. Two-electrode full-cells work under conditions similar to commercial battery devices.

In this research, the full-cells were prepared with FeOOH as anode and XC-72 carbon as cathode materials. The reason to choose XC-72 as anode materials is that the charge storage mechanism of XC-72 is primarily surface double-layer capacitance and remains stable over the cycles. Also, XC-72 has a plausible specific capacity due to its large surface area. Therefore, when excess amounts of XC-72 are used in the cathode, overall full-cell performance (*e.g.*, storage capacity and potential) can be primarily decided by the anode.

The full-cells were prepared with ECC-AQU electrochemical cells (EL-Cell GmbH, Germany) and measured with a BT-G Battery Analyzer (Arbin Instruments, USA). For the two-electrode full-cell measurements, 20 mg of XC-72 carbon loaded on Toray carbon paper (18 mm in diameter) as anode and 2 mg γ-FeOOH/carbon black (with a mass ratio of 2:8) mixture loaded on Toray carbon paper as the cathode, both cathode and anode electrode were prepared with 2.25%

of Styrene-Butadiene Rubber (SBR, MTI Corporation, USA) as the binder, 2.7 mL electrolyte was used. The filter paper was used as the separator.

2.3.3 ACQUISITION OF ELECTROCHEMICAL DATA

For the half-cell CV measurements except for the kinetics analysis, the measurements were done four times at the same condition to obtain the averaged data. The kinetics analysis in Section 3.2.2 and 3.2.6 were both calculated on one CV measurement conducted under a series of current densities, the measurements however were done three times for each condition with a standard deviation of the calculated b value less than 5%. For the half-cell CP measurements, the measurement was done four times under each condition with the standard deviation of capacity under 20 %, but only one dataset was used to analyze on and shown in the discussion in Chapter 4, unless otherwise ststed. For the full cell measurements, three runs were done for each condition, and the values for discharge capacity and coulombic efficiency were the averaged values from three runs. The individual CP profiles and the corresponding dC/dV curve were chosen from one of the three runs.

2.4 *IN-SITU* X-RAY DIFFRACTION MEASUREMENTS

The scheme of the *in-situ* XRD is shown in **Figure 2.1**. *In-situ* XRD measurements provide the ability to look at the changes in crystal structure during the electrochemical process, which was extremely helpful to a better understanding of the reaction chemistry. Several iron oxides/hydroxides were unstable under the standard atmosphere; traditional *ex-situ* measurements would likely not provide reliable information on the reaction chemistry.

In-situ XRD measurements were conducted with a wavelength of 0.166 Å. The homemade electrochemical cell was used with an Ag/AgCl micro-reference electrode. γ-FeOOH/carbon

black (mass ratio=7:3) mixture was drop-casted onto a thin Toray carbon paper (0.11 mm in thickness), along with Nafion as the binder. A platinum wire was used as a counter electrode. Two different electrolytes were used: 0.1 M NaOH with 0.45 M Na_2SO_4, 0.25 M NaOH, respectively. The electrolytes were prepared with the glass bottle and transferred to a plastic container without soaking in the glass bottle for an extended time. The thickness of the electrolyte was approximately 2 mm, which was penetrated by X-ray during the measurements. Before each *in-situ* XRD measurement, a blank cell that was identical to the actual cell but without the mixture of active material and carbon black was used for background diffraction image collection. The *in-situ* measurements were conducted without Argon flow, although the electrolytes were purged with Argon before using.

The images collected by the 2D detector during the measurement were first integrated into XRD patterns and then analyzed using Rietveld refinement to identify the phases and the corresponding ratio between each phase. The data processing was conducted using the software GSAS-II.[125]

CHAPTER 3 ELECTROCHEMICAL PROPERTIES OF LEPIDOCROCITE

3.1 MATERIAL CHARACTERIZATIONS

The synthesized material was in the form of power and had a brownish color, as shown in **Figure 3.1 (a)**. **Figure 3.1 (b, c, d)** were the SEM images collected on the synthesized sample to investigate the particle size and morphology. The particles had a spherical shape with a diameter under 100 nm. **Figure 3.1** (b, c) showed that the nano-sized particles generally aggregate to form larger clusters.

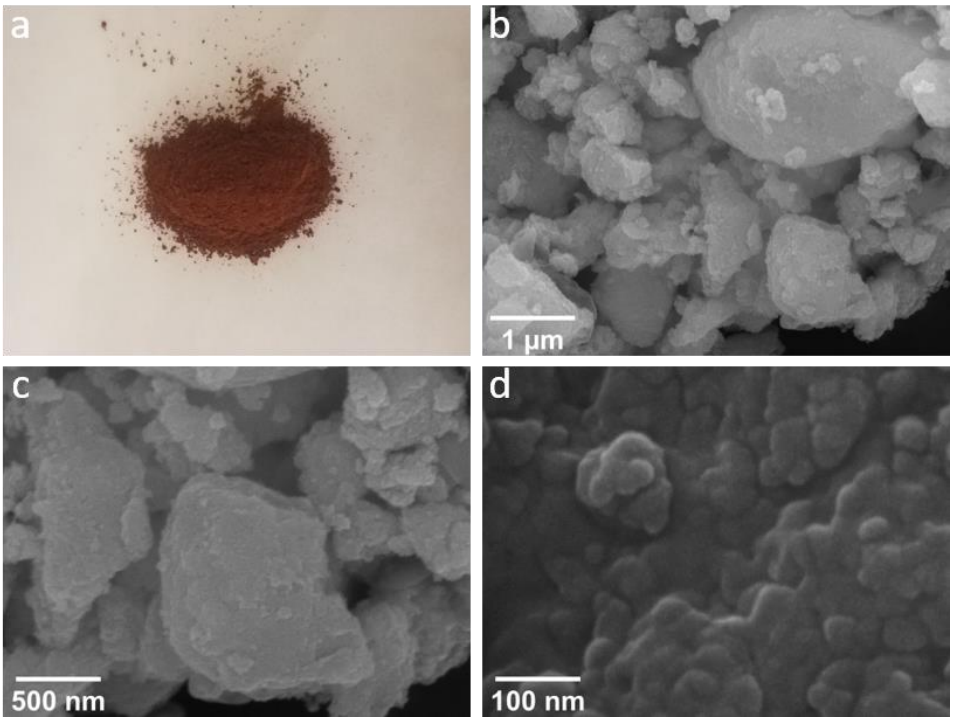

Figure 3.1 (a) Optical image and **(b, c, d)** SEM image of the synthesized material.

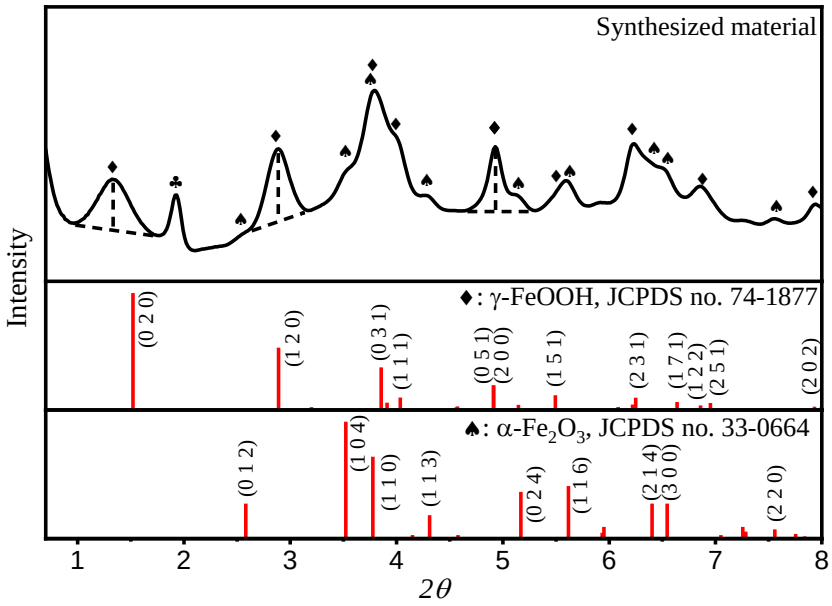

Figure 3.2 XRD patterns of the synthesized material.

XRD patterns are shown in **Figure 3.2**. The synthesized material has a dominant phase of lepidocrocite (γ-FeOOH, JCPDS no. 74-1877), as all the major peaks except the peak at 2θ=1.93° can be identified from γ-FeOOH. In addition to the dominant γ-FeOOH phase, there were also noticeable peaks that belong to hematite (α-Fe_2O_3, JCPDS no. 33-0664), as labeled in **Figure 3.2**. The sharp peak at 2θ=1.93° (d=4.95 Å) is likely from polytetrafluoroethylene (PTFE) impurity introduced into the product during synthesized from the PTFE coating of stirring bar.[126,127] As shown in **Figure 3.3**, γ-FeOOH has a layered structure consisting of [FeO_6] octahedral units, where Fe atoms reside in the center and oxygen atoms located at the corners. As shown in **Figure 3.2**, the diffraction peak at 2θ=1.33° is identified as the (2 0 0) peak from γ-FeOOH, suggesting a layer spacing of 7.18 Å.

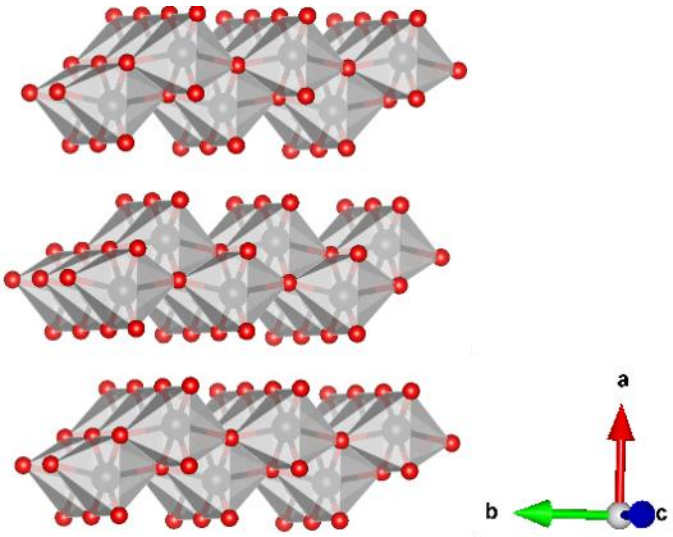

Figure 3.3 Illustration of the structure of γ-FeOOH: red dot represents an oxygen atom, black dot represents an iron atom. Hydrogen atoms are not shown in the structure.[128]

The crystallinity of the synthesized materials was also estimated from the XRD data with the *Scherrer* equation (Equation 2.2). Nickel powder was used as standard material to estimate the instrumental peak broadening using the averaged FWHM of selected peaks, and the value was calculated to be 0.00154. The peaks at 2θ=1.32°, 2.89° and 4.92° from γ-FeOOH were chosen for the calculation of crystallite size. A straight line was applied as the baseline for each peak in order to determine the FWHM. The estimated crystallite sizes are shown in **Table 3.1**. The estimated crystallite sizes with all three peaks were under 10 nm, which was in accordance with estimation from SEM data.

Table 3.1 Estimated crystallite size for the synthesized material.

Peak position (2θ)	1.32°	2.89°	4.92°
Estimated crystallite size (nm)	2.57	3.88	7.19

3.2 CV MEASUREMENTS OF LEPIDOCROCITE IN IN THREE-ELECTRODE HALF-CELL SYSTEM

3.2.1 ELECTROCHEMICAL PERFORMANCE OF LEPIDOCROCITE IN PURE ALKALINE ELECTROLYTES

The synthesized material was first tested with CV in 0.01 M NaOH electrolytes (pH=12) at a scan rate of 1 $mV \cdot s^{-1}$ under a potential window of -1.2 V to 0.2 V (vs. Hg/HgO). Three complete CV cycles were conducted, and the results are shown in **Figure 3.4**. The first segment was the cathodic scan (reduction process) from 0.2 V to -1.2 V, showing three reduction peaks at -0.87 V, -0.99 V and -1.11 V, respectively. However, during the second segment, the anodic scan (oxidation process) from -1.2 V to 0.2 V, only had one sharp peak around -0.60 V.

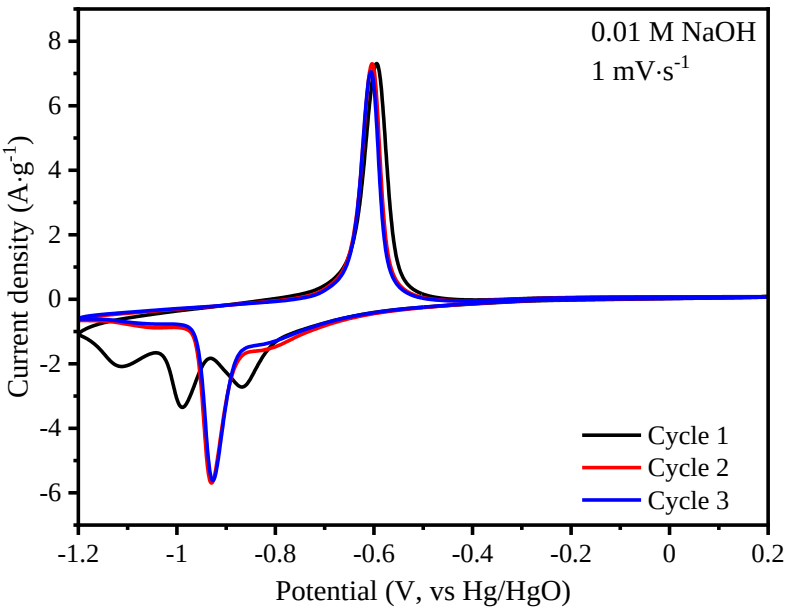

Figure 3.4 The first three cycles of CV results of γ-FeOOH measured in 0.01 M NaOH.

Notably, the reduction scan in the first cycle was different from the following reduction scan in the second cycle and third cycle, as both last two reduction scans only showed one reduction

peak at around -0.93 V. Therefore, the first reduction was thus considered as the activation process. The difference between the first reduction and the following reduction curves was likely due to the fact that the starting materials (made by a wet-chemistry method) had a different crystalline structure from the materials formed electrochemically. Specifically, the first reduction scan in this measurement started with the synthesized materials with a dominant phase of γ-FeOOH and minor phase of α-Fe_2O_3. In contrast, the later *in-situ* XRD illustrated that the second reduction scan started with a dominantly Fe_3O_4 phase, with a minimal amount of α-FeOOH. In the following analysis of half-cell CV measurements, all the analyses were conducted on the data collected from the second cycle, unless otherwise stated. It was worth mentioning that the overlapped CV curves between the second and third cycles suggested a stable redox process.

3.2.1.1 EFFECT OF THE CONCENTRATION OF SODIUM HYDROXIDE ON THE ELECTROCHEMICAL PERFORMANCE OF LEPIDOCROCITE

Besides 0.01 M NaOH electrolyte, 0.1 M NaOH electrolyte was also used for the CV test. As shown in **Figure 3.5**, the peak position of the reduction scan remained at roughly the same potential around -0.93 V, while the peak position of the oxidization scan shifted from -0.60 V in 0.01 M NaOH to -0.65 V in 0.1 M NaOH. The electrode capacity was calculated based on half of the area between the oxidization scan and the reduction scan, following Equation 3.1 and Equation 3.2:

Mass-specific capacitance: $C_{MS} = \frac{i}{(dV/dt)*m} = \int_{t_0}^{t_F} \frac{i}{\Delta V * m} dt$ Equation 3.1

Electrode capacity: $C_{electrode} = \frac{C_{MS}*\Delta V}{3.6}$ Equation 3.2

where i (A) is the measured current at the time of t (s), m (g) is the mass of the active material, ΔV (V) is the potential window. t_0 (s) and t_F (s) are respective times at the initial

potential and the final potential.[129] The electrode capacity shown in the following sections in CV measurements is the average of capacity of reduction scan and oxidization scan.

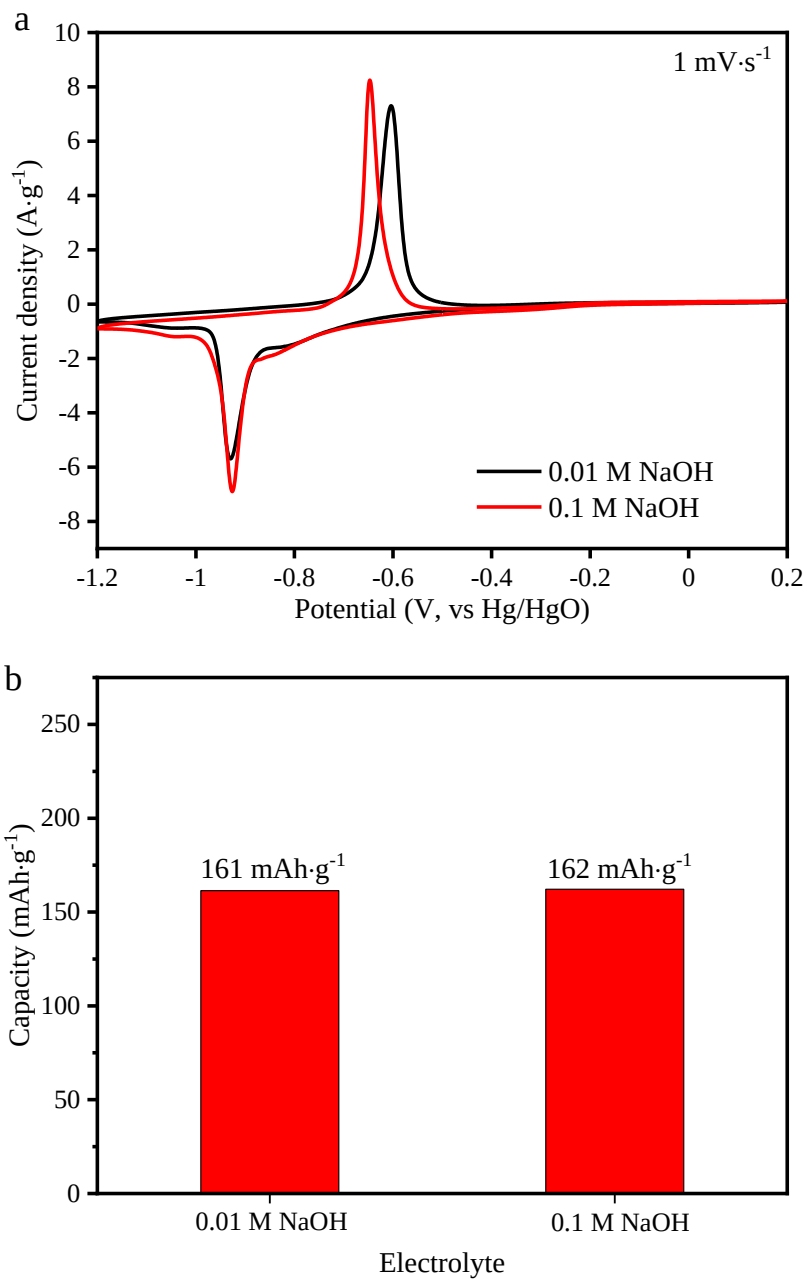

Figure 3.5 (a) CV results of γ-FeOOH in electrolytes with different pH and **(b)** the calculated capacities.

It was 161 mAh·g^{-1} in 0.01 M NaOH and 162 mAh·g^{-1} in 0.1 M NaOH electrolyte. The capacity remained almost the same after increasing the concentration of the alkaline solution by ten times, suggesting 0.01 M NaOH was sufficient in providing enough OH^- to the reaction in the current system. Despite the difference in peak position, there was no noticeable difference between the electrochemical performance of the synthesized material in pH=12 and pH=13 environments.

3.2.1.2 REACTION KINETICS OF LEPIDOCROCITE IN PURE SODIUM HYDROXIDE ELECTROLYTE

The reaction kinetics was an important aspect of an electrochemical reaction and was decided by the intrinsic reaction rate and the mass transfer rate associated with the diffusion of the charge carriers. The reaction kinetics of the electrochemical reactions were investigated by analyzing CV plots measured at different scan rates. In a CV measurement, the observed current can be described by the power-law (Equation 3.3):

$$i = av^b \qquad \text{Equation 3.3}$$

where both *a* and *b* are adjustable parameters.[130] The value of *b* is an indication of the mechanism of the charge transfer process: when *b* value equals 1, the current is in a linear relationship of the scan rate, indicating that the current was generated from double-layer capacitance; when *b* value equals 0.5, the current is in a linear relationship of the square root of the scan rate, indicating the electrochemical charge storage process was a diffusion-limited process. When the b value falls between 0.5 and 1, the charge storage mechanism is a hybrid process that includes the double-layer capacitive and diffusion-limited processes.

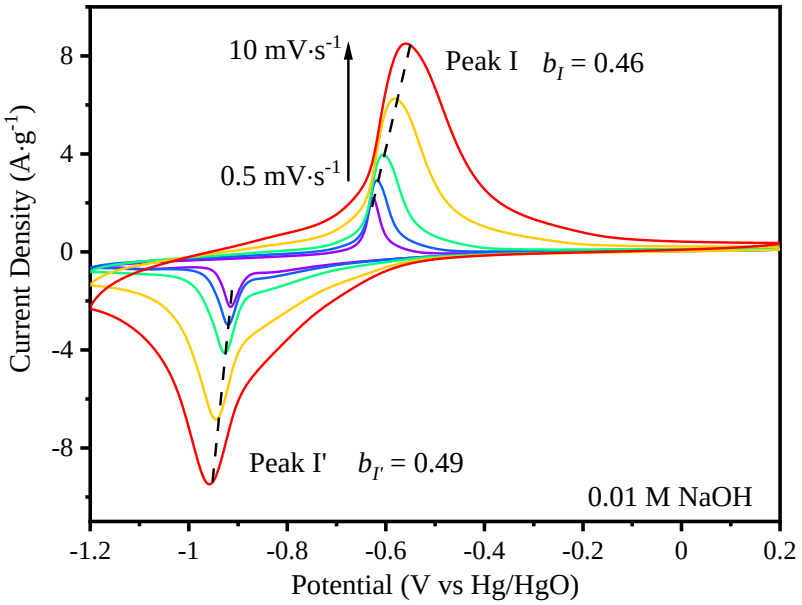

Figure 3.6 Kinetics analysis of the electrochemical process of γ-FeOOH in 0.01 M NaOH.

Figure 3.6 shows the CV measurements at a series of scan rates ranging from 0.5 $mV{\cdot}s^{-1}$, 1 $mV{\cdot}s^{-1}$, 2 $mV{\cdot}s^{-1}$, 5 $mV{\cdot}s^{-1}$, to 10 $mV{\cdot}s^{-1}$. As shown in **Figure 3.6**, the major redox peak in both oxidization scan and reduction scan had a *b* value close to 0.5, indicating the related electrochemical reaction was a diffusion-limited process. When the scan rates increased from 0.5 $mV{\cdot}s^{-1}$ to 10 $mV{\cdot}s^{-1}$, the peak positions in the oxidization scans shifted to higher potential and also shifted to lower potential in the reduction scan. The peak separation between oxidization and reduction scans increased from 0.28 V at 0.5 $mV{\cdot}s^{-1}$ to 0.40 V at 10 $mV{\cdot}s^{-1}$. An increasing peak separation indicated that the redox process became less reversible when the scan rates increased.

3.2.2 ELECTROCHEMICAL PERFORMANCE OF LEPIDOCROCITE IN COCKTAIL ELECTROLYTES

Figure 3.7 shows the CV measurements conducted with a cocktail electrolyte containing NaOH (0.01 M) and Na_2SO_4 (0.2 M). The choice of Na_2SO_4 was made based on the following

considerations. First, SO_4^{2-} is electrochemically stable under the reducing environment applied in this project; Second, it carries two negative charge, beneficial for an insertion-type of redox reaction. For the same amount of anions the host materials could accommodate, a higher storage capacity would achieve when multi-valance ions were used than mono-valene ions. When pure NaOH electrolyte was used, there was only one redox couple at -0.60 V/-0.93 V (anodic scan/cathodic scan), as previously discussed. However, in addition to the major redox peaks at -0.58 V/-0.89 V, a new redox feature appears at -0.48 V/-0.54 V in the cocktail electrolyte. The major redox peaks also showed a change in potential from -0.60 V/-0.93 V in 0.01 M NaOH to -0.58 V/-0.89 V in the cocktail electrolyte.

The overall capacity increased from 161 $mAh \cdot g^{-1}$ to 242 $mAh \cdot g^{-1}$ in the cocktail electrolyte, approximately 50% higher than that measured in NaOH electrolyte. The overall capacity could be from two charge storage processes: double-layer capacitive process and diffusion-limited electrochemical redox reaction. The previous results (**Figure 3.6**) suggested that the diffusion-limited redox reactions dominated the charge storage process. Therefore, the capacity increase in cocktail electrolytes likely resulted from diffusion-limited redox reactions. Moreover, a new redox peak couple in CV measurement indicated a new redox reaction due to $NaSO_4$ addition. More details on this new redox reaction will be discussed later during *in-situ* XRD measurement (**Section 3.3**).

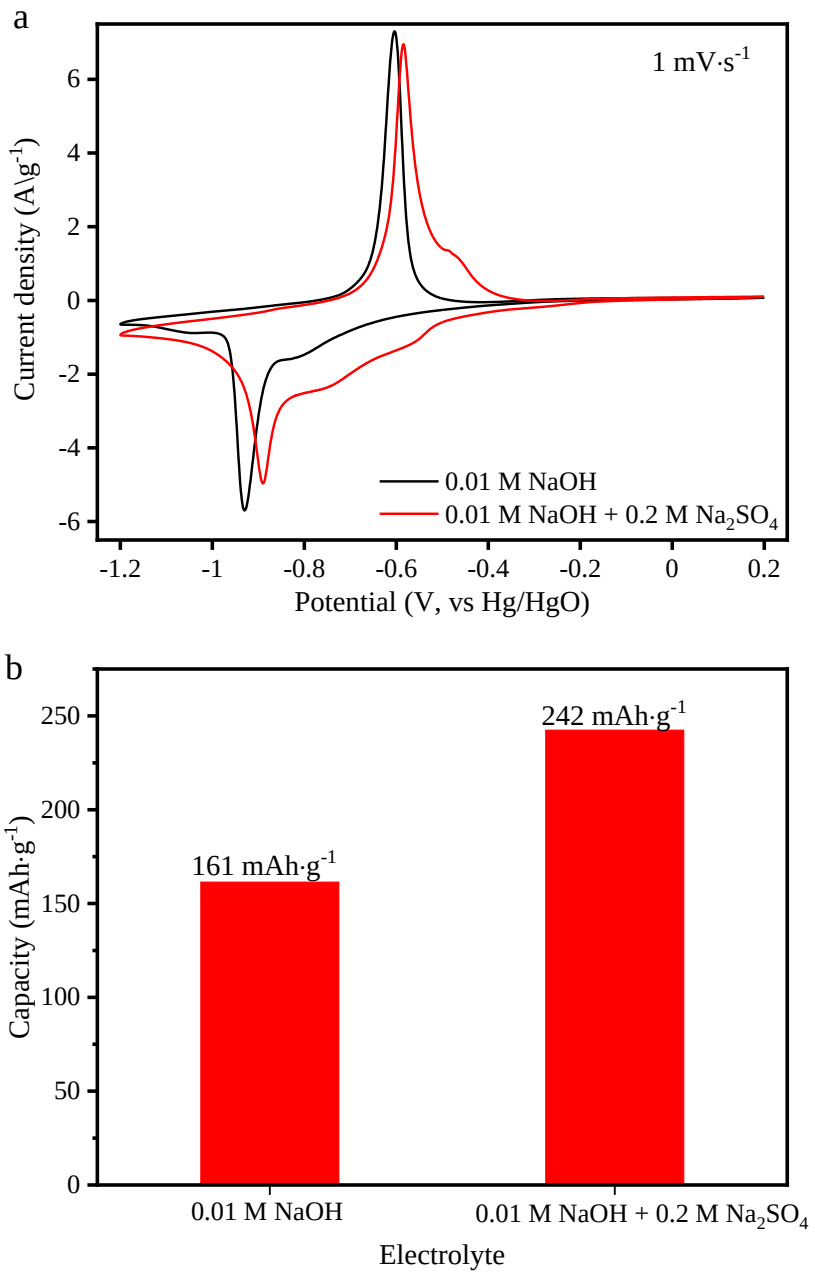

Figure 3.7 (a) CV results of γ-FeOOH measured in different electrolytes at pH=12 and **(b)** the calculated capacities.

3.2.2.1 EFFECT OF ALKALINITY OF THE COCKTAIL ELECTROLYTE ON THE ELECTROCHEMICAL PERFORMANCE OF LEPIDOCROCITE

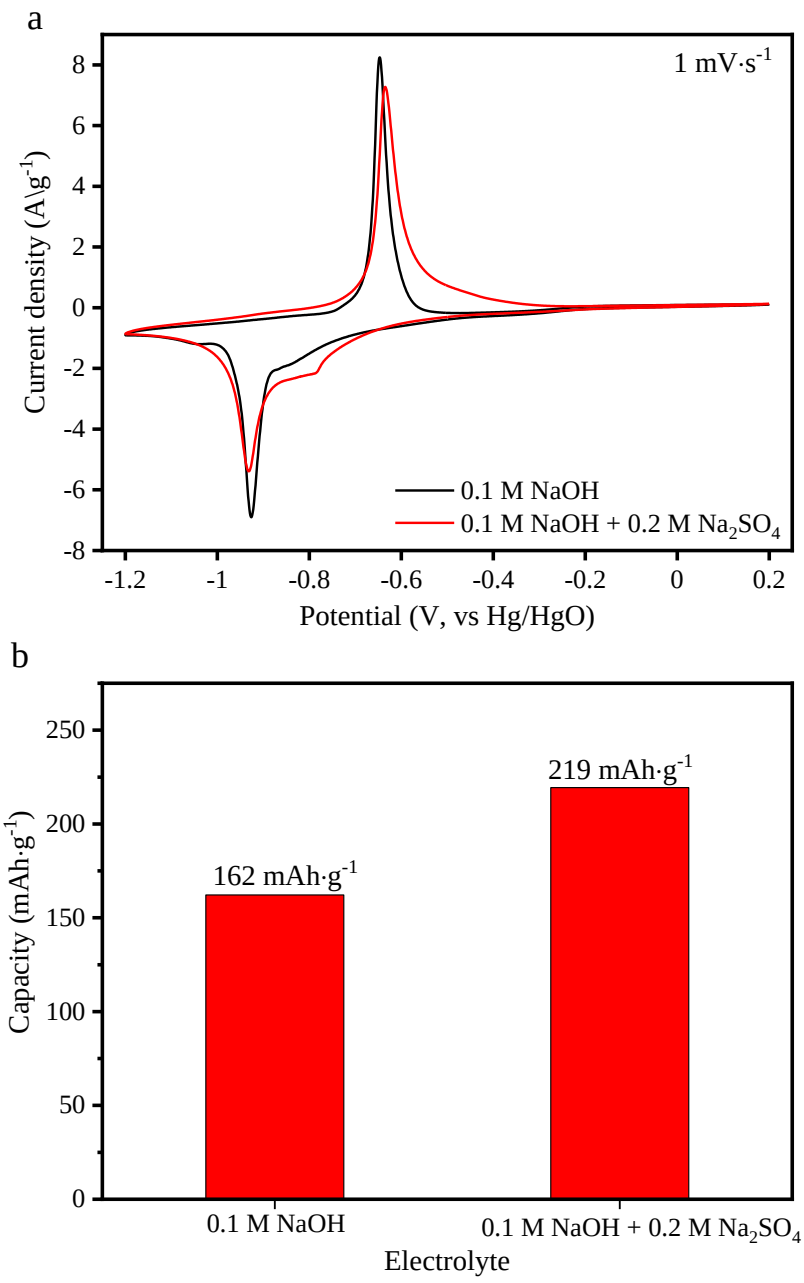

Figure 3.8 (a) CV results of γ-FeOOH measured in different electrolytes at pH=13 and **(b)** the calculated capacities.

The effect of adding Na_2SO_4 into the electrolyte was also investigated in electrolytes with higher pH, as shown in **Figure 3.8**. The cocktail electrolyte did not incur an observable new couple of redox peaks at a higher pH environment. However, it is evident that the oxidization peak in the cocktail electrolyte was asymmetric and had a tail around -0.45 V, while in the pure NaOH electrolyte, it was nearly symmetric. The capacity increased from 162 $mAh \cdot g^{-1}$ to 219 $mAh \cdot g^{-1}$, an approximately 35% increase, less significant than that observed in cocktail electrolytes with a lower pH.

The electrochemical performance of γ-FeOOH was studied in cocktail electrolytes with different concentrations of Na_2SO_4 under two pH conditions at a scan rate of 1 $mV \cdot s^{-1}$. The results are shown in **Figure 3.9**. It was clearly shown that the new redox feature (~ -0.5 V during the anodic scan) became more distinct in cocktail electrolytes with 0.01 M NaOH than that with 0.1 M NaOH. The results suggested the new redox feature and much-improved storage capacity is strongly associated with SO_4^{2-} anion, and on the other hand, is also inhibited by OH^- involved charge-storage process. Notably, the following half-cell measurements were reported in pH=12 electrolytes.

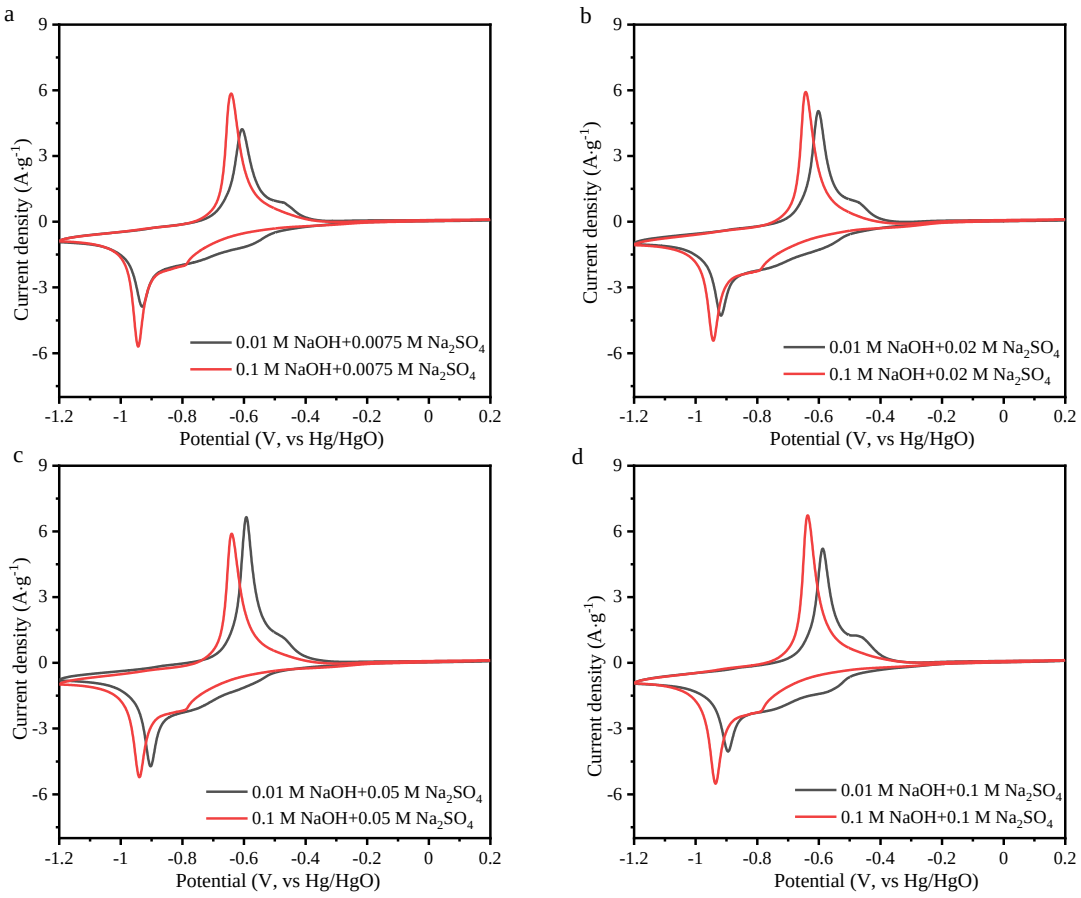

Figure 3.9 CV measurements of γ-FeOOH in electrolytes at pH=12 and pH=13 environments with different concentrations of Na_2SO_4: **(a)** 0.0075 M Na_2SO_4; **(b)** 0.02 M Na_2SO_4; **(c)** 0.05 M Na_2SO_4; **(d)** 0.1 M Na_2SO_4.

3.2.2.2 EFFECT OF THE CONCENTRATION OF SODIUM SULFATE OF THE COCKTAIL ELECTROLYTES ON THE ELECTROCHEMICAL PERFORMANCE OF LEPIDOCROCITE

The CV profiles of different concentrations of Na_2SO_4 at pH=12 are shown in **Figures 3.7** and **Figure 3.9**. The capacity under each condition was summarized in the following **Figure 3.10**. It was shown that the increase of c(Na_2SO_4) from 0.0075 M to 0.2 M resulted in an increase in capacity, from 201 mAh·g^{-1} to 242 mAh·g^{-1}. As discussed previously, both SO_4^{2-} anion and OH^-

impacted the new redox feature. Therefore, under the same OH^- concentration, more SO_4^{2-} anion likely favored the new redox feature and resulted in an improved capacity.

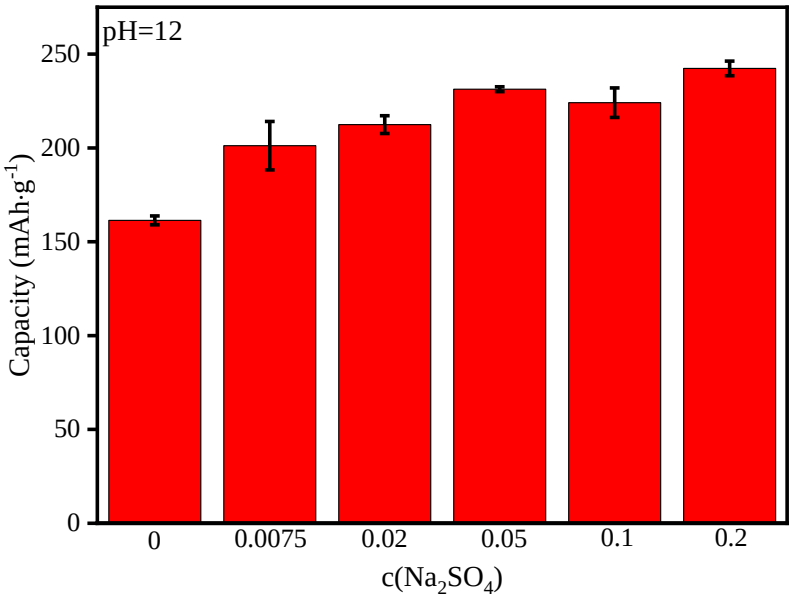

Figure 3.10 Capacity at different concentrations of Na_2SO_4 ($c(Na_2SO_4)$) under pH=12.

3.2.2.3 ELECTROCHEMICAL KINETICS OF LEPIDOCROCITE IN THE COCKTAIL ELECTROLYTE

The electrochemical kinetics analysis was also conducted on γ-FeOOH in the cocktail electrolyte using CV measurements with the scan rates ranging from 0.5 $mV \cdot s^{-1}$ to 10 $mV \cdot s^{-1}$. As shown in **Figure 3.11**, the *b* value of Peak I (anodic scan) and Peak I' (cathodic scan) were both close to 0.5, indicating that the electrochemical process was a diffusion-limited redox reaction. When the scan rates increased from 0.5 $mV \cdot s^{-1}$ to 10 $mV \cdot s^{-1}$, the Peak I positions shifted to higher potential, and Peak I' shifted to lower potential. In addition, the peak separation between Peak I and Peak I' increased with increasing scan rates, suggesting that the redox processes became more irreversible as scan rates increased (and a faster reaction rate). Meanwhile, the peak couple at -0.48 V/-0.54 V (the new redox feature associated with SO_4^{2-} addition) became less

distinguishable with increased scan rates. As it was challenging to separate this new redox feature from the main anodic peaks, the analysis of the *b* value of this redox couple was not conducted.

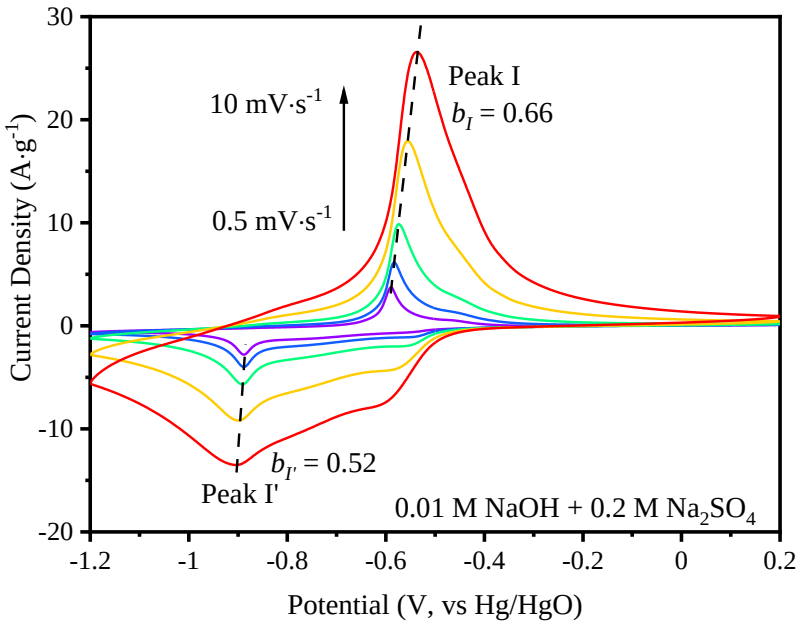

Figure 3.11 Kinetics analysis of the electrochemical process of γ-FeOOH in the cocktail electrolytes consisting of 0.01 M NaOH and 0.2 M Na_2SO_4.

3.2.3 CONTRIBUTION TO CV RESULTS FROM THE SIDE REACTION AND THE BACKGROUND.

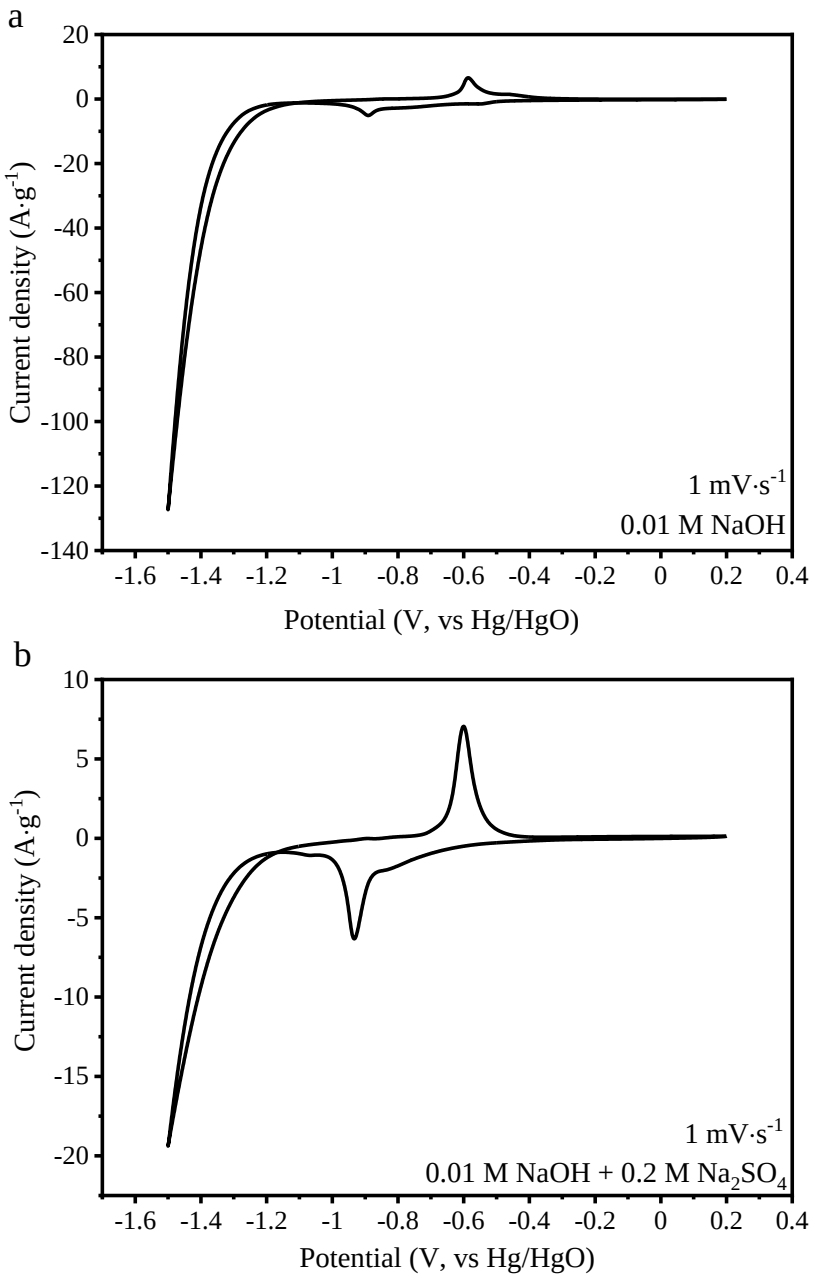

Figure 3.12 CV measurements conducted under a wide potential window with two electrolytes: **(a)** 0.01 M NaOH, **(b)** 0.01 M NaOH with 0.2 M Na_2SO_4.

According to the Nernst Equation, HER equilibrium potential at pH=12 is -0.85 V vs. Hg/HgO, within the potential window for FeOOH electrochemical measurements (-1.2 V to 0.2 V). Though the actual HER might happen at the potential lower than -0.85 V by considering the overpotential, the possible contribution of hydrogen evolution reaction (HER) to the overall CV signal needs to be studied.

Figure 3.12 shows the CV measurements of FeOOH under a wide potential window between -1.5 V and 0.2 V in pure 0.01 M NaOH and cocktail electrolytes. HER occurred in both electrolytes when the potential approached -1.5 V. However, above the potential of -1.2 V, the current signal was close to zero, suggesting no significant current from HER.

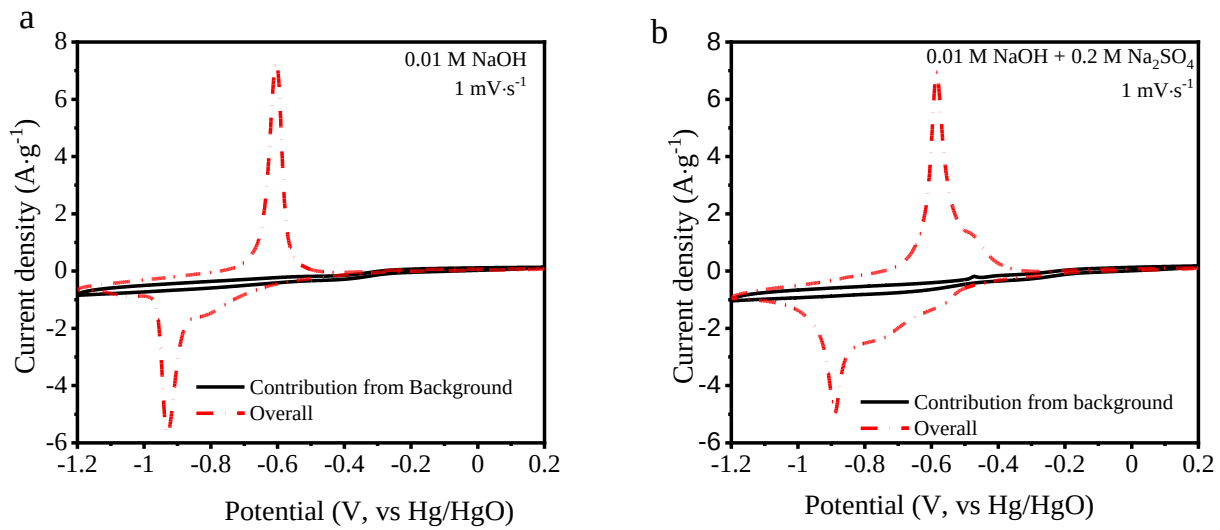

Figure 3.13 Contribution from background for the CV measurements with two electrolytes: **(a)** 0.01 M NaOH, **(b)** 0.01 M NaOH with 0.2 M Na_2SO_4.

Besides HER current, the background signal was also considered. In the preparation of the electrode ink, the active material was mixed with carbon black to increase the conductivity. Thus, the contribution from carbon black (additive) and glassy carbon (current collector substrate) was measured in CVs, and the data are shown in **Figure 3.13**. Clearly, the background

contributes little signal compared to FeOOH active materials. Moreover, the background signal had no redox feature in the potential window, suggesting background contribution mainly resulted from double-layer capacitance occurring on the electrode surface. Notably, the contribution from the background was only identified and shown in **Figure 3.13.** The CV data shown previously in this chapter were without background subtraction.

3.3 INVESTIGATION ON THE REACTION MECHANISM OF LEPIDOCROCITE IN ALKALINE SYSTEM USING *IN-SITU* XRD

3.3.1 CV TESTS OF LEPIDOCROCITE FOR THE *IN-SITU* XRD MEASUREMENTS

The reaction mechanism was investigated with *in-situ* XRD measurements. CV was used as the electrochemical method with a potential window of -1.2 V to 0.2 V, the same conditions as half-cell measurements. A lower scan rate (0.5 $mV \cdot s^{-1}$) and higher concentration of electrolytes (0.1 M NaOH with 0.45 M Na_2SO_4, and 0.25 M NaOH) were chosen since the loadings of active materials in XRD measurement were in a milligram level, nearly 1000 times higher than the loading in half-cell measurements. High loading of active material was used to generate adequate X-ray diffraction signals for more accurate data analysis, as the diffraction counts were related to the mass loading.

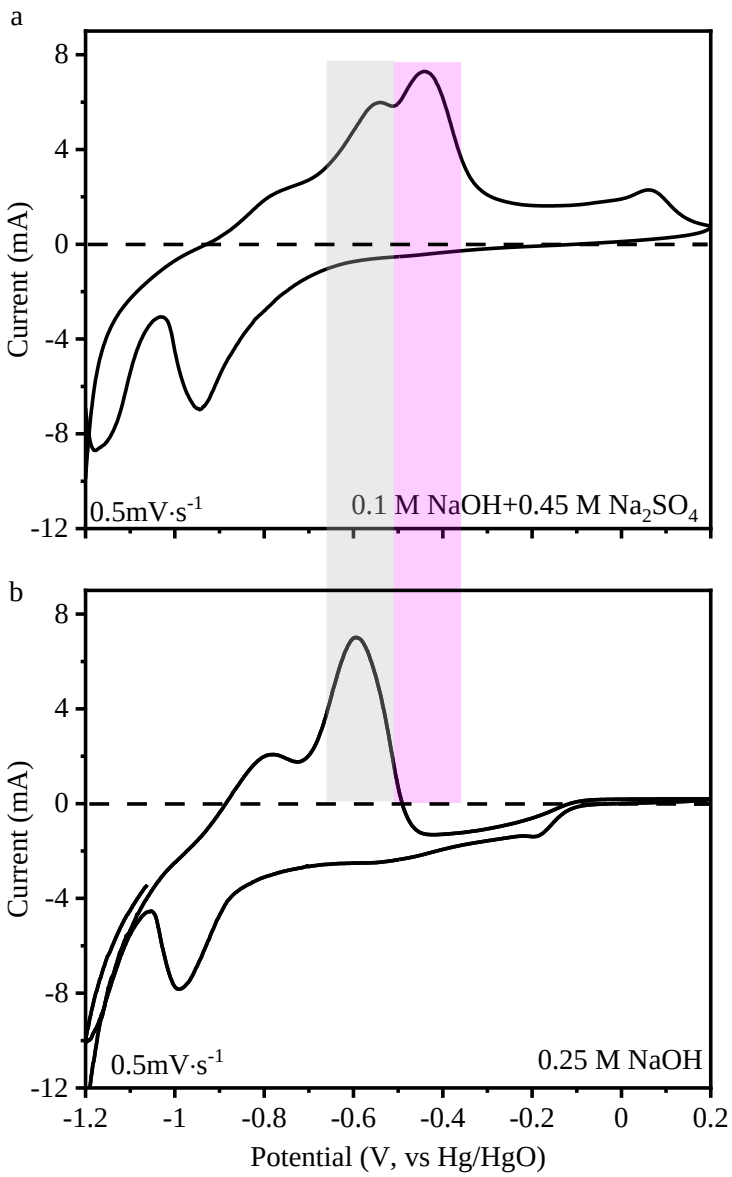

Figure 3.14 CV results for the *in-situ* XRD measurements with different electrolytes: **(a)** 0.1 M NaOH with 0.45 M Na_2SO_4; **(b)** 0.25 M NaOH.

Figure 3.14 showed the CV results during *in-situ* XRD measurements when pure NaOH and cocktail electrolytes were used. The CV measurements started with a reduction scan, which was regarded as the activation process. The CV data shown in this figure were the following oxidization scan and the next reduction scan. An additional region of the second oxidization scan

from -1.2 V to -1.06 V for the measurement with NaOH as electrolyte was included for a better illustration of phase changes. CVs showed an oxidation peak at -0.6 V in both electrolytes. However, an additional oxidization peak was around -0.45 V in the cocktail electrolyte, missing in the pure NaOH electrolyte. Similar differences were also observed from half-cell measurements. It was notable that the CV curves from *in-situ* XRD were slightly unbalanced in total charges and showed more discernable negative current contributions. Oxygen reduction reaction (ORR), as shown in Equation 3.4, may contribute negative current during the *in-situ* measurements.

$O_2 + 4e^- + 2H_2O \rightarrow 4OH^-$ (in an alkaline environment) Equation 3.4

The equilibrium potential for the ORR in 0.25 M NaOH was around 0.3 V vs. Hg/HgO. Thus, theoretically, the ORR could happen during the measurement in the presence of oxygen gas. The inert gas protection wasn't employed during *in-situ* measurements due to the complex sample environment when setting up an in-situ XRD test, although the electrolytes were purged with inert gas before use.

There could be two sources of dissolved oxygen in the electrolyte. The first one was that the oxygen might diffuse into the electrolyte from the air, as the experiment was conducted without inert gas protection. The second one was that the oxygen could form on the counter electrode during the CV measurements. The counter electrode used in the measurement was a Pt wire, which had a limited surface area. In the reduction scan of the working electrode, there would be OER on the counter electrode simultaneously to account for the charge balance. Thus, some oxygen gas formed on the counter electrode could dissolve into the electrolyte and diffuse toward the working electrode.

3.3.2 DATA ANALYSIS ON THE RESULTS FROM *IN-SITU* XRD MEASUREMENTS

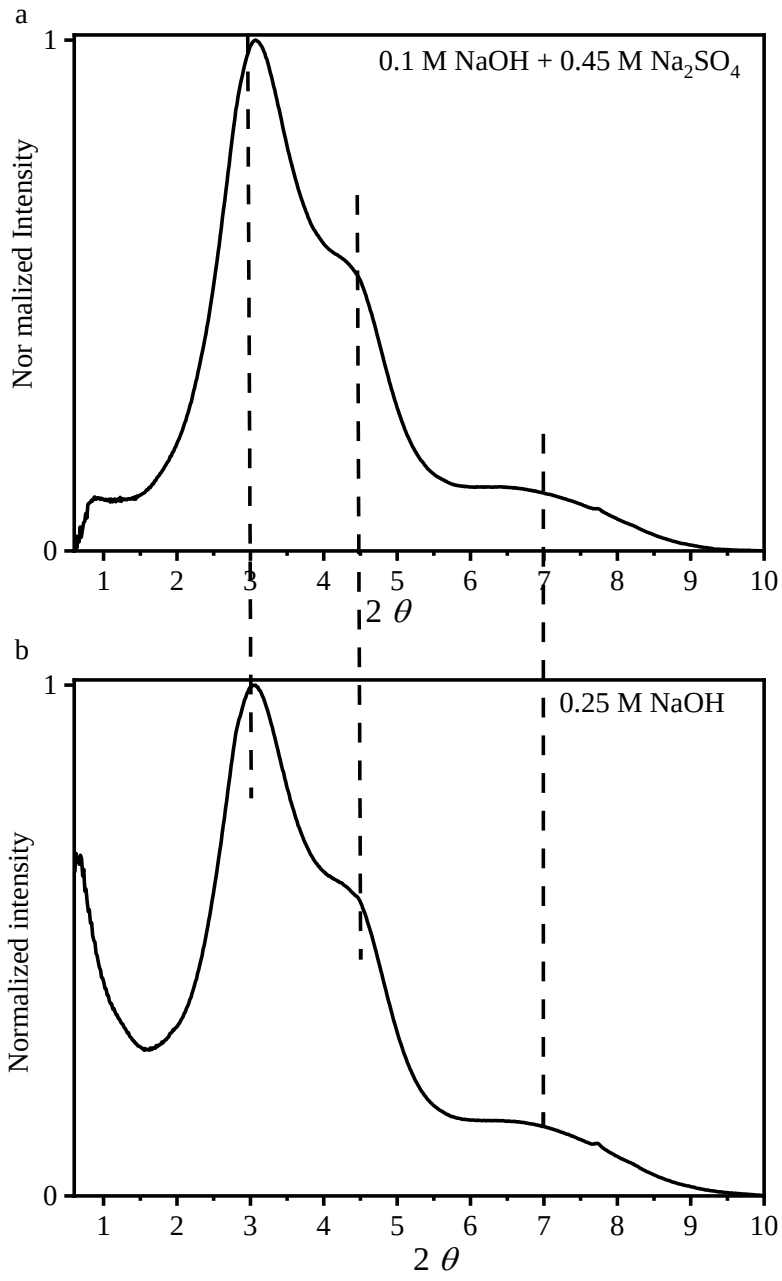

Figure 3.15 Background XRD patterns for different electrolytes: **(a)** 0.1 M NaOH with 0.45 M Na_2SO_4; **(b)** 0.25 M NaOH.

A background scattering pattern without loading of active material or carbon black was collected for both measurements before starting the *in-situ* XRD measurements. As mentioned previously,

the X-ray needs to penetrate a series of supporting materials, including layers of Kapton tape used for sealing, Toray carbon paper where the material was loaded, and most importantly, the aqueous electrolyte around 2 mm in thickness along the pathway of the X-ray. Since the electrolytes with different compositions could have different scattered X-ray signals, an individual background pattern was obtained for each electrolyte.

The background scattering patterns for each electrolyte are shown in **Figure 3.15**. The two background patterns were very similar as they are both dominated by water scattering, even though they have different dissolved salts.

The scattering peaks at around 2θ=3°, 4.5°, 7° were identified from water scattering.[131,132] The difference below 2θ=1.5° was likely due to the difference in the effect of air scattering. The two sets of data were collected at different settings, even though at the same beamline. And we believe the position of the beam stop might attribute to the scattering at the low 2θ angle. It is worth noting that beam stop was used in X-ray scattering measurements to block the X-ray that directly penetrates the sample without being scattered. In the measurement shown in **Figure 3.15 (a)**, the beam stop was put right after the sample. While in the second measurement shown in **Figure 3.15 (b)**, the beam stop was located near the detector. Thus, the X-ray that directly penetrated the sample likely incurred air scattering before hitting the beam stop close to the detector. However, the air scattering was minimal in the first measurement, as the penetrated X-ray was blocked right after the sample.

This air scattering was not an issue for later data refinement, as it would be subtracted from the raw scattering data, along with other background signals. No discernable peak could be identified as scattering from Kapton tape or Toray carbon paper, as their scattering signals were relatively marginal than the background signal from water.

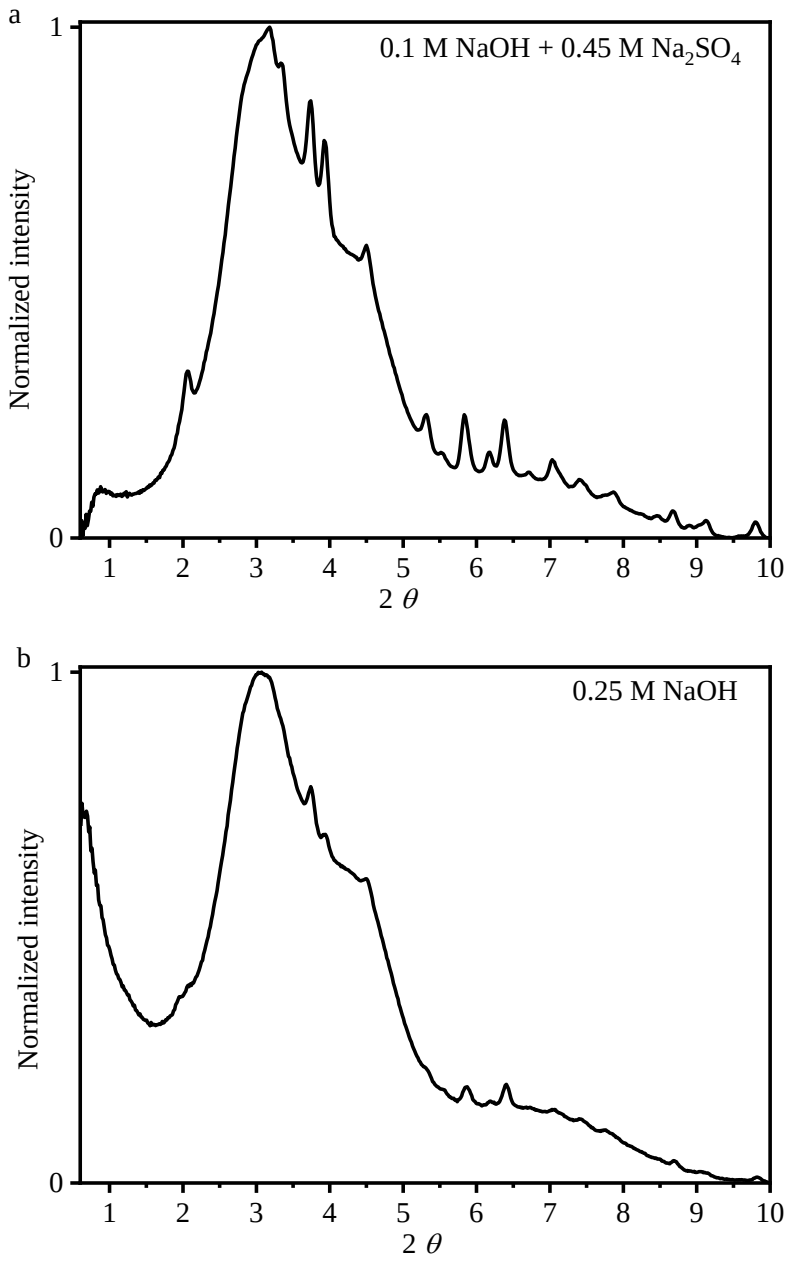

Figure 3.16 XRD patterns before subtracting background file at -1.2V for different electrolytes: **(a)** 0.1 M NaOH with 0.45 M Na_2SO_4; **(b)** 0.25 M NaOH.

The X-ray scattering data were collected at the same time, along with the CV measurements. **Figure 3.16** was one representative XRD pattern collected at -1.2 V from each condition before the background subtraction. The overall signal was dominated by water scattering. Therefore, it

was impossible to conduct accurate structure refinement to obtain helpful information such as phase fractions or lattice parameters without background subtraction.

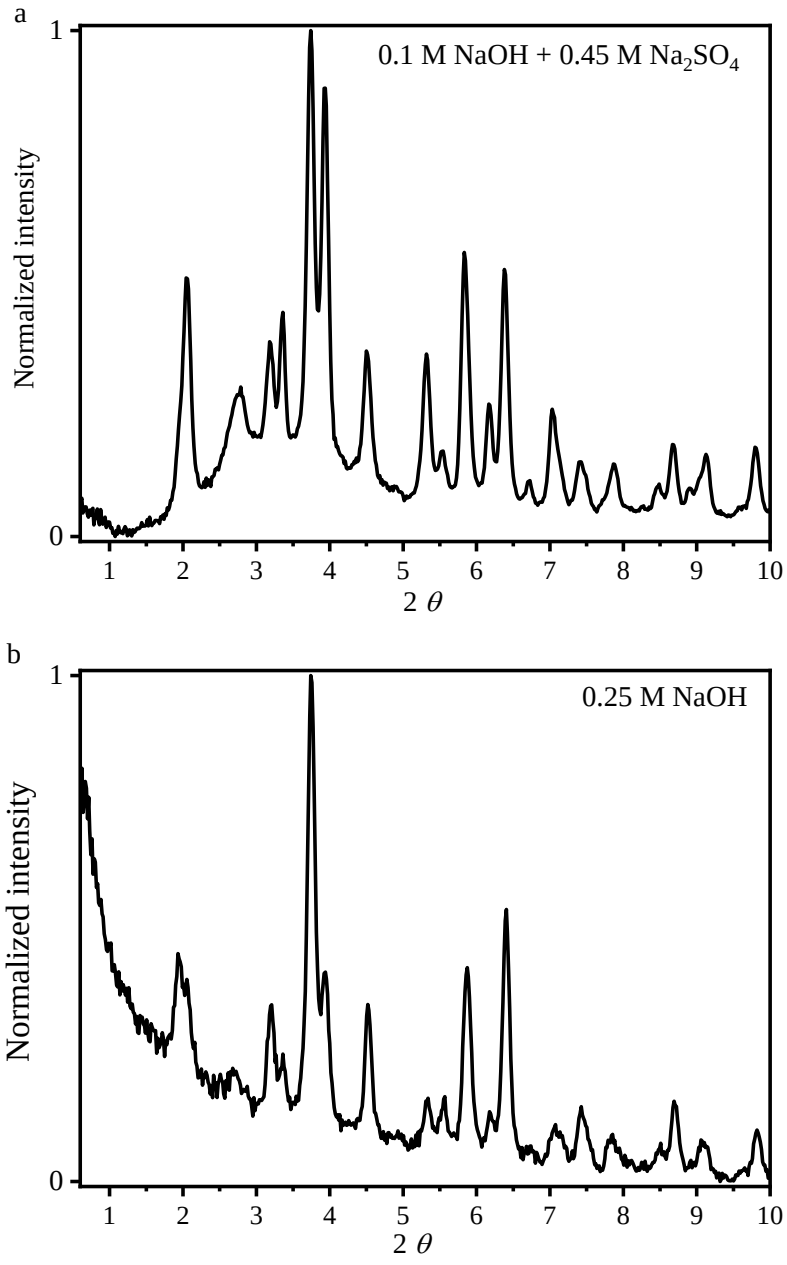

Figure 3.17 XRD patterns after subtracting background file at -1.2V for different electrolytes: **(a)** 0.1 M NaOH with 0.45 M Na_2SO_4; **(b)** 0.25 M NaOH.

Figure 3.17 shows the XRD data after background subtraction. After subtracting background, it was clear that more peaks were observable under both conditions, and more information on the crystal structure could be obtained from data analysis.

A perfect diffraction pattern, in theory, would have a flat baseline. As shown in **Figure 3.17**, there were still significant background signals. Also, the diffraction peak at 2θ=2.73° was identified from carbon black additive by comparing the *ex-situ* XRD patterns measured on the carbon black, as shown in **Figure 3.18**. Thus, a *chebyschev* function was used to fit the background during the Rietveld refinements using software *GSAS-II*. The *in-situ* XRD patterns presented in the following figures were after the subtraction of the fitted background. The phases were identified with published structures.[128, 133-136]

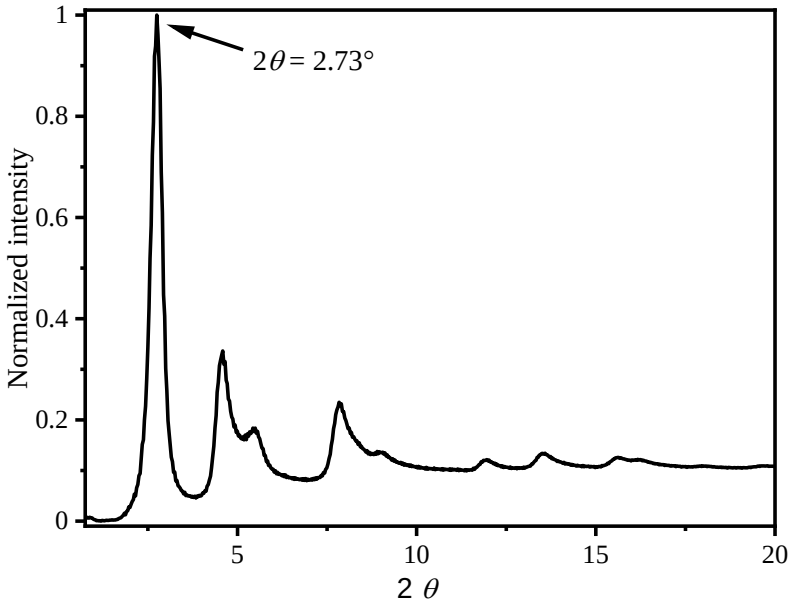

Figure 3.18 XRD patterns of carbon black.

It was worth mentioning that the 2θ range used for the fitting was from 0.6° to 10°. As the wavelength used here was λ = 0.166 Å, the corresponding *d* spacing range can be calculated by

Bragg's Law to be 0.95 Å to 15.85 Å. To better demonstrate the changes in the scattering patterns, a 2θ range from 0.6° to 6° was presented in the following figures, as it already contained sufficient scattering features.

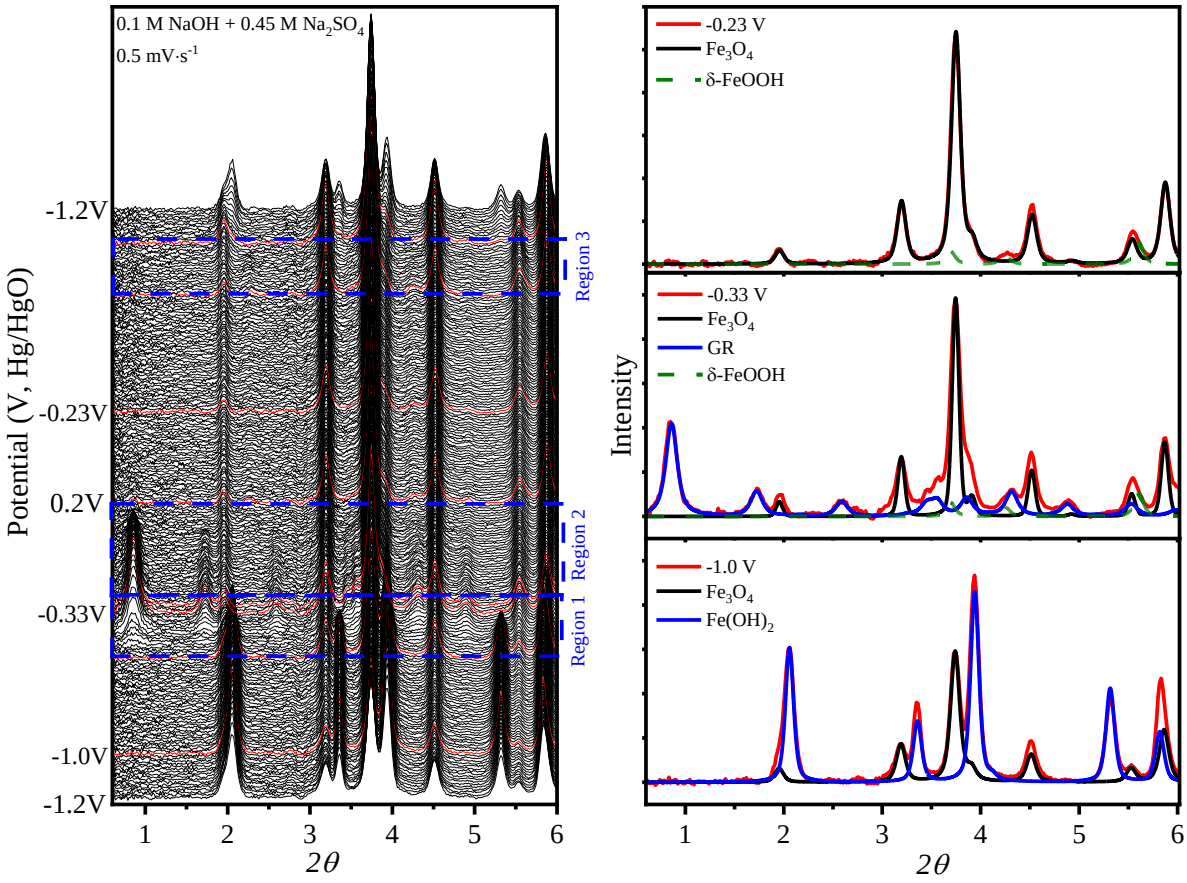

Figure 3.19 Waterfall plot of *in-situ* XRD patterns and picked individual XRD patterns from the cocktail electrolytes consisting of 0.1 M NaOH with 0.45 M Na_2SO_4.

A waterfall plot of the *in-situ* XRD patterns and some selected individual patterns from cocktail electrolytes were shown in **Figure 3.19** and **Figure 3.20**. The patterns were listed in the order of different potential during the CV measurements, from which several crystalline phases of the electrode materials were identified between the potential window ranging from -1.2 V to 0.2 V. At a potential of -1.0 V, a mixture of Fe_3O_4 and $Fe(OH)_2$ phases was identified. In Region 1 from

-0.54 V to -0.29 V in the oxidization scan, a declining peak intensity of $Fe(OH)_2$ was accompanied by the formation of a Green Rust (GR) phase, and a δ-FeOOH phase started to form at -0.35 V. In Region 2 from -0.29 V in the oxidization scan, the diffraction signal from GR phase decreased and disappeared at 0.15 V, accompanied by the increase of δ-FeOOH phase from -0.29 V to around 0.15 V. From 0.15 V to 0.2 V, the intensity of δ-FeOOH phase and Fe_3O_4 phase remained roughly stable. In Region 3 from -0.79 V δ-FeOOH started to diminish and disappeared at -0.98 V, Fe_3O_4 became the only phase from -0.98 V to -1.02 V, a trace amount of $Fe(OH)_2$ was formed from -1.03 V.

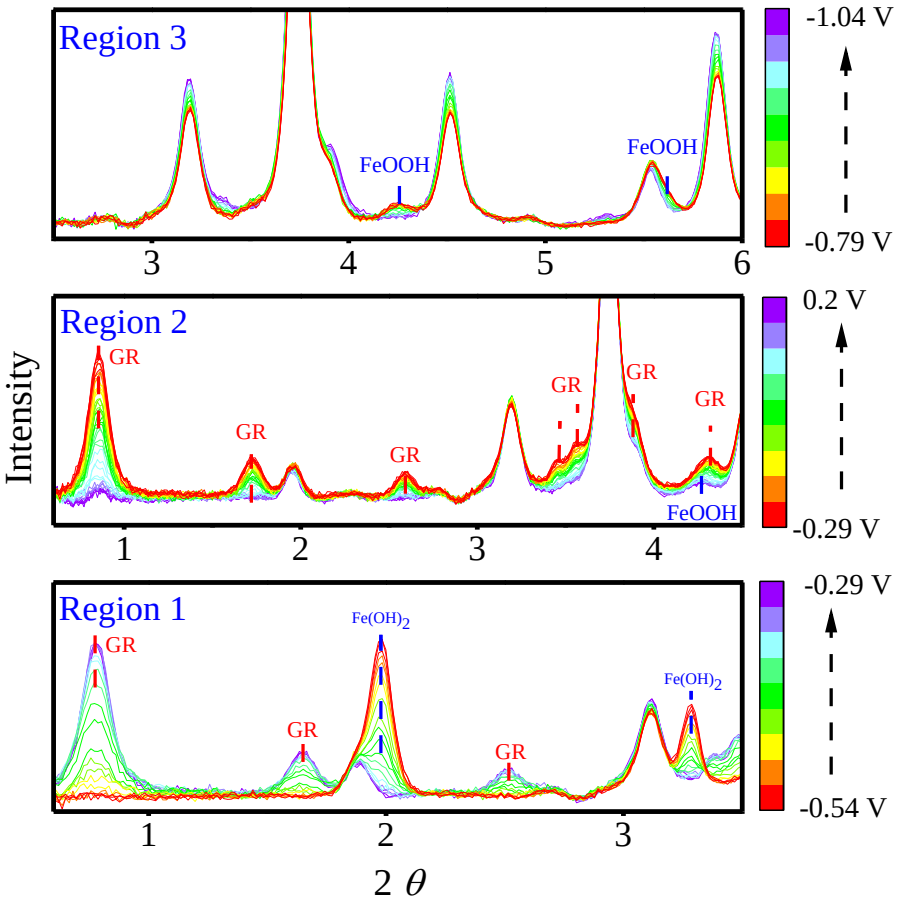

Figure 3.20 Picked regions of the *in-situ* XRD patterns from the cocktail electrolytes consisting of 0.1 M NaOH with 0.45 M Na_2SO_4

Figure 3.19 and **Figure 3.20** clearly showed that phase changes (emerge or disappearance of crystalline phases) happened during the electrochemical process, drastically different from insertion-type of reactions where only peak shifting happened during the electrochemical process as the structure of the host material did not change during the insertion/extraction of ions.

Table 3.2 Lattice parameters of green rust obtained from refinement using *GSAS-II*.

Phase	Space group	Lattice parameters					
		a (Å)	b(Å)	c(Å)	α(°)	β(°)	γ(°)
Green rust	P -3 1 m	5.5074	5.5074	11.026	90	90	120

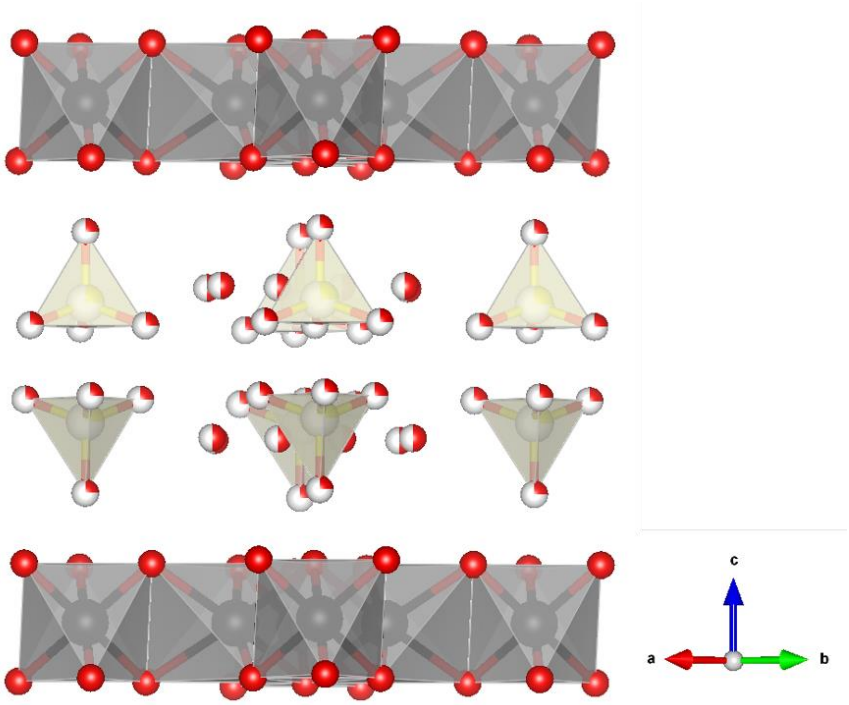

Figure 3.21 Modified structure of green rust: red dot represents an oxygen atom, black dot represents an iron atom, yellow dot represent sulfur atom. Hydrogen atoms are not shown in the structure. Site occupancy was represented by the dot occupancy.

Notably, the new phase of green rust was identified and fitted with a published structure file, which was built from *Simon*'s work.[133] The structure file was modified with the XRD pattern obtained at -0.31 V, around which potential the GR phase showed the most significant diffraction peaks. The obtained lattice cell parameters of GR phase were listed in **Table 3.2**, and the corresponding atomic structure generated by the software VESTA was shown in **Figure 3.21**.[137]

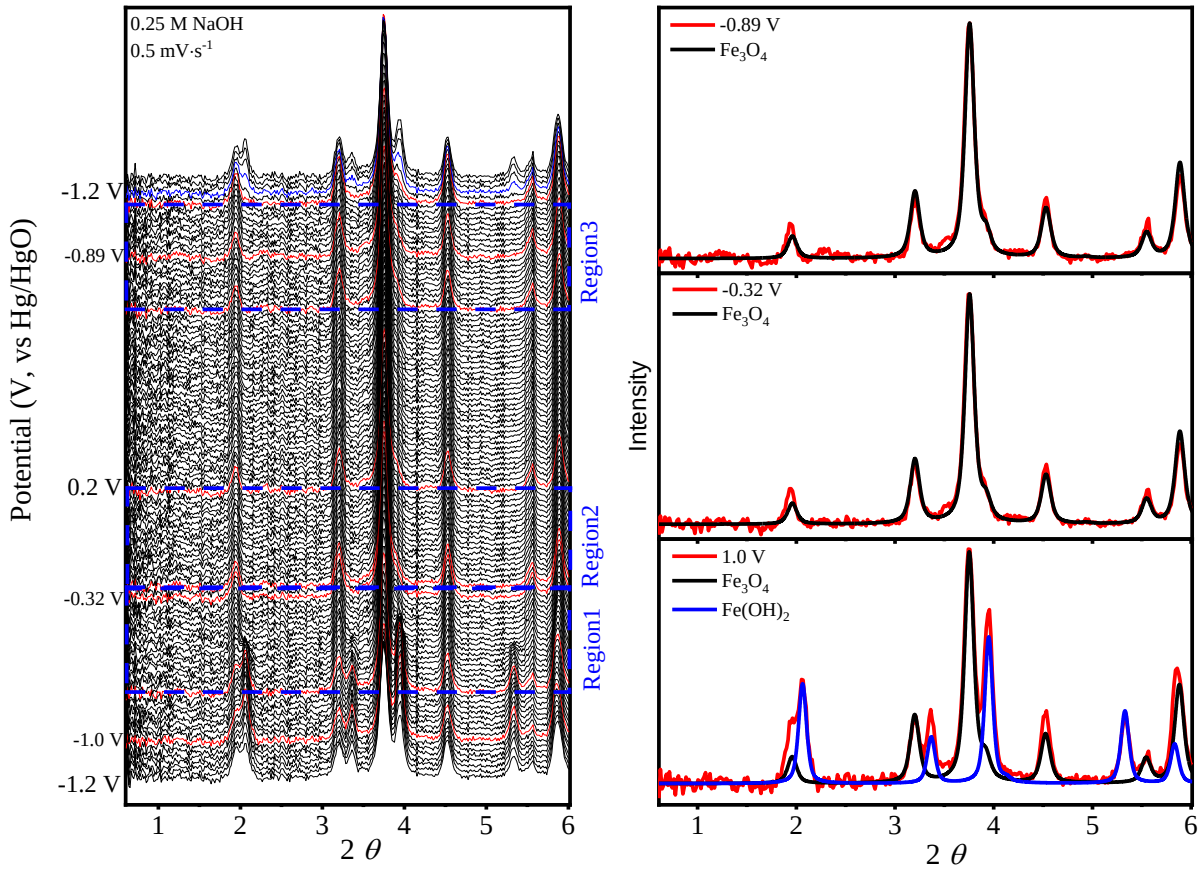

Figure 3.22 Waterfall plot of *in-situ* XRD patterns and picked individual XRD patterns from the 0.25 M NaOH electrolyte.

A waterfall plot of the *in-situ* XRD patterns and some selected individual patterns from pure NaOH electrolyte were shown in **Figure 3.22** and **Figure 3.23**. The potential window also ranged from -1.2 V to 0.2 V, following -1.2 V → 0.2 V →-1.2 V. An additional region of -1.2 V

to -1.06 V was included to better illustrate the formation of $Fe(OH)_2$. At -1.0 V, the identified phases were Fe_3O_4 and $Fe(OH)_2$, the same phase compositions in cocktail electrolytes. In Region 1 from -0.78 V to -0.66 V in the oxidization scan, the decreasing of $Fe(OH)_2$ was observed but without a new phase formation and from -0.66 V to -0.27 V. The individual pattern at -0.32 V and the picked Region 2 from -0.27 V to 0.18 V in the oxidization scan also showed only Fe_3O_4 existed after the $Fe(OH)_2$ phase diminished. At -0.89 V and the whole Region 3 from -0.64 V to -1.14 V in the reduction scan, the XRD patterns were exclusively attributed to Fe_3O_4.

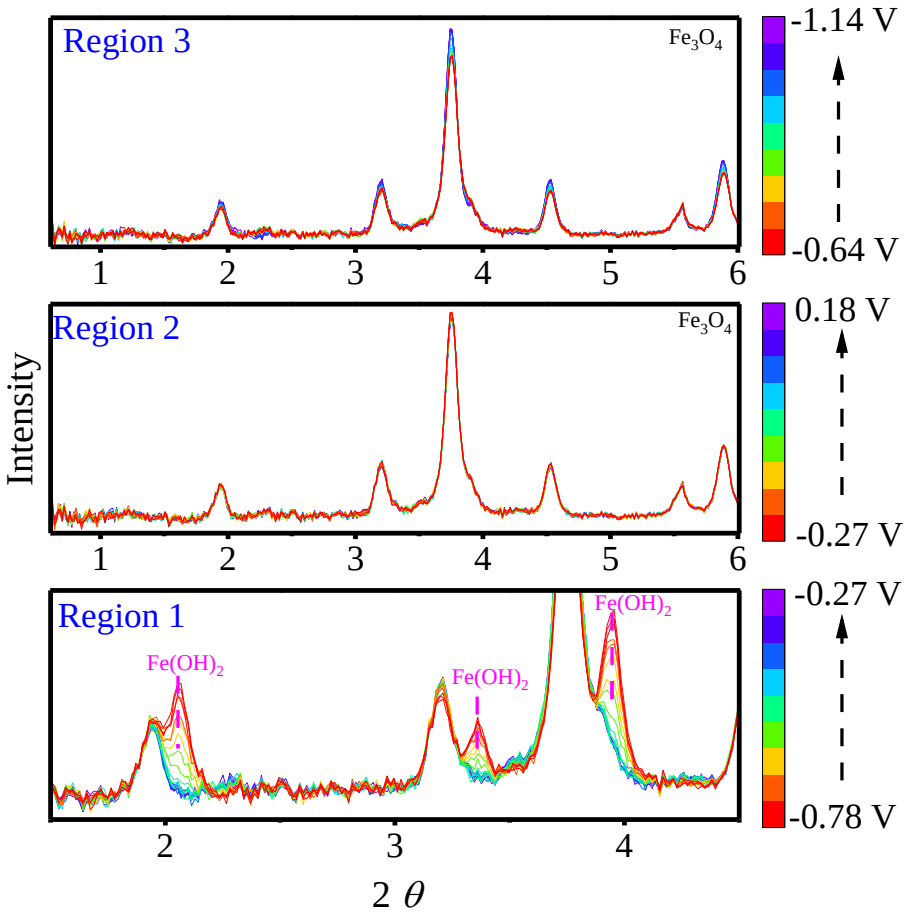

Figure 3.23 Picked regions of the *in-situ* XRD patterns from the 0.25 M NaOH electrolyte.

A minor amount of α-FeOOH was formed during the oxidization stage with pure NaOH electrolyte and later reduced to Fe_3O_4, evidenced in **Figure 3.24**. However, the signal was too weak to get a reliable refinement with α-FeOOH. Thus, α-FeOOH phase fraction was not included in the refinement.

Clearly, the difference between the two electrolytes was the formation of GR in the cocktail electrolyte and a significant amount of FeOOH formed in the cocktail electrolyte. It was worth pointing out that the Fe_3O_4 phase existed in all the potential regions in both electrolytes.

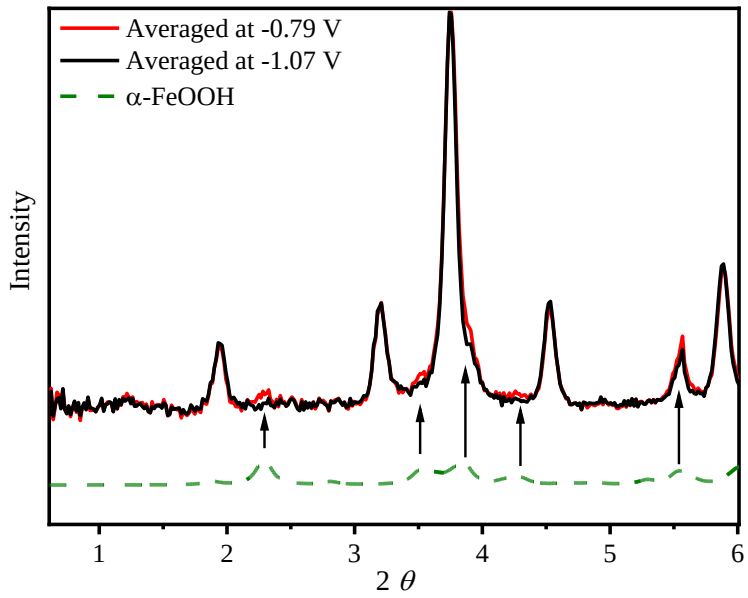

Figure 3.24 Evidence of the existence of α-FeOOH.

A thorough refinement of the entire region of each electrolyte shown in the above figures was conducted, and the results were shown in **Figure 3.25** and **Figure 3.26**. As mentioned before, the Fe_3O_4 phase existed in all potential regions. For the sake of clarity, only the part of Fe_3O_4 that was involved in the electrochemical process was considered in the phase analysis. Specifically, during the reduction region and the beginning part of the oxidization scan, where the current was still negative, Fe_3O_4 was reduced to $Fe(OH)_2$. Eventually, part of Fe_3O_4 would not participate in

the redox process and be considered inert. This portion would then be subtracted from the analysis and setting the molar fraction of $Fe(OH)_2$ as 100 % at this point. The results of phase analysis were presented in the form of molar fraction of total Fe atoms.

In the oxidization scan with cocktail electrolyte, $Fe(OH)_2$ can be directly oxidized to Fe_3O_4, following Equation 3.5:

$$3Fe(OH)_2 + 2OH^- \rightarrow Fe_3O_4 + 4H_2O + 2e^- \quad \text{Equation 3.5}$$

With the potential increase to ~ -0.48V, $Fe(OH)_2$ can be oxidized alternatively to Green Rust (GR), following Equation 3.6:

$$6Fe(OH)_2 + {SO_4}^{2-} \rightarrow {Fe^{2+}}_4\,{Fe^{3+}}_2(OH^-)_{12}SO_4 + 2e^- \quad \text{Equation 3.6}$$

Approximately 42 % of GR would be further oxidized to δ-FeOOH, with the rest being oxidized to Fe_3O_4, following Equation 3.7 and Equation 3.8, respectively.

$${Fe^{2+}}_4\,{Fe^{3+}}_2(OH^-)_{12}SO_4 + 6OH^- \rightarrow 6FeOOH + {SO_4}^{2-} + 6H_2O + 4e^- \quad \text{Equation 3.7}$$

$${Fe^{2+}}_4\,{Fe^{3+}}_2(OH^-)_{12}SO_4 + 4OH^- \rightarrow 2Fe_3O_4 + {SO_4}^{2-} + 8H_2O + 2e^- \quad \text{Equation 3.8}$$

The phase fraction of δ-FeOOH remained roughly stable after the GR diminished at 0.15 V. The formation of δ-FeOOH could likely entirely be attributed to the oxidization of GR. Fe_3O_4 would unlikely be oxidized to δ-FeOOH. Otherwise, the phase fraction of δ-FeOOH would be increasing with the potential increase to higher values.

In the following reduction scan, δ-FeOOH was reduced to Fe_3O_4, following Equation 3.9. With the potential continued to decrease, Fe_3O_4 was further reduced to $Fe(OH)_2$, following the reversed reaction described in Equation 3.5.

$$3FeOOH + e^- \rightarrow Fe_3O_4 + H_2O + OH^- \quad \text{Equation 3.9}$$

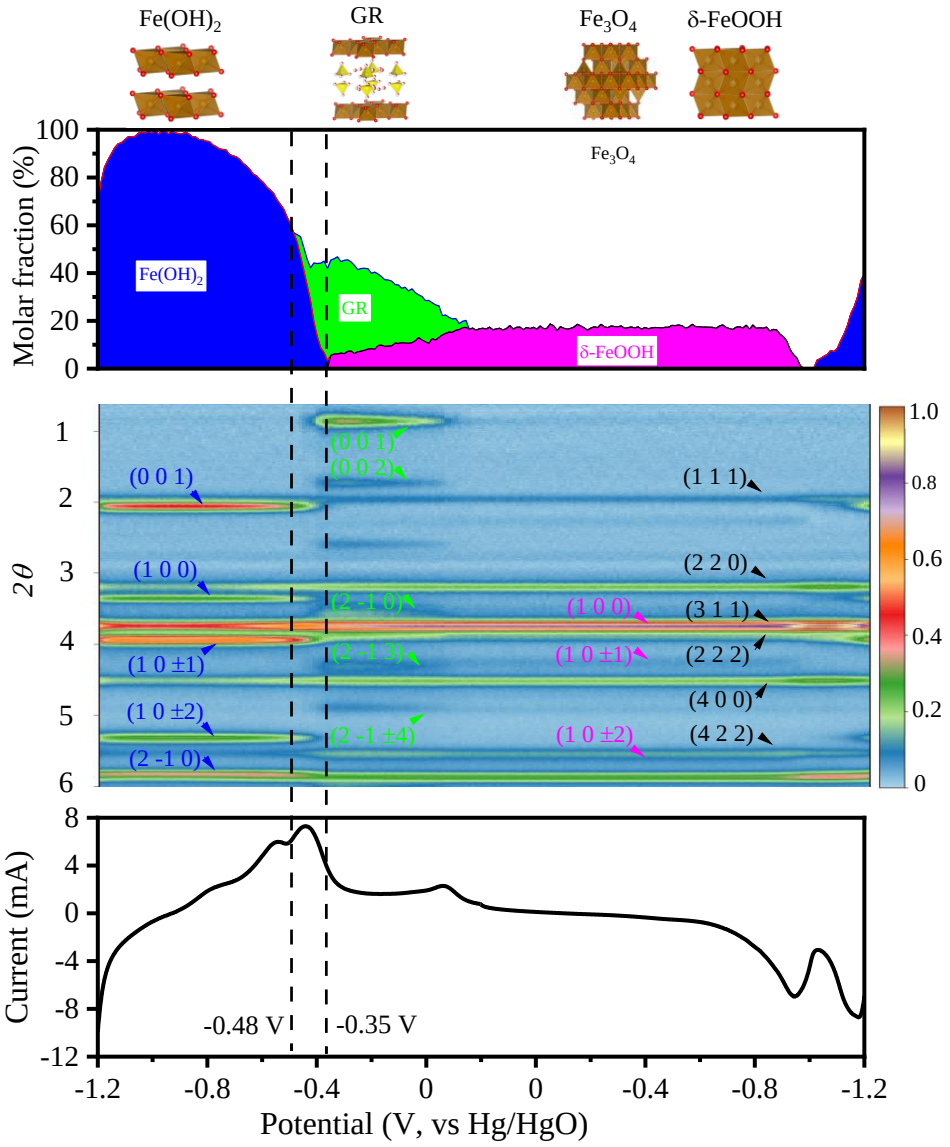

Figure 3.25 Phase analysis of *in-situ* XRD with cocktail electrolyte consisting of 0.1 M NaOH and 0.45 M Na_2SO_4.

In contrast, the redox reaction only involved $Fe(OH)_2$ and Fe_3O_4 phases without forming green rust when pure NaOH electrolyte was used. It was because Fe_3O_4 was a relatively stable phase and difficult to be further oxidized into FeOOH. Fe_3O_4 would then be reduced to $Fe(OH)_2$ in the

reduction region. Overall, the redox reaction in pure NaOH electrolyte was limited to $Fe(OH)_2 \leftrightarrow Fe_3O_4$.

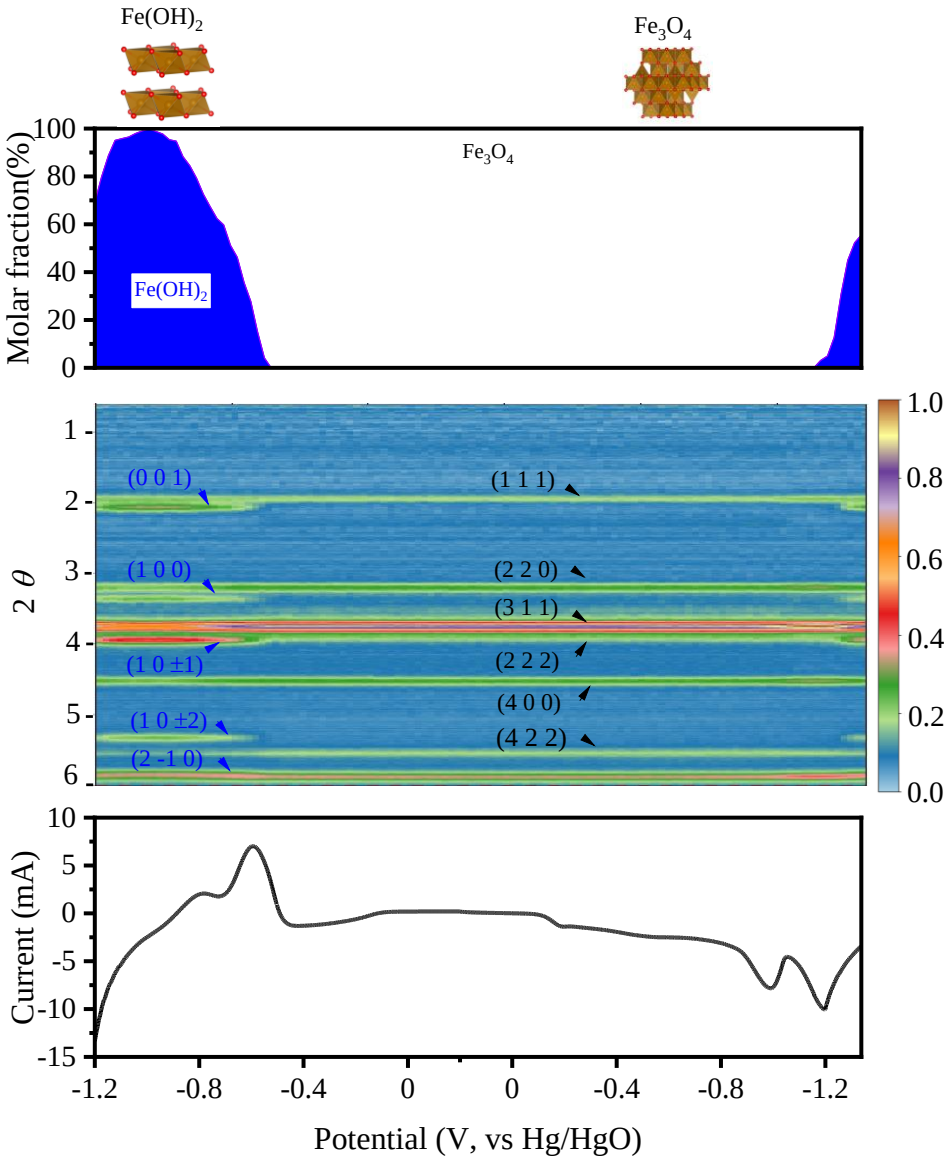

Figure 3.26 Phase analysis of *in-situ* XRD with 0.25 M NaOH as electrolyte.

3.3.3 PROPOSED REACTION MECHANISM OF LEPIDOCROCITE IN ALKALINE SYSTEM

In summary, a reaction mechanism can be proposed as following: in the pure NaOH electrolyte, the oxidization reaction followed reaction pathway 1:

$$Fe(OH)_2 \rightarrow Fe_3O_4 \qquad \text{Reaction pathway 1}$$

While in the cocktail electrolyte, the presence of SO_4^{2-}, there was alternative reaction pathway 2 in addition to reaction pathway 1 for the oxidization of $Fe(OH)_2$:

$$Fe(OH)_2 \rightarrow GR \rightarrow FeOOH \qquad \text{Reaction pathway 2}$$

Although GR could partially be oxidized to Fe_3O_4, this portion, however, could be included in reaction pathway 1. Reaction pathway 2 competed with reaction pathway 1. The previous half-cell CV measurements indicated that lower pH favored reaction pathway 2.

Reaction pathway 2 was beneficial in two aspects. First, it ensured a more significant charge transfer in the redox reaction, resulting in a larger capacity, as shown in previous CV measurements. Second, this reaction pathway avoided the formation of Fe_3O_4 in the oxidization scan, which was beneficial for the long-term cyclability as Fe_3O_4 was relatively electrochemically inert.

To further prove that the cocktail electrolyte helps form FeOOH, which is beneficial for a battery reaction since it provides more charge transfer, XPS measurements were conducted to see the valance states of the oxidized materials from both electrolytes.

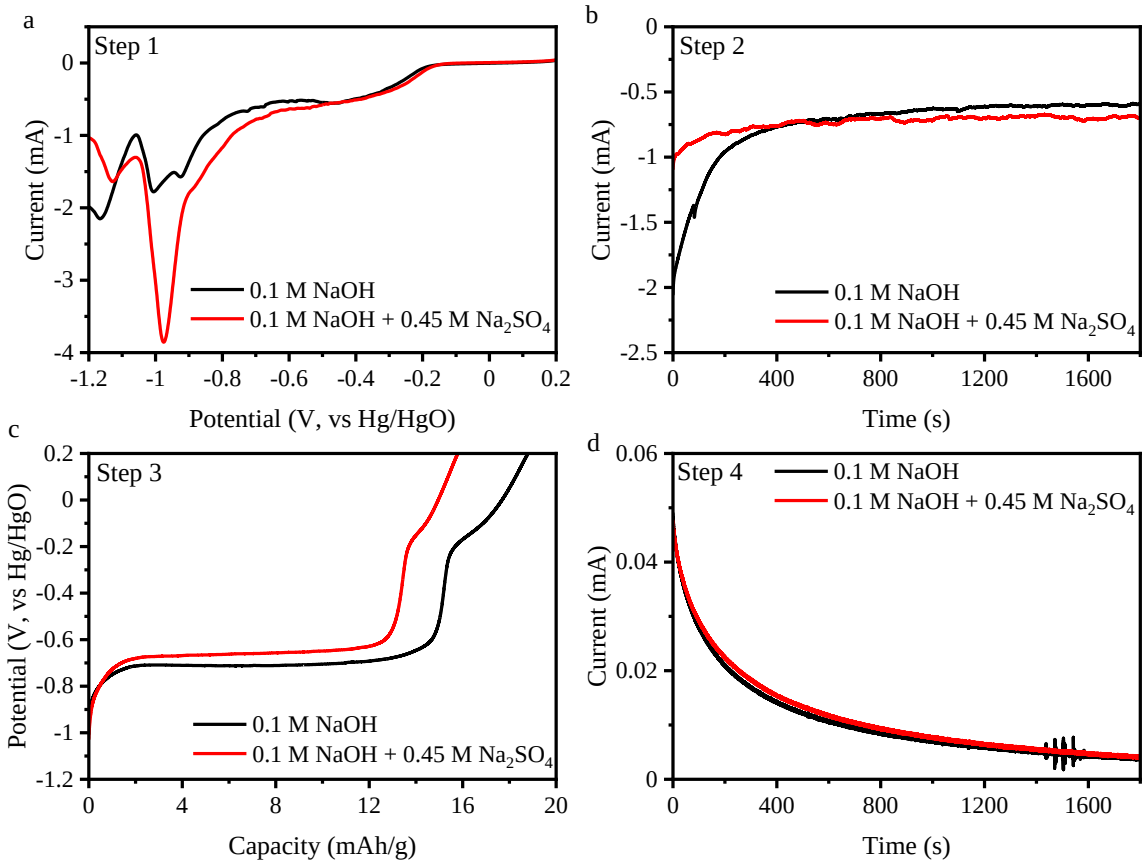

Figure 3.27 Electrochemical preparation for XPS measurement: **(a)** step 1: CV at 0.5 $mV \cdot s^{-1}$ from 0.2 V to -1.2 V; **(b)** step 2: holding at -1.2 V for 30 min; **(c)** step 3: CP at 0.021 $A \cdot g^{-1}$ form -1.2 V to 0.2 V; **(d)** step 4: holding at 0.2 V for 30 min.

Specifically, to collect enough amount of samples for XPS measurements, the working electrode was prepared differently: the working electrode was prepared with drop-casting ~ 4 mg γ-FeOOH/carbon mixture black (mass ratio=7:3) onto Toray carbon paper, then covered with ~ 4 μL of Nafion solution (~ 5% of Nafion by mass). The measurements were conducted with 0.1 M NaOH with and without 0.45 M Na_2SO_4. The sample was first reduced to -1.2 V by CV measurement and hold at -1.2 V for 30 min, followed by a CP measurement at a current density of 0.021 $A \cdot g^{-1}$ from -1.2 V to 0.2 V, and finally hold at 0.2 V for 30 min. The results from the electrochemical preparation stages were shown in **Figure 3.27**. The relatively low discharge

capacity shown in **Figure 3.27 (c**) suggested that a limited amount of active materials were involved in the reaction, likely due to poor contact and ion transport limitations resulted from large loading. Based on the relatively significant differences shown in the XRS data, it was likely that the reactions only happened at the near surface of the electrodes.

The XPS data of Fe 2p of the oxidized samples were shown in **Figure 3.28**, and the C 1s spectra were shown in **Figure 3.29**. The XPS data of the oxidized sample from the cocktail electrolyte showed a much stronger satellite peak at 719 eV, which was the signature peak from Fe^{3+}, indicating a higher ratio of Fe^{3+}/Fe^{2+}.[138,139]

The XPS data demonstrated that the oxidization product from the cocktail electrolyte had a higher valance state, congruent with the XRD results showing the formation of FeOOH at high voltage when the cocktail electrolyte was used.

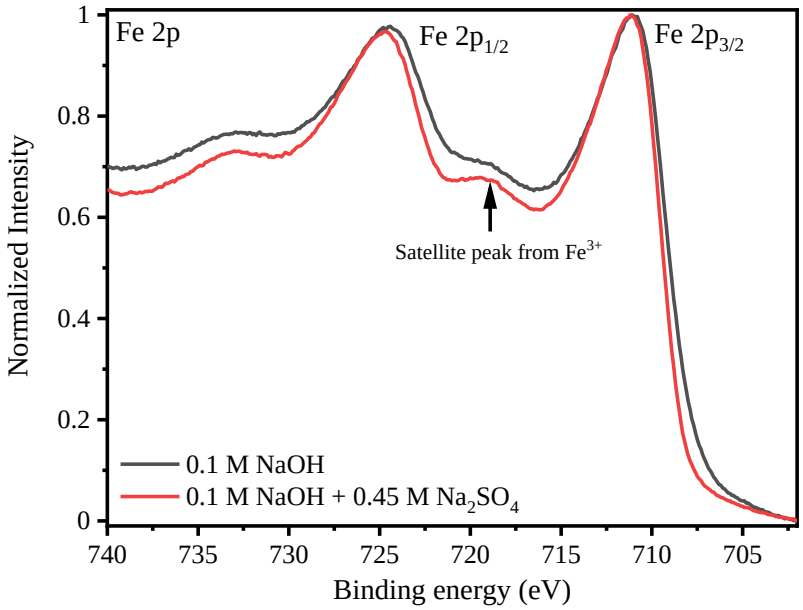

Figure 3.28 XPS of Fe 2p from oxidized sample measured with different electrolytes.

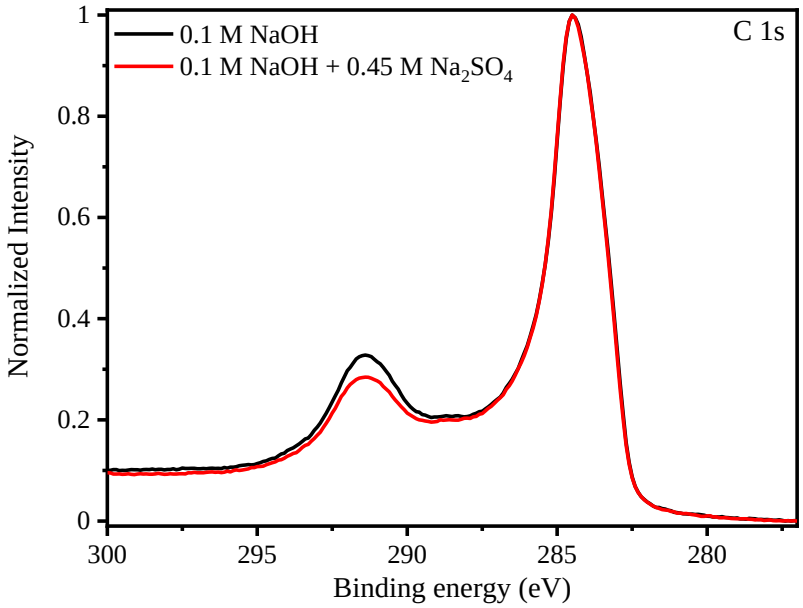

Figure 3.29 XPS of C 1s from oxidized sample measured with different electrolytes.

CHAPTER 4 PERFORMANCE OF LEPIDOCROCITE AS THE ANODE FOR BATTERY APPLICATIONS

With the understanding of the reaction mechanism of γ-FeOOH under the alkaline system, it is also critical to investigate its performance for battery application. As mentioned previously, CP measurements worked at a similar condition with an actual battery device. It was important to investigate the performance of the studied material under CP measurements and evaluate the long-term cyclability. Two forms of CP measurements were conducted. One was conducted in a three-electrode half-cell, and the other was conducted using a two-electrode asymmetric full-cell.

4.1 CP MEASUREMENTS IN THREE-ELECTRODE HALF-CELL SYSTEM

4.1.1 THE EXPLORATION OF OPERATIONAL POTENTIAL WINDOW

CP measurements were first conducted in a three-electrode half-cell system. Similar to half-cell CV measurements, half-cell CP measurements were ideal for investigating the intrinsic electrochemical properties of the studied material, as external diffusion limitations can be significantly minimized due to a small amount of the active electrode materials on the surface of a working electrode (microgram-level loading). To explore the potential window that can be used for CP measurements, the lower limit of the potential window was first set at -1.7 V. As shown in **Figure 4.1**, the lowest potential during reduction that can be reached was around -1.2 V, and the following plateaus were both at even higher potentials. Since complete reduction from FeOOH to $Fe(OH)_2$ yields a theoretical capacity of ~300 $mAh \cdot g^{-1}$, the following plateau extended to 800 $mAh \cdot g^{-1}$ was likely from HER and/or metallic iron formation. The formation of metallic iron from $Fe(OH)_2$ occurs at -0.90 V when pH is equal to 12 during reduction, accompanying HER that happens at -0.85 V. Therefore, the potential increase during reduction

likely resulted from iron formation, whereas iron could catalyze HER and decrease the potential during the CP test.

Thus, the lower limit of the potential window chosen for half-cell CP measurements was set to be -1.05 V to avoid HER. Previous CV measurements showed that the peaks in the oxidization scan were around -0.6 V and -0.48 V in a mixture of 0.01 M NaOH and 0.2 M Na_2SO_4 electrolytes at a scan rate of 1 $mV \cdot s^{-1}$. Therefore, the upper potential limit of CP measurements was set at -0.35 V so that the potential window was large enough to cover the redox reactions.

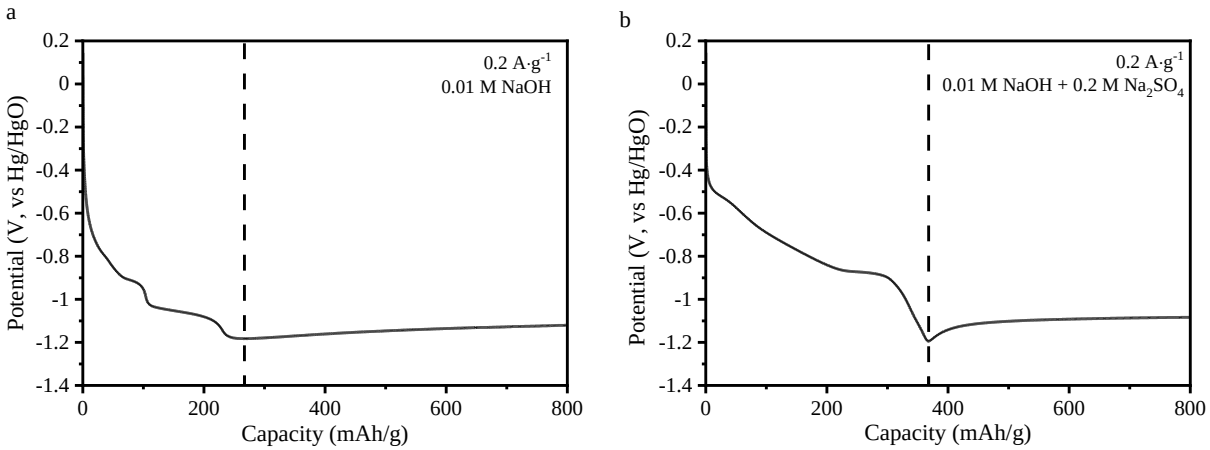

Figure 4.1 Exploration of the potential window for CP measurements of γ-FeOOH in **(a)** 0.01 M NaOH; **(b)** 0.01 M NaOH with 0.2 M Na_2SO_4.

4.1.2 CP MEASUREMENTS OF LEPIDOCROCITE WITH A POTENTIAL WINDOW FROM -1.05 V TO -0.35 V

Similarly, the first reduction segment was different from the following reduction segments, as shown in **Figure 4.2**. In pure NaOH, there were multiple plateaus in the first reduction segment at around -0.78 V, -0.82 V, -0.90 V, and -1.03 V, while in the second reduction segment, there was only one observable plateau at around -0.78 V. In the cocktail electrolyte, two plateaus appeared at around -0.79 V and -0.92 V in the first reduction segment and emerged at around -

0.5 V and -0.85 V in the following reduction segments, respectively. The difference between the first reduction segment and the following reduction segments was likely due to the structural difference between the materials as-synthesized and the oxidization product formed during the electrochemical process. The synthesized material was identified as a mixture of iron oxide and iron oxyhydroxide, dominantly γ-FeOOH. However, as suggested by *in-situ* XRD measurements, the oxidization product was Fe_3O_4 in pure NaOH electrolyte and a mixture of Fe_3O_4 and δ-FeOOH in the cocktail electrolyte. Thus, the first reduction segment would be regarded as the activation process.

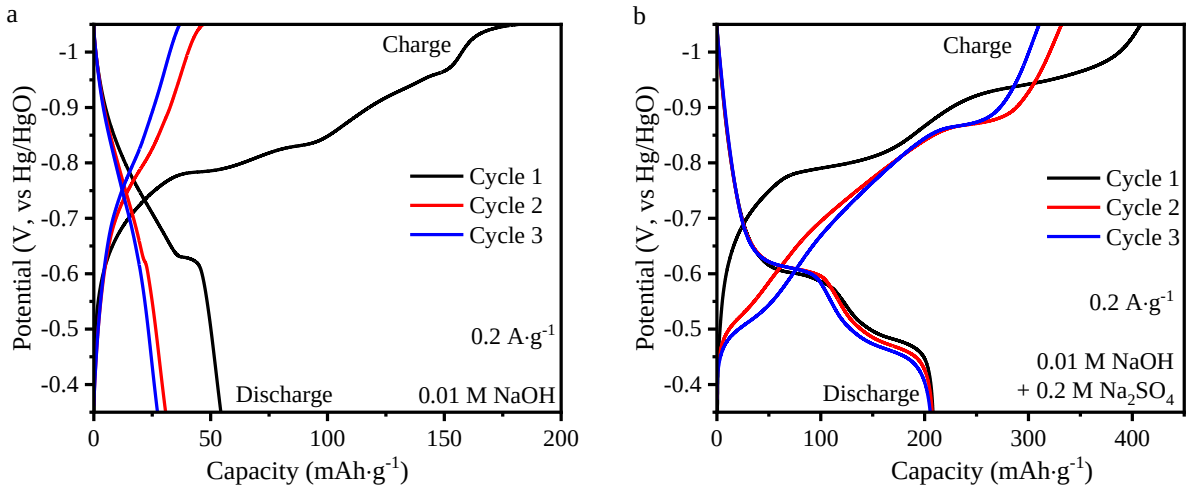

Figure 4.2 First 3 cycles of CP measurements of γ-FeOOH in different electrolytes: **(a)** 0.01 M NaOH; **(b)** 0.01 M NaOH with 0.2 M Na_2SO_4.

Figure 4.3 shows the second charge/discharge cycle of γ-FeOOH in pure NaOH electrolyte, separated from **Figure 4.2** and paired with the dC/dV curve (the 1st order derivative of capacity with respect to potential). It was clear that the capacity was much lower than that in CV measurements and a minimal discharge plateau around -0.6 V. There was a broad plateau around -0.8 V in the reduction scan, suggesting a new phase formation during the reduction process. The

dC/dV curve shown in **Figure 4.3 (b)** has an intensive but incomplete peak at potential below -1.0 V, possibly due to the incomplete reduction from Fe_3O_4 to $Fe(OH)_2$.

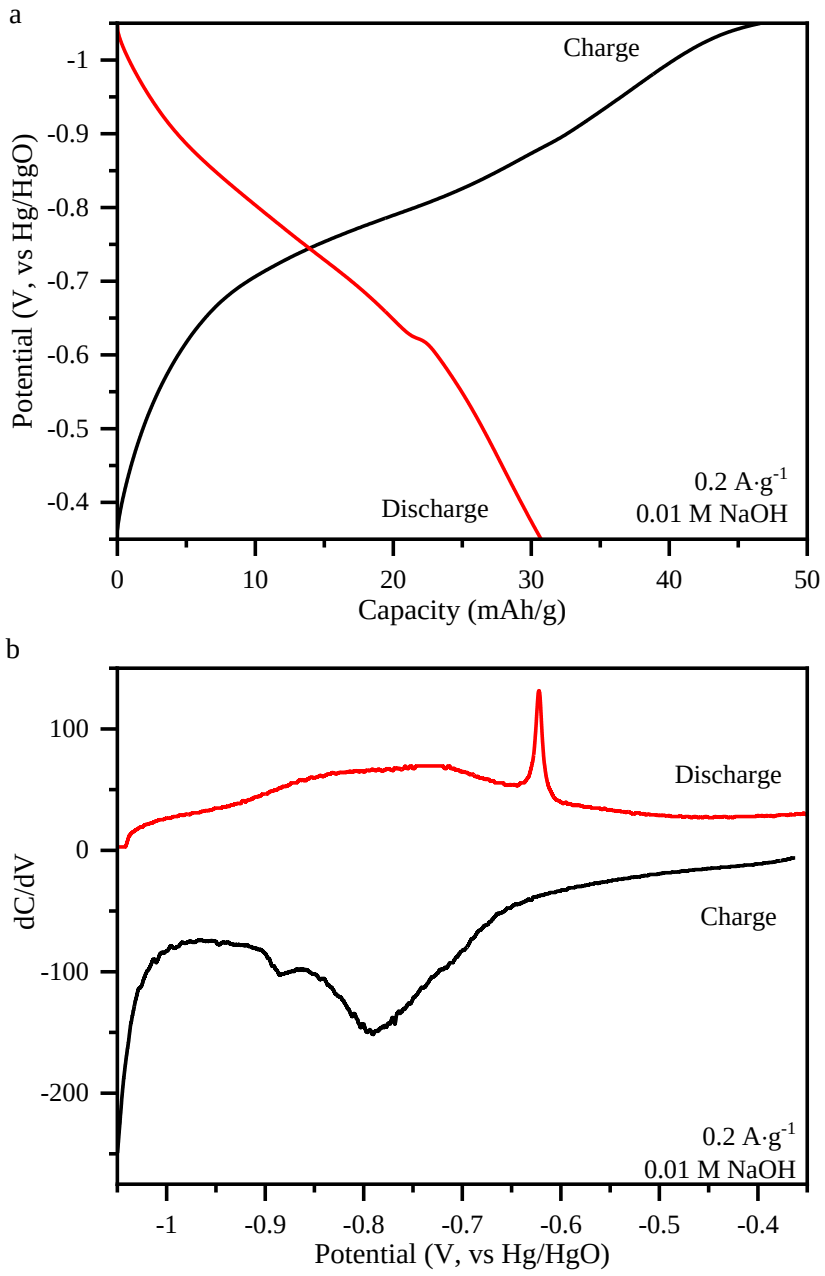

Figure 4.3 (a) 2nd cycle of CP measurement of γ-FeOOH and **(b)** the corresponding dC/dV curve in in 0.01M NaOH.

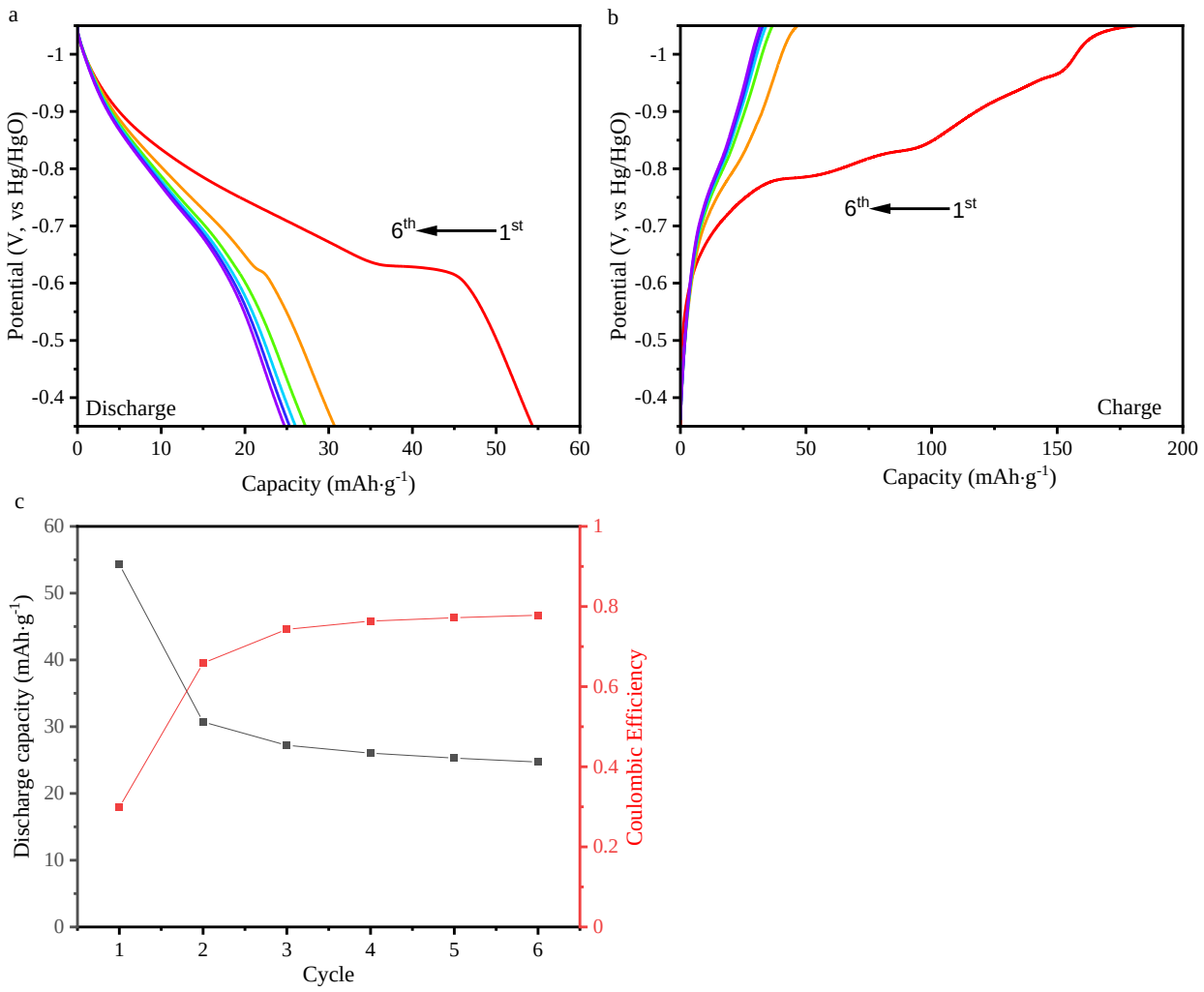

Figure 4.4 CP results of γ-FeOOH in 0.01 M NaOH: **(a)** The first 6 discharge segments; **(b)** the first 6 charge segments; **(c)** the coulombic efficiencies of the first 6 cycles.

The first six charge and discharge cycles of γ-FeOOH in pure NaOH electrolyte were plotted in **Figure 4.4 (a, b)**, and the corresponding columbic efficiency, the ratio between charge and discharge capacities, were shown in **Figure 4.4 (c)**. **Figure 4.4 (a)** showed that the discharge plateau around -0.6 V decreased rapidly from the first cycle to the second cycle and disappeared at the third cycle. The overall discharge capacity also dropped rapidly from 54 $mAh \cdot g^{-1}$ at the first cycle to 31 $mAh \cdot g^{-1}$ at the second cycle and stabilized from the third cycle slightly below 30 $mAh \cdot g^{-1}$. As indicated from the *in-situ* XRD, the plateau around -0.6 V was likely attributed to

the oxidization of $Fe(OH)_2$ to Fe_3O_4. The disappearance of this plateau suggested that $Fe(OH)_2$ formation was incomplete in the previous reduction segments.

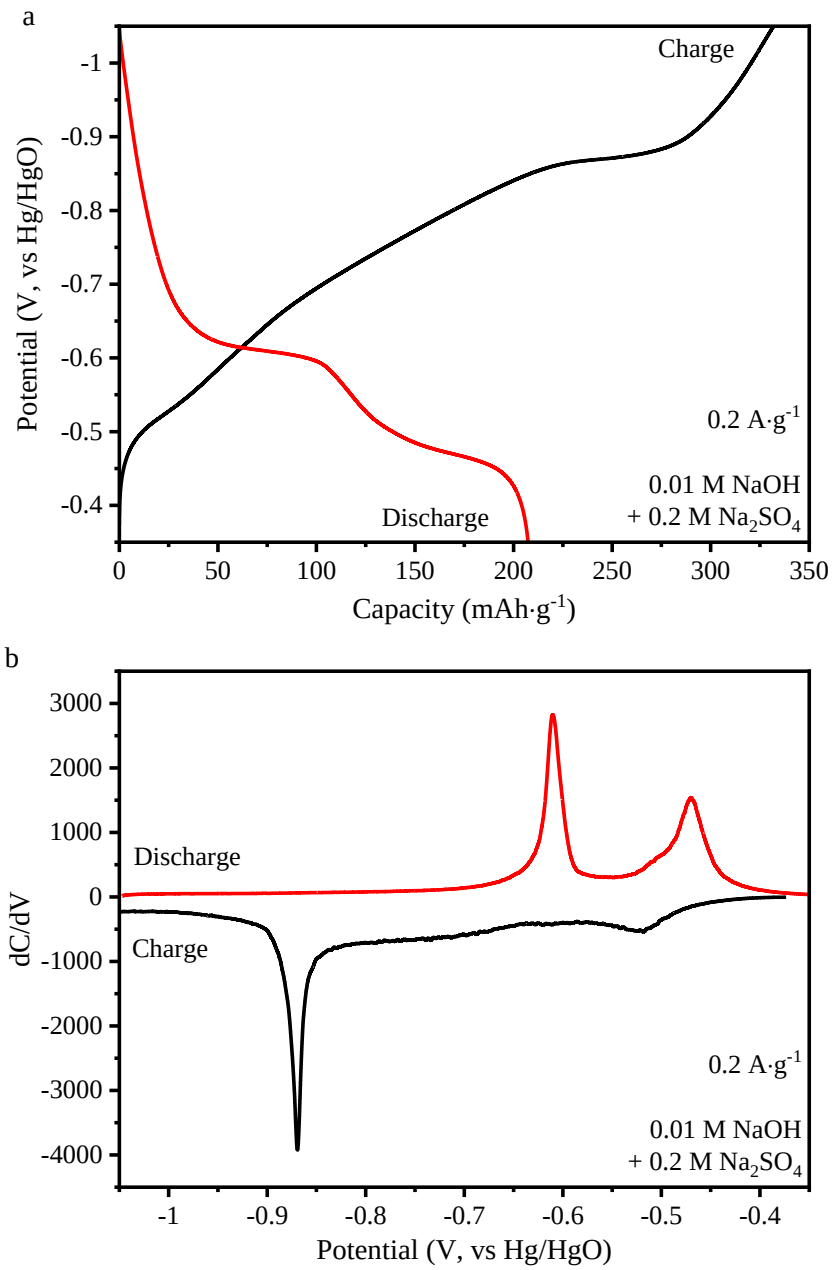

Figure 4.5 (a) 2nd cycle of CP measurement of γ-FeOOH and **(b)** the corresponding dC/dV curve in 0.01 M NaOH with 0.2 M Na_2SO_4.

The effect of the addition of Na_2SO_4 was also investigated using CP measurements. The second cycle of the charge/discharge profile of γ-FeOOH in the cocktail electrolyte and the corresponding dC/dV curves were plotted in **Figure 4.5**.

Unlike in the CV measurements, where the addition of Na_2SO_4 attributed to a 50% increase in capacity, the addition of Na_2SO_4 in CP measurement increased the discharge capacity from 31 $mAh \cdot g^{-1}$ to 207 $mAh \cdot g^{-1}$ in the second cycle. Also, unlike the CV measurements where the second oxidization peak at -0.48 V was relatively small, the plateau at around -0.46 V from CP tests was more significant and contributed roughly the same capacity to the overall capacity as the first plateau at around -0.6 V. This significant increase could be attributed to the nearly complete formation of $Fe(OH)_2$ during the reduction segments, providing more reactants to oxidize in the discharge segment. Notably, the CP measurements were typically conducted in slower charge transfer rates than CV measurements, and the redox reaction in the CP test would be nearly thorough due to the decreased overpotential.

As suggested from the *in-situ* XRD results, there were likely two reaction pathways during the oxidization in the cocktail electrolytes. The reduction product $Fe(OH)_2$ could directly be oxidized to Fe_3O_4, and it could also be first oxidized to GR and further oxidized to either Fe_3O_4 or FeOOH. The two reaction pathways likely resulted in different reaction kinetics. Therefore, discharging at various current densities were also conducted to investigate the effect of reaction kinetics on the distribution of these two reaction pathways and would be discussed later in this section.

The first 6 charge and discharge cycles of γ-FeOOH in the cocktail electrolyte and the corresponding columbic efficiencies were plotted in **Figure 4.6**. In contrast to the sharp decrease in discharge capacity from the first to the second cycle in pure NaOH electrolyte, the capacity

remained roughly stable around 200 mAh·g^{-1} over the first 6 cycles. It was worth mentioning that the coulombic efficiency was under 80% in both electrolytes, which was still unsatisfactory for a battery system.

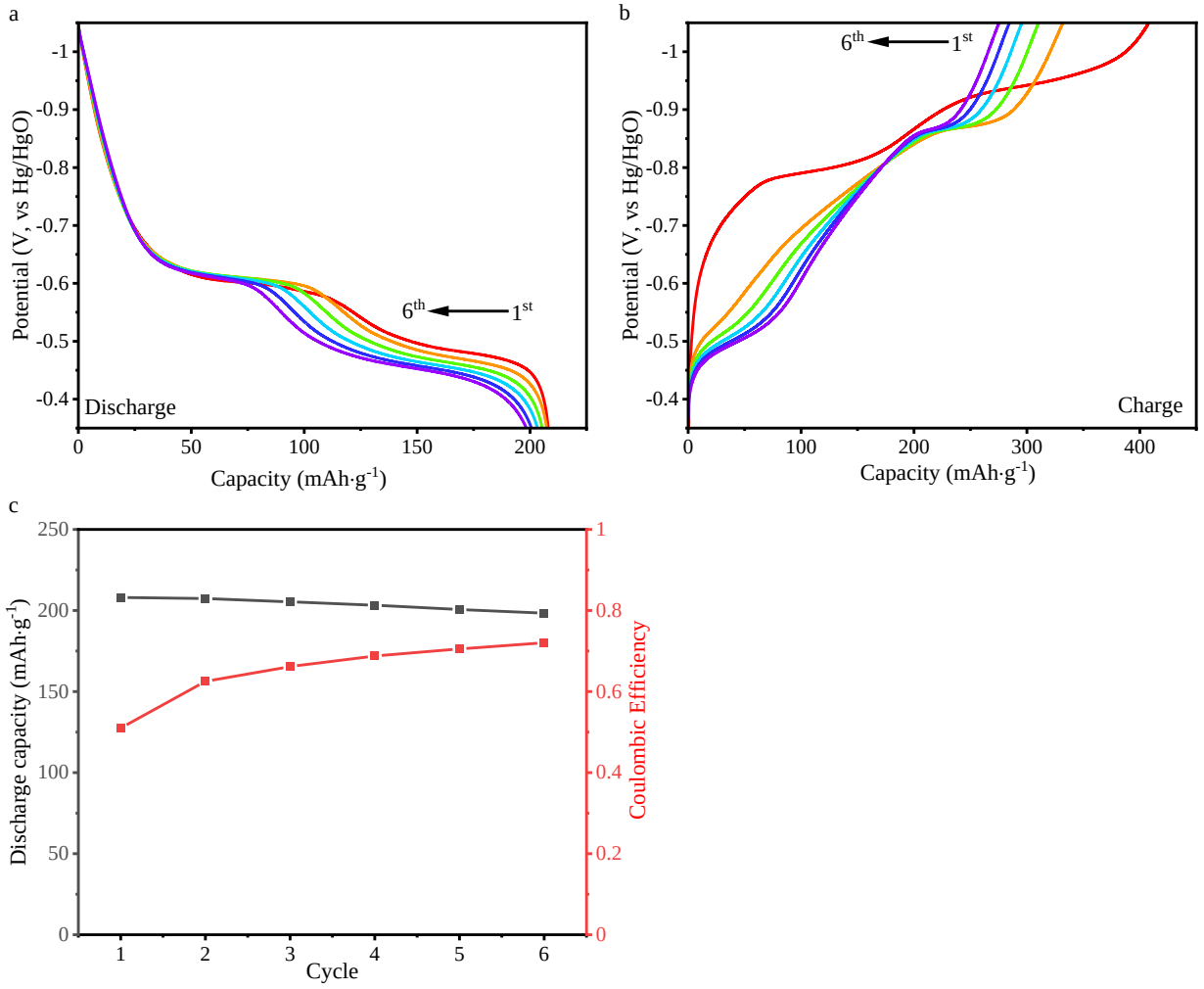

Figure 4.6 CP results of γ-FeOOH in 0.01 M NaOH with 0.2 M Na_2SO_4: **(a)** The first 6 discharge segments; **(b)** the first 6 charge segments; **(c)** the coulombic efficiencies of the first 6 cycles.

Aside from the intrinsic irreversibility of the reaction, the low coulombic efficiency was likely due to oxygen reduction reaction (ORR) during the reduction segments, which could also explain the unbalanced CV curve in the *in-situ* measurement (**Figure 3.14**). Although the half-cell CP

measurements were conducted under the protection of Argon, the formation of oxygen on the counter electrode still could not be avoided. ORR as the side reaction could occur during the entire reduction segment. These issues could be improved by using a two-electrode full-cell system that was well sealed and without a counter electrode. The electrochemical measurements conducted with full-cells showed a better coulombic efficiency, which will be discussed later in **Section 4.2**.

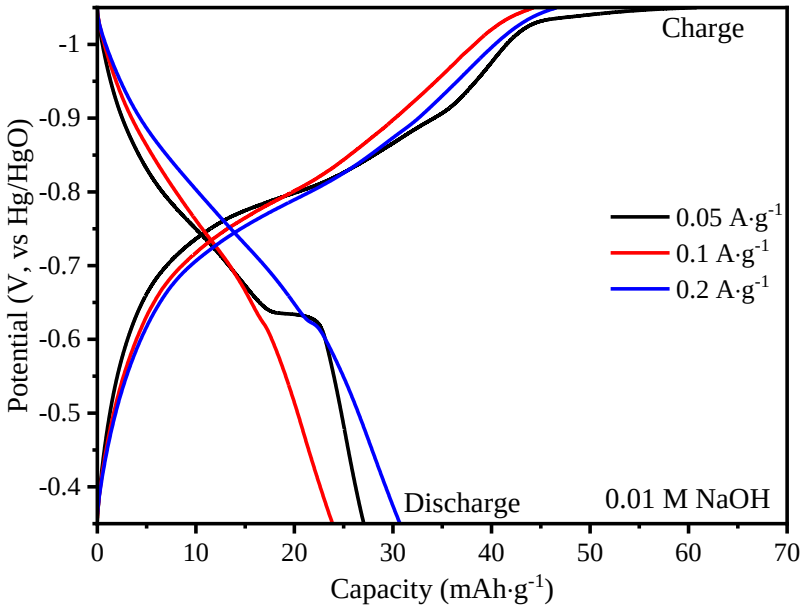

Figure 4.7 2nd cycle of CP measurement of γ-FeOOH at different current densities in 0.01 M NaOH.

The CP measurements were also conducted with lower current density, including 0.05 $A \cdot g^{-1}$ and 0.1 $A \cdot g^{-1}$. The results of the second cycle are shown in **Figure 4.7** and **Figure 4.8**. In pure NaOH electrolyte, the reduction plateau around -1.02 V at 0.05 $A \cdot g^{-1}$ and the oxidization plateau at around -0.6 V were more significant. But the overall discharge capacity remained low. In the cocktail electrolyte, low current density did not necessarily improve the overall discharge capacity significantly either. However, it was clear that the first oxidization plateau at -0.6 V

contributed less to the overall discharge capacity while the second oxidization plateau increased with decreasing current densities.

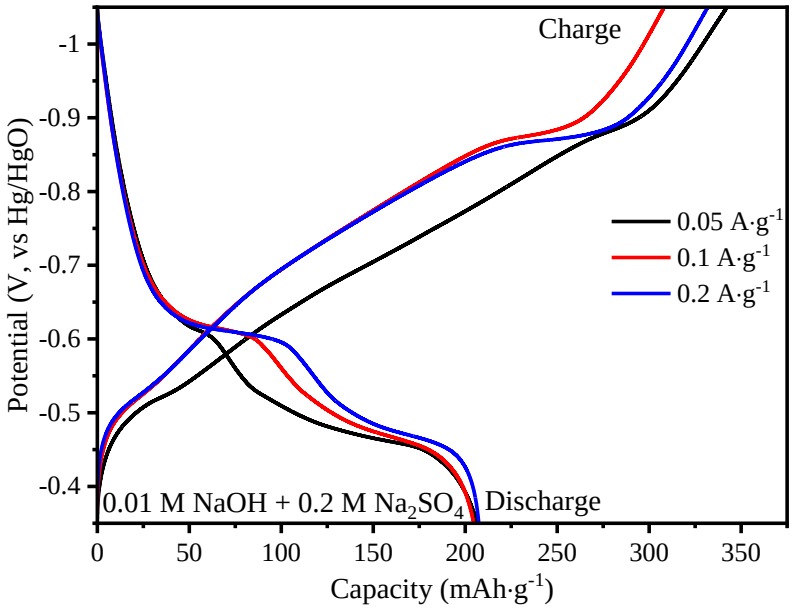

Figure 4.8 2nd cycle of CP measurement of γ-FeOOH at different current densities in 0.01 M NaOH with 0.2 M Na_2SO_4.

Figure 4.9 further highlights the capacity distribution resulting from two discharge plateaus. The first plateau at -0.6 V contributed 54.1% of the overall discharge capacity at 0.2 $A \cdot g^{-1}$, while it only contributed 33.7% at 0.05 $A \cdot g^{-1}$. As discussed previously, there were likely two competing reaction pathways occurring in the oxidization with cocktail electrolytes, and the pathway toward the formation of green rust was favored at low current density. The corresponding reduction plateau to the second oxidization plateau (around -0.46 V) was around -0.52 V, which made the potential separation between the oxidization and the reduction plateaus around 60 mV, suggesting relatively reversible oxidation/reduction processes.

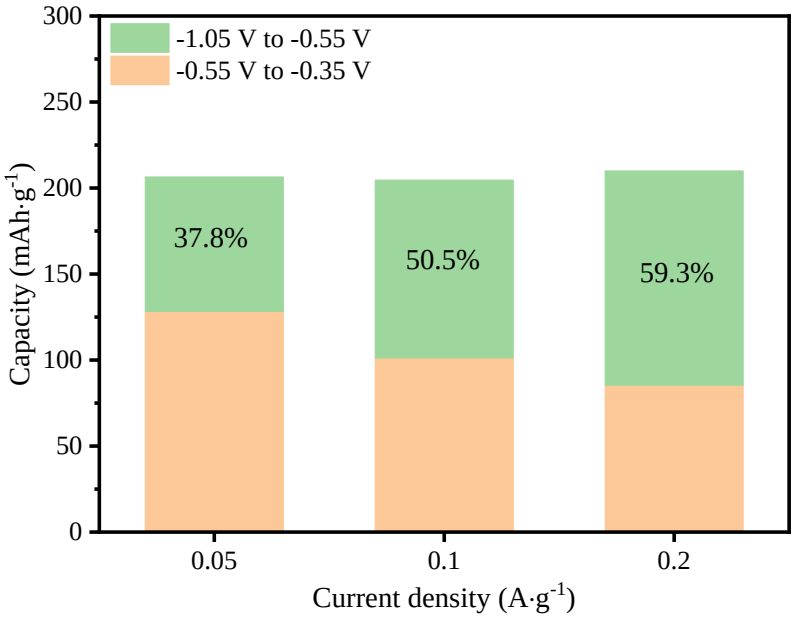

Figure 4.9 Capacity distributions at different current densities in 0.01 M NaOH with 0.2 M Na_2SO_4 electrolyte.

It was worth mentioning that lowering down current density in both electrolytes did not increase the discharge capacity greatly. Although the exact mechanism is still unclear, one possible reason was that lower current density required more reaction time, even if it did not increase the capacity. A longer measurement time might cause the disintegration of the materials on the working electrode, thus lowering the overall capacity. A full-cell device could minimize the detachment of materials from the electrode with pressure applied on the surface of both electrodes.

To further investigate the reaction kinetics, measurements with charging current density fixed at 0.2 $A \cdot g^{-1}$ and different discharging current densities (0.5 $A \cdot g^{-1}$, 1 $A \cdot g^{-1}$) were conducted, and the results were shown in **Figure 4.10** and **Figure 4.11**.

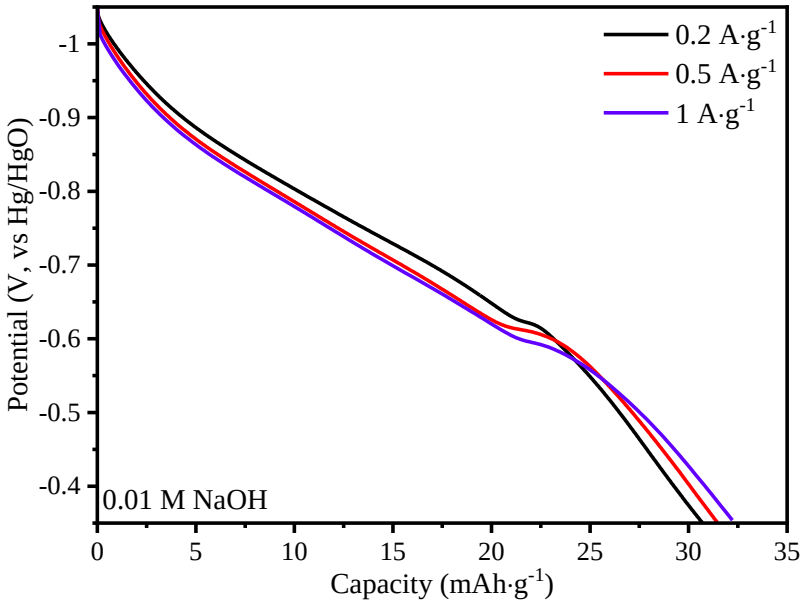

Figure 4.10 2nd discharge curves of CP measurements of γ-FeOOH at different current densities in 0.01 M NaOH.

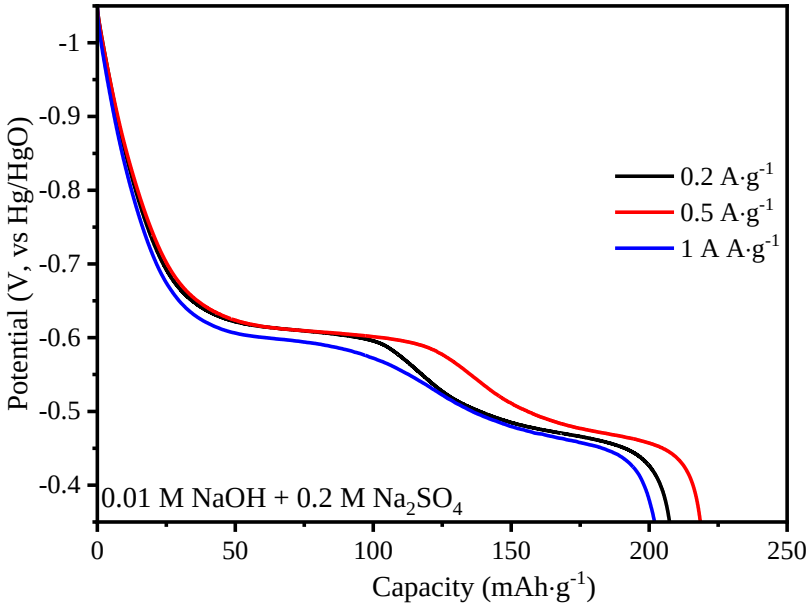

Figure 4.11 2nd discharge curves of CP measurements of γ-FeOOH at different current densities in 0.01 M NaOH with 0.2 M Na_2SO_4.

The reason to set the charging current density all at 0.2 $A \cdot g^{-1}$ was to eliminate the difference from the charge segment and focus on the discharge segment. Increasing discharge current density from 0.2 $A \cdot g^{-1}$ to 1 $A \cdot g^{-1}$ did not cause a significant difference between the discharge profile in either of the two electrolytes at the second cycle. However, a higher current density showed a decrease in capacity retention in the cocktail electrolyte.

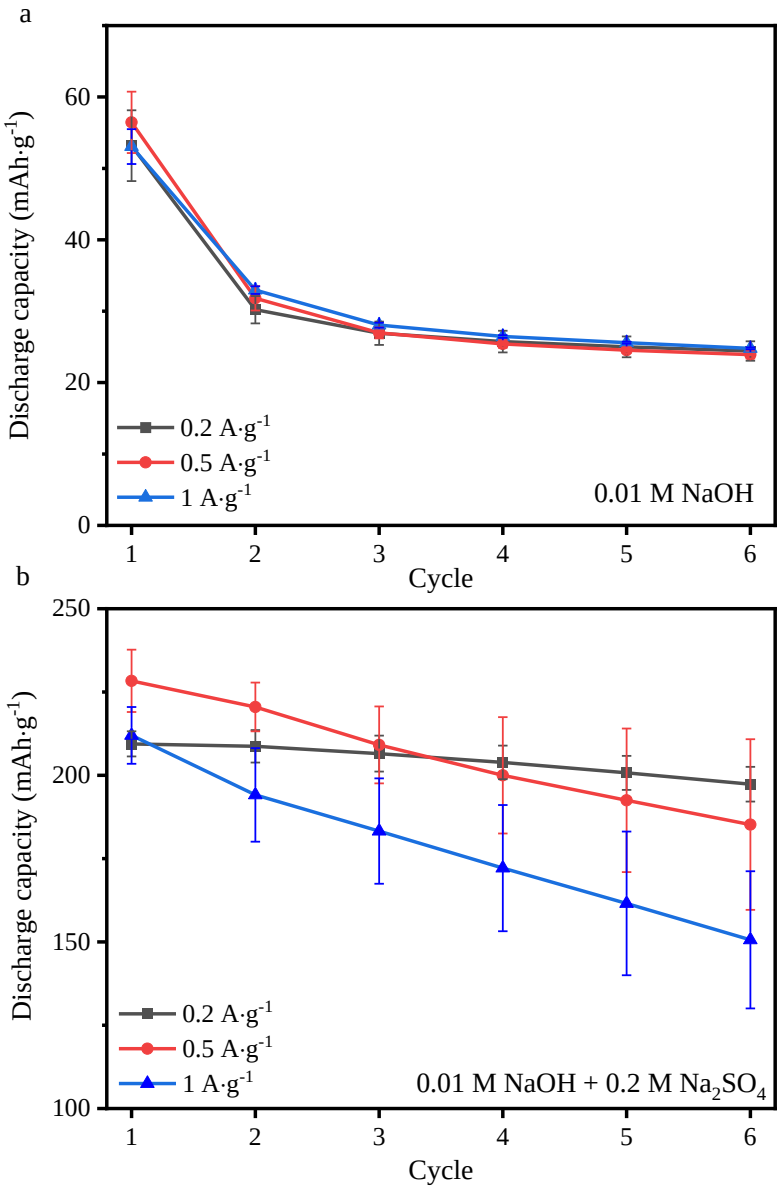

Figure 4.12 Cyclability of γ-FeOOH at a series of current densities in different electrolytes: **(a)** 0.01 M NaOH; **(b)** 0.01 M NaOH with 0.2 M Na_2SO_4.

Figure 4.12 shows the capacity retention of FeOOH in both electrolytes (average of four runs) at the current density ranging from 0.2 $A \cdot g^{-1}$ to 1 $A \cdot g^{-1}$. There was no noticeable difference in capacity retention when 0.01 M NaOH was used, where a large capacity drop occurred under all three current densities. In the cocktail electrolyte, the capacity retention was significantly improved. At a discharge rate of 0.2 $A \cdot g^{-1}$, the first discharge segment had an averaged value of 209.4 $mAh \cdot g^{-1}$, and the sixth discharge cycle had an averaged value of 197.3 $mAh \cdot g^{-1}$, a 94.2% capacity retention. When the discharge rate increased to 0.5 $A \cdot g^{-1}$ and 1 $A \cdot g^{-1}$, the capacity retention after 6 cycles dropped to 81.1% and 77.6%, respectively.

4.1.3 CP MEASUREMENTS OF LEPIDOCROCITE WITH A POTENTIAL WINDOW FROM -1.1 V TO 0.2 V

As discussed previously, the capacity in 0.01 M NaOH measured with a potential window from -1.05 V to -0.35 V was much lower than in the cocktail electrolyte. One possible reason for that was that the reduction was uncompleted in the potential window. Therefore, CP measurements with a wide potential window from -1.1 V to 0.2 V were conducted using the same current density of 0.2 $A \cdot g^{-1}$. As shown in **Figure 4.13**, both charge and discharge capacity were significantly increased when a wider potential window (-1.1 V to 0.2 V) was used, increasing from 46.6 $mAh \cdot g^{-1}$ and 30.7 $mAh \cdot g^{-1}$ to 152.0 $mAh \cdot g^{-1}$ and 118.5 $mAh \cdot g^{-1}$, respectively. The dC/dV curve showed that the reduction was close to complete when the potential limit was decreased from -1.05 V to -1.1 V, and the oxidization feature around -0.6 V was significantly enhanced accordingly. Thus, the results suggested that the low capacity from previous measurements was likely due to incomplete reduction.

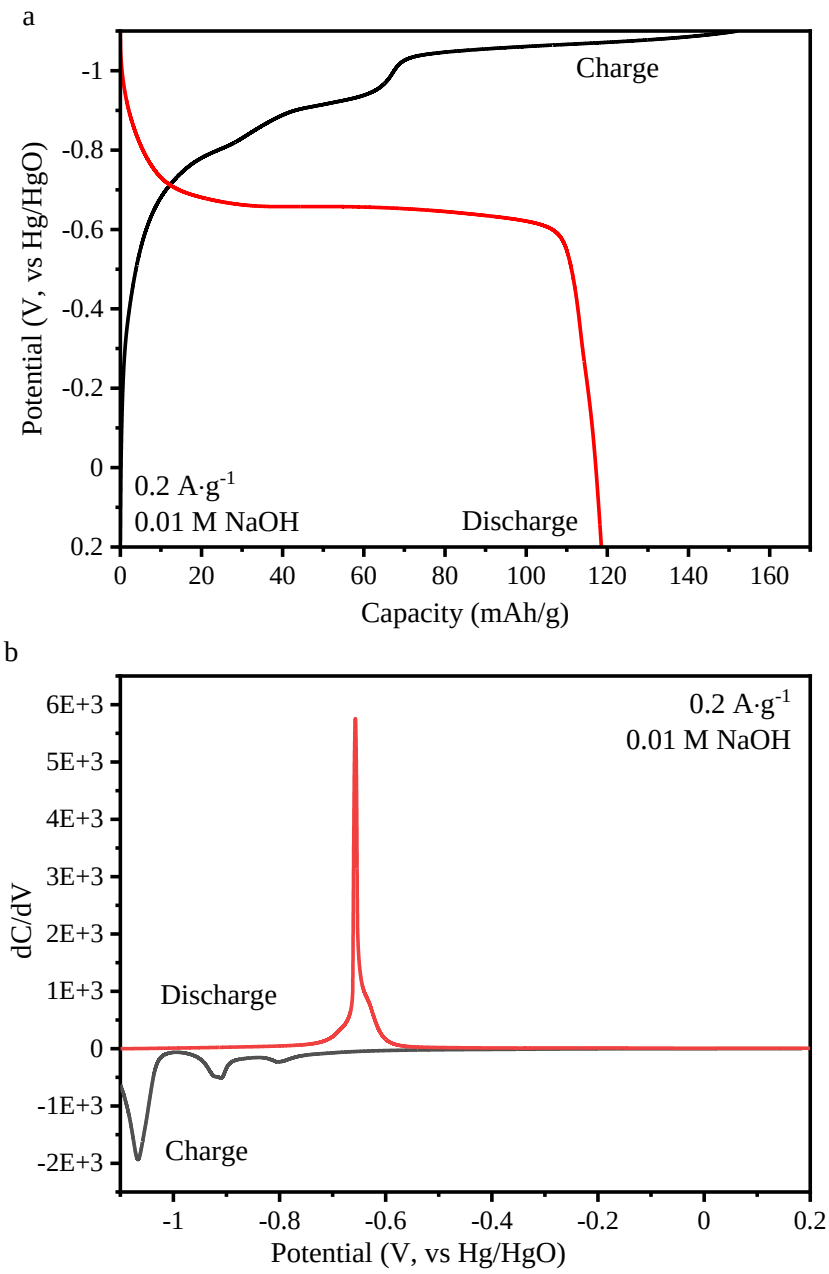

Figure 4.13 (a) 2nd cycle of CP measurement of γ-FeOOH and **(b)** the corresponding dC/dV curve in 0.01 M NaOH with a larger potential window at 0.2 $A \cdot g^{-1}$.

Figure 4.14 showed the charge/discharge profiles of the first seven CP cycles and the corresponding coulombic efficiencies at a current density of 0.2 $A \cdot g^{-1}$ when the 0.01 M NaOH electrolytes and wide potential window were used. The capacity decayed from 137.6 $mAh \cdot g^{-1}$ at

the 1st cycle to 77.9 mAh·g^{-1} at the 7th cycle, a 43.4% loss after 7 cycles, and the coulombic efficiency remained around 80% after the first cycle. The capacity retention and initial capacity were improved significantly comparing the results measured previously with a smaller potential window with pure NaOH electrolyte.

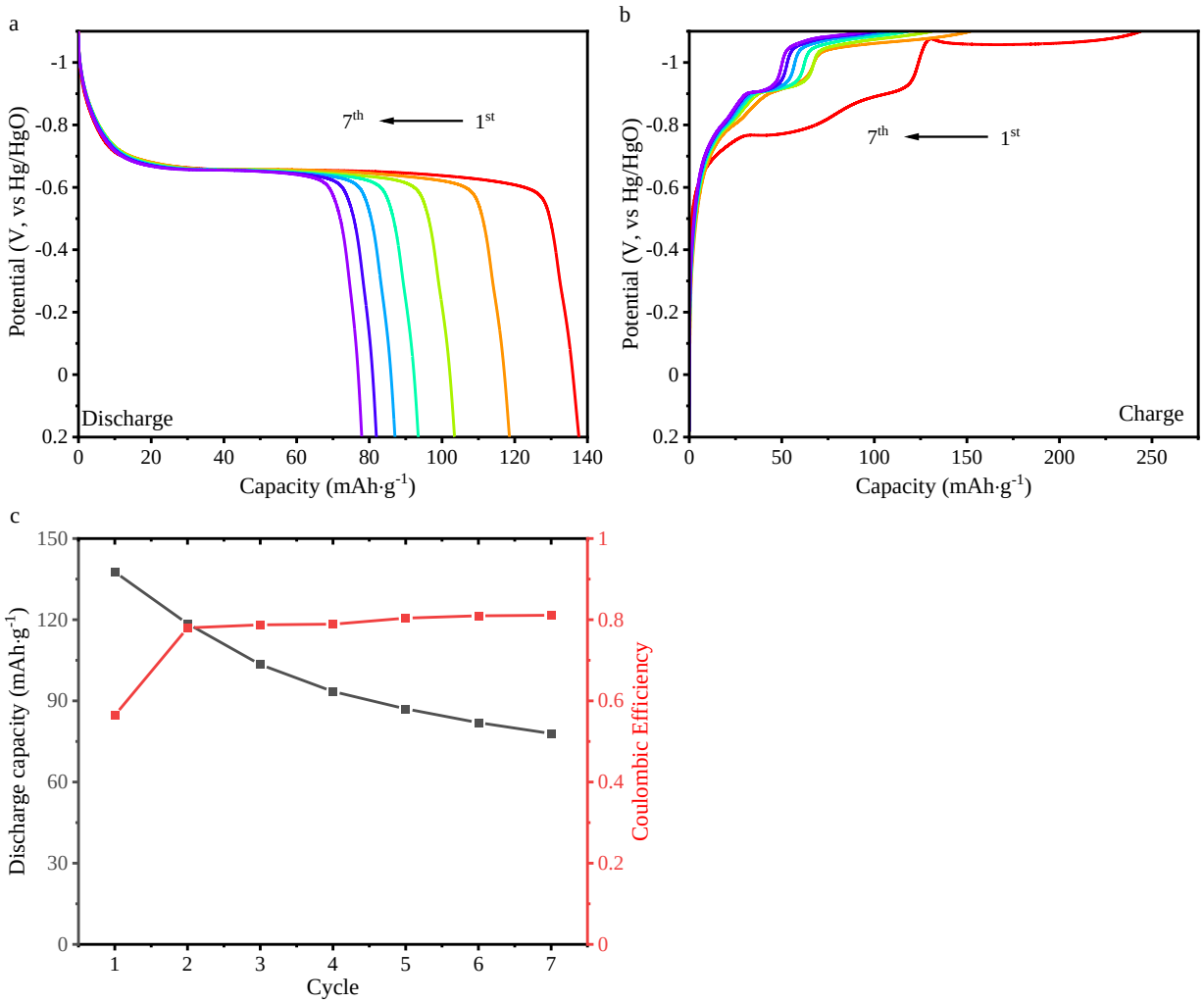

Figure 4.14 CP results of γ-FeOOH in 0.01 M NaOH at 0.2 A·g^{-1} with a larger potential window: **(a)** The first 7 discharge segments; **(b)** the first 7 charge segments; **(c)** the coulombic efficiencies of the first 7 cycles.

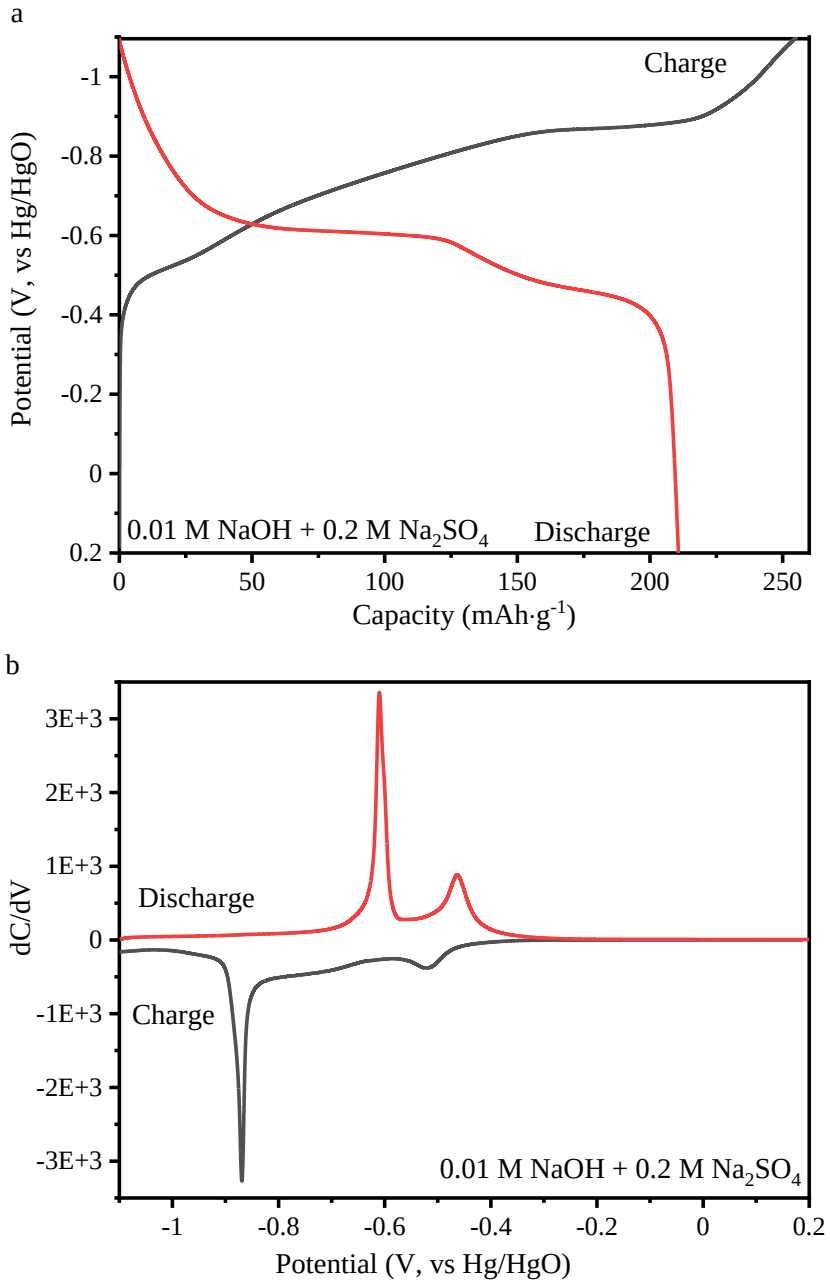

Figure 4.15 (a) 2nd cycle of CP measurement of γ-FeOOH and **(b)** the corresponding dC/dV curve in 0.01 M NaOH with 0.2 M Na_2SO_4 with a larger potential window at 0.2 $A \cdot g^{-1}$.

Figure 4.15 shows the CP measurement conducted in cocktail electrolytes with a wide potential window. Expanding potential window did not significantly affect the charge/discharge performance compared with the previously discussed CP measurements with a smaller potential

window, as the redox reactions were completed within the potential window of -1.05 V to -0.35 V.

The discharge capacity at the 2nd cycle was increased from 118.5 $mAh \cdot g^{-1}$ in pure NaOH electrolyte to 210.7 $mAh \cdot g^{-1}$ in the cocktail electrolyte. As shown in **Figure 4.15**, the discharge capacity in the cocktail electrolyte contributed from the first discharge stage in the 2nd cycle around -0.6 V was about 135 $mAh \cdot g^{-1}$, which was close to the overall capacity from pure NaOH electrolyte. The capacity difference was mainly contributed from the new plateau around -0.46 V.

The charge/discharge profiles of seven CP cycles and the corresponding coulombic efficiencies in the cocktail electrolyte are shown in **Figure 4.16**. The discharge capacity decreased from 215 $mAh \cdot g^{-1}$ at the 1st cycle to 201 $mAh \cdot g^{-1}$ at the 7th cycle, showing a 93.5% capacity retention after seven cycles. While in pure NaOH electrolyte, the discharge capacity decreased from 138 $mAh \cdot g^{-1}$ at the 1st cycle to 78 $mAh \cdot g^{-1}$ at the 7th cycle, showing a 56.6% capacity retention after seven cycles. Compared with the rapid capacity loss in pure NaOH electrolytes, the addition of Na_2SO_4 increased the overall capacity and improved capacity retention.

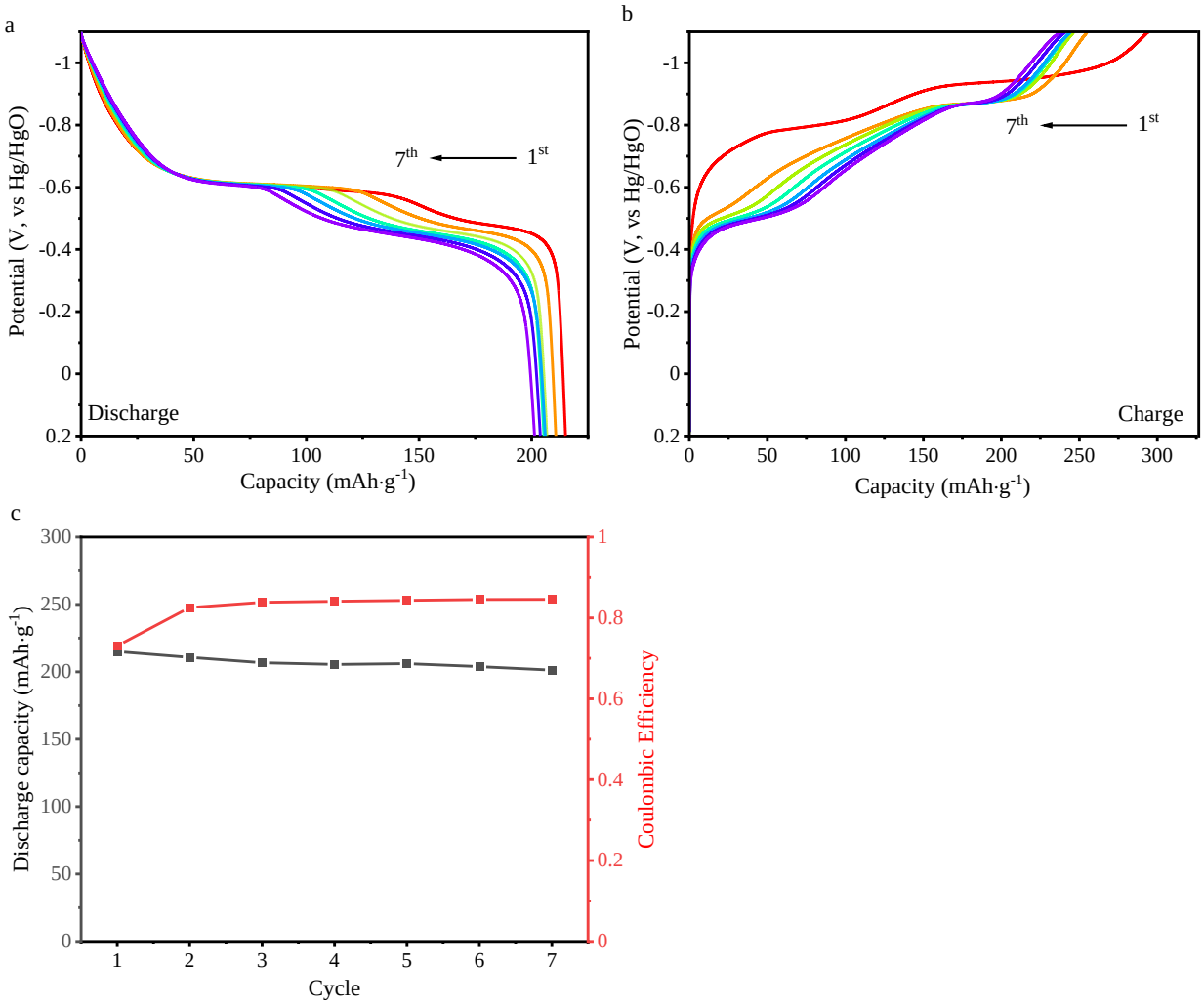

Figure 4.16 CP results of γ-FeOOH in 0.01 M NaOH with 0.2 M Na_2SO_4 at 0.2 $A \cdot g^{-1}$ with a larger potential window: **(a)** The first 7 discharge segments; **(b)** the first 7 charge segments; **(c)** the coulombic efficiencies of the first 7 cycles.

A closer look at the discharge profile showed that in the cocktail electrolyte, the capacity from the first plateau (below -0.55 V) decreased from 148 $mAh \cdot g^{-1}$ for the first cycle to 93 $mAh \cdot g^{-1}$ for the seventh cycle, as shown in **Figure 4.17**.

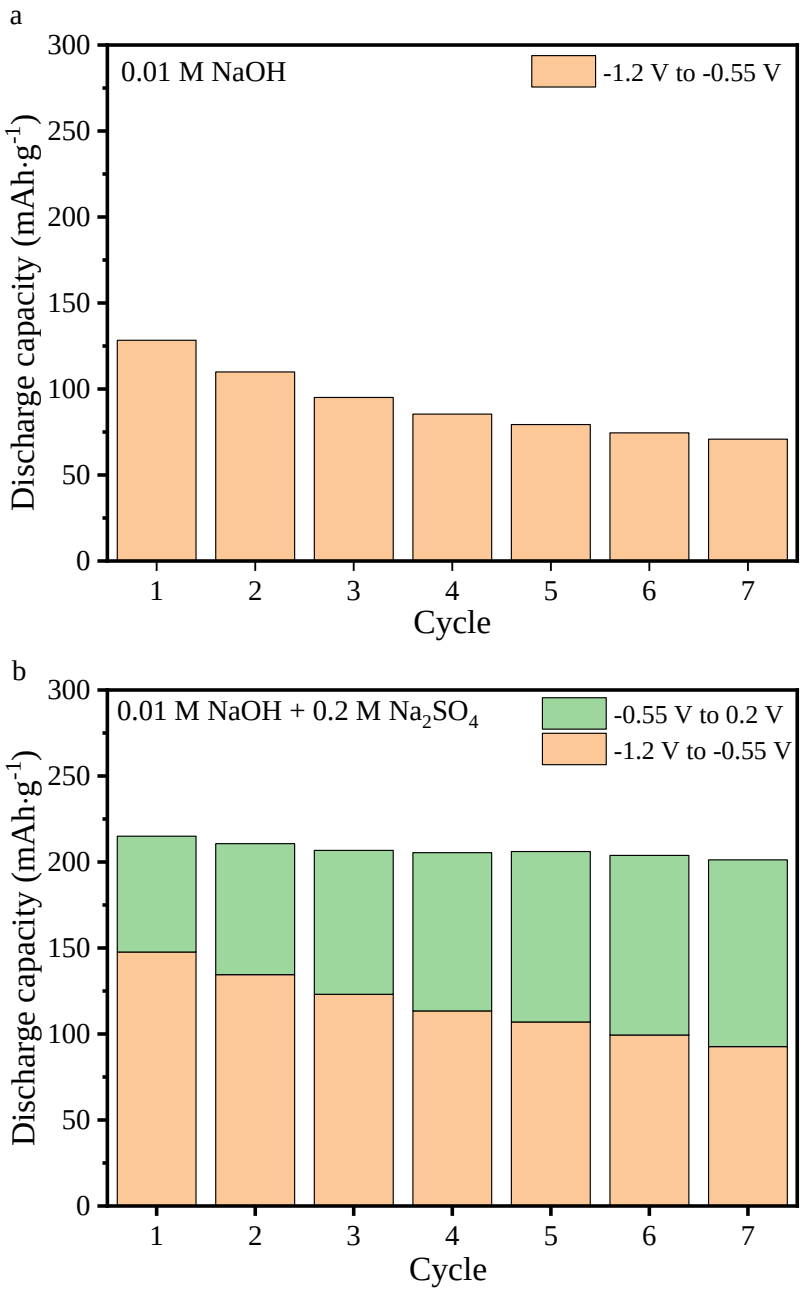

Figure 4.17 The distribution of discharge capacity of γ-FeOOH at 0.2 $A \cdot g^{-1}$ in different electrolytes: **(a)** 0.01 M NaOH; **(b)** 0.01 M NaOH with 0.2 M Na_2SO_4.

While the capacity contributed from the second plateau (above -0.55 V) increased from 67 $mAh \cdot g^{-1}$ for the 1st cycle to 109 $mAh \cdot g^{-1}$ for the 7th cycle, a plateau in a charge/discharge profile or a redox peak in a CV curve represents a transport-limited process. Plateaus or peaks at

different potentials in the same profile are usually from different electrochemical reactions. The capacity decrease in the first plateau and increase in the second plateau suggested that the first reaction was less favored, and the second reaction was gradually more favored over cycling. As discussed previously, the formation of GR in the oxidization process was a kinetically slow process, and low current density favored this reaction. Therefore, we hypothesize that the electrode particles might break down to smaller sizes during the cycling, improving mass transfer and the formation of GR.

The contributions from the background in half-cell CP tests were also measured, and the results are shown in **Figure 4.18**. Both the charge and discharge segments showed negligible capacities. Especially the discharge capacities were both below 5 $mAh \cdot g^{-1}$ and showed no plateau. Thus, the contribution from the background was neglected and not included in the capacity calculations for half-cell measurements.

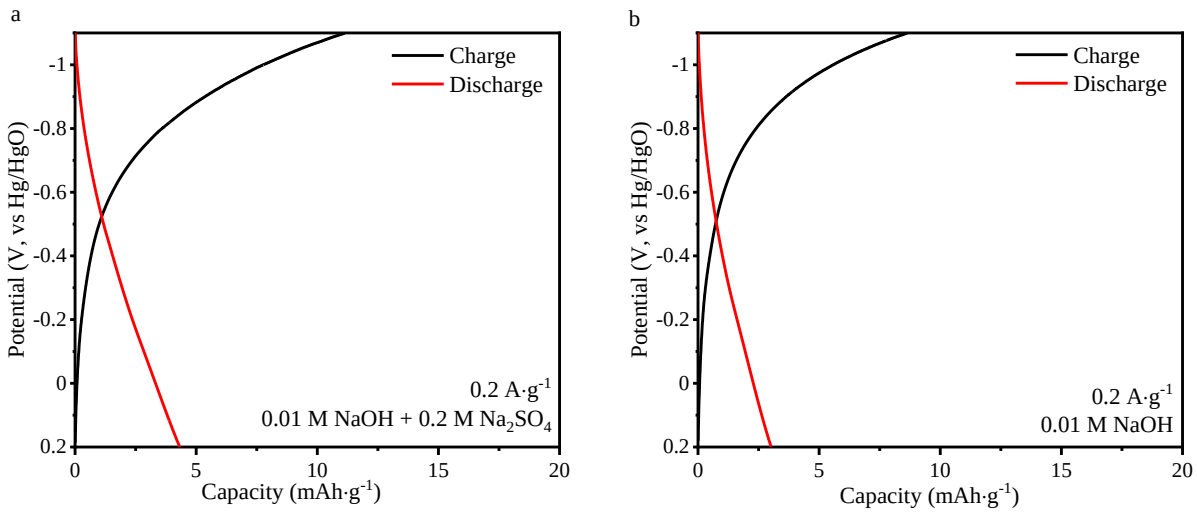

Figure 4.18 Contribution from the background in half-cell CP measurements with different electrolytes: **(a)** 0.01 M NaOH with 0.2 M Na_2SO_4; **(b)** 0.01 M NaOH.

Half-cell CP measurements helped understand the reaction kinetics and the short-term cyclability of the electrode materials. However, full-cell measurement was favored for the long-term

performance, as it is a closed system where contact with air is minimized. It also ensures better contact between activate material and the current collector.

4.2 FULL CELL MEASUREMENTS

Two-electrode full-cell measurement is the most frequently used electrochemical method to evaluate the long-term performance of battery devices. Unlike the three-electrode half-cell tests, full-cell measurements use two electrodes (the cathode and the anode) without employing a reference electrode. Therefore, during the two-electrode test, the absolute potential of electrode reaction often cannot be controlled without a reference electrode. Instead, only the potential difference between the two electrodes could be measured and controlled. In this research, the potential range was set from 0.1 V to 1.5 V, corresponding to a 1.4 V potential window, the same potential difference as in half-cell measurements. Full cells usually go through a complicated activation process that lasts more than one cycle.[140-142] The activation process for each full-cell measurement was excluded from the data shown in this chapter.

4.2.1 BALANCING OF THE CAPACITY OF ELECTRODES

In full-cell measurements, it is critical to have the two electrodes with balanced capacities, or a smaller capacity on the electrode of interest so performance the full cell could be dominated by that electrode. The cathode material used in the full-cells was carbon black (XC-72). XC-72 was chosen for its relatively large specific surface area, which could lead to a reasonable capacity. The discharge capacity of XC-72 was measured in full-cell with the two different electrolytes, and the results are shown in **Figure 4.19**. It showed an average discharge capacity of 8.0 $mAh \cdot g^{-1}$ in cocktail electrolyte and 6.3 $mAh \cdot g^{-1}$ in pure NaOH electrolyte. Considering the FeOOH active materials had a much higher storage capacity (> 100 $mAh \cdot g^{-1}$) than XC-72, the mass loading of

anode and cathode were set at different values to have larger capacity from the cathode. In this research, the loading of the anode contained ~ 0.4 mg of γ-FeOOH. So, the highest capacity the cathode could provide was $0.4\ mg \times 215\ mAh \cdot g^{-1} = 0.086\ mAh$ in the cocktail electrolyte, and $0.4\ mg \times 138\ mAh \cdot g^{-1} = 0.055\ mAh$ in pure NaOH electrolyte. While the loading on the cathode contained ~ 20 mg of XC-72. Thus, the capacity it can provide was $20\ mg \times 8.0\ mAh \cdot g^{-1} = 0.16\ mAh$ in the cocktail electrolyte, and $20\ mg \times 6.3\ mAh \cdot g^{-1} = 0.126\ mAh$ in pure NaOH electrolyte. The above calculations show that the anode in both electrolytes had around 50% of the theoretical capacity of the cathode. It was clear that a higher mass loading is needed in the cathode to exceed the anode in capacity.

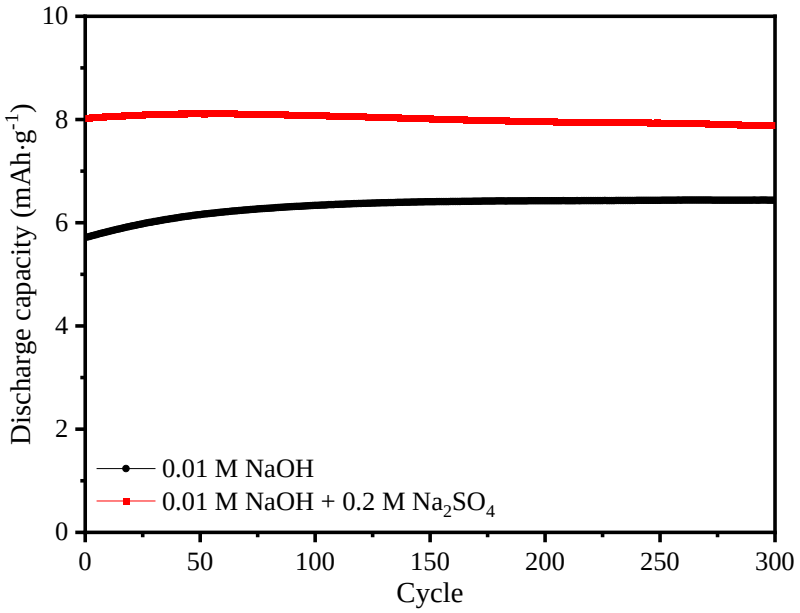

Figure 4.19 The discharge capacity of XC-72 measured in full-cell with different electrolytes.

One of the benefits of choosing XC-72 as the cathode is that the charge storage mechanism with XC-72 was majorly double-layer capacitance, which was a fast process and would unlikely be the limiting step of the full-cell reactions. As shown in **Figure 4.20**, there was no plateau in either CP profile from both electrolytes. As the capacity majorly contributed from surface

double-layer capacitance which was a highly reversible process, the capacity of XC-72 was fairly stable over cycling, as shown in **Figure 4.19**.

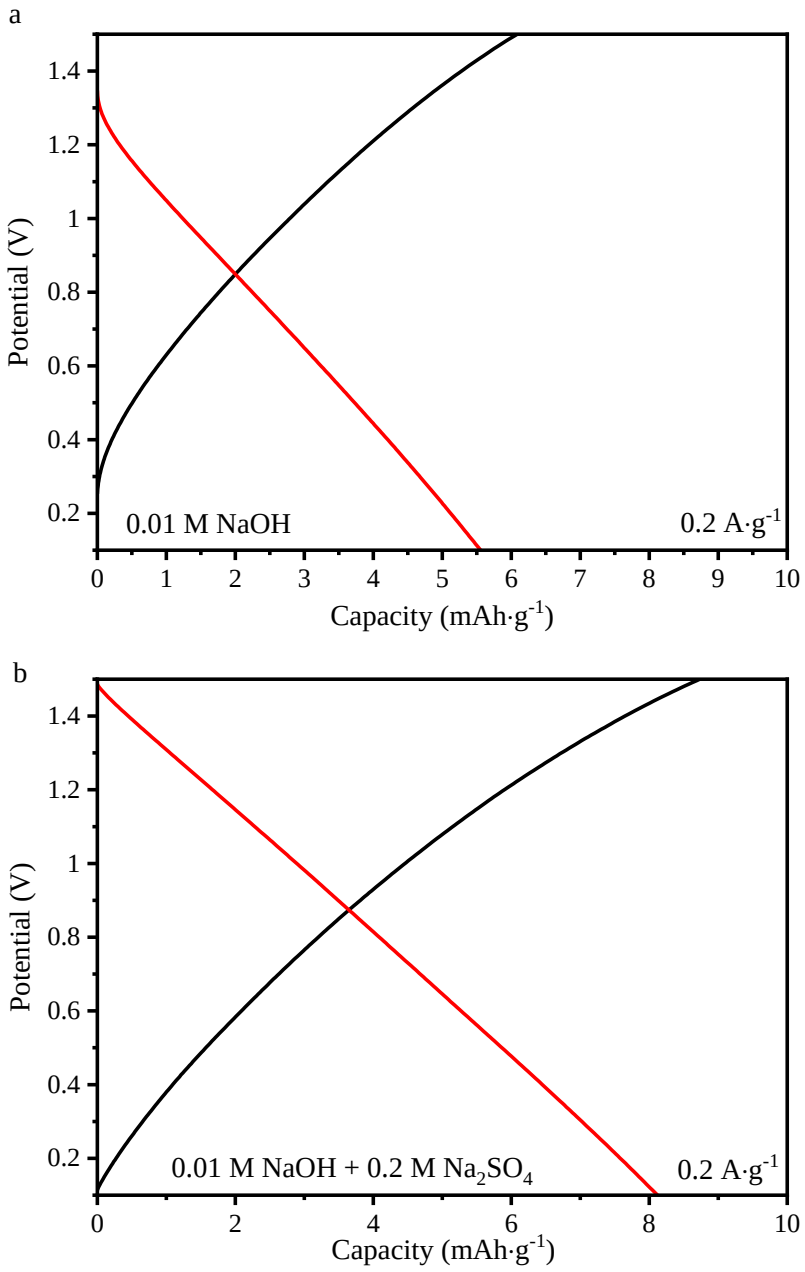

Figure 4.20 CP results of the 1st cycle of XC-72 measured in full-cell with different electrolytes: **(a)** 0.01 M NaOH; **(b)** 0.01 M NaOH with 0.2 M Na_2SO_4.

4.2.2 LONG-TERM CYCLABILITY OF LEPIDOCROCITE IN FULL CELLS

High discharge capacity and good cyclability are two important features that a good battery should have. The assembled full-cells were measured over 300 cycles at a current density of 0.2 $A \cdot g^{-1}$, and results were shown in **Figure 4.21**. The current density was calculated based on the mass loading of the active material (γ-FeOOH). Although the carbon black consisted 80% of the mass, its capacity was minimal compared with γ-FeOOH.

The discharge capacity of γ-FeOOH anode (based on the mass loading of the γ-FeOOH) in the cocktail electrolyte had an initial value of 67.8 $mAh \cdot g^{-1}$ and was maintained at 62.9 $mAh \cdot g^{-1}$ after 300 cycles, showing capacity retention of 92.8%. While the discharge capacity of γ-FeOOH anode in the pure NaOH electrolyte showed a much lower initial capacity of 41.2 $mAh \cdot g^{-1}$ and dropped down to 19.5 $mAh \cdot g^{-1}$ after 300 cycles, showing capacity retention of 47.3% over 300 cycles. Similar to the results from half-cell CP measurements, the addition of Na_2SO_4 increased the initial capacity by about 64.6% and significantly improved the capacity retention.

Another important feature was coulombic efficiency. A higher coulombic efficiency means higher energy efficiency and usually indicates more reversible battery reactions. Adding Na_2SO_4 also significantly improved the coulombic efficiency of the full-cells, as shown in **Figure 4.21**. The full-cell measured in cocktail electrolyte showed a coulombic efficiency of 92.6% at the initial cycle and 94.2% for the 300^{th} cycle, averaged at 93.3%. In the meantime, the full-cells measured with pure NaOH electrolyte showed an initial coulombic efficiency of 66.7% and increased to 90.6% at the 300^{th} cycle, averaged at 84.5%.

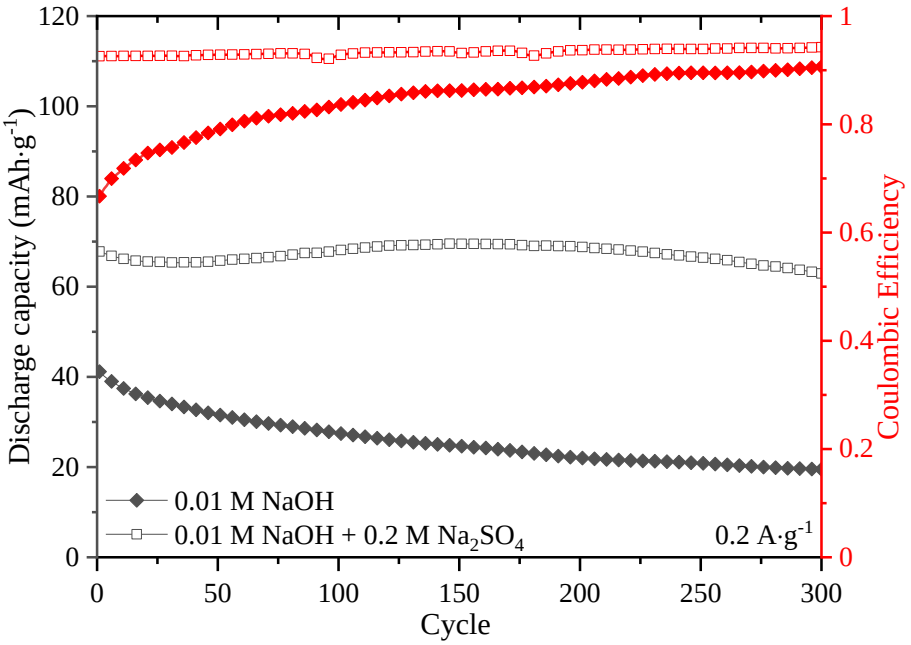

Figure 4.21 Discharge capacity of the γ-FeOOH anode and the coulombic efficiency of the full-cells with two different electrolytes.

Figure 4.22 shows the CP profiles of the initial cycle and the 300th cycle. In the full-cell with cocktail electrolyte, the initial cycle had a more significant charge/discharge plateaus than the 300th cycle. One of the reasons could be the capacity loss over cycling, resulting in a smaller overall capacity. Another reason could be the potential shifting of the electrochemical reactions that occurred in both electrodes. As shown in the dC/dV curve in **Figure 4.22 (a)**, there was a major redox peak couple at 0.7 V(discharge)/1.0 V (charge) in the initial cycle, which shifted to 0.8 V(discharge) /1.1 V(charge) in the 300th cycle with much smaller intensity. There was also a minor redox couple at 0.4 V(discharge) /0.5 V(charge) in the initial cycle, which stayed roughly at the same potential in the 300th cycle but with a relatively more vigorous intensity.

In the full-cell test, the discharge of the cell represented the oxidization of the anode. The first strong oxidization peak at 0.7 V was followed by a relatively less intensive oxidization peak at

0.4 V, similar to CP profiles measured in half-cells. Unlike the potentials in three-electrode half -cells, the voltages in the full-cells only represented the potential difference between two electrodes and may not be identical to the potential observed in half-cell tests (the potentials of the oxidization peaks were -0.6 V and -0.46 V, vs. Hg/HgO in half cell CP measurement).

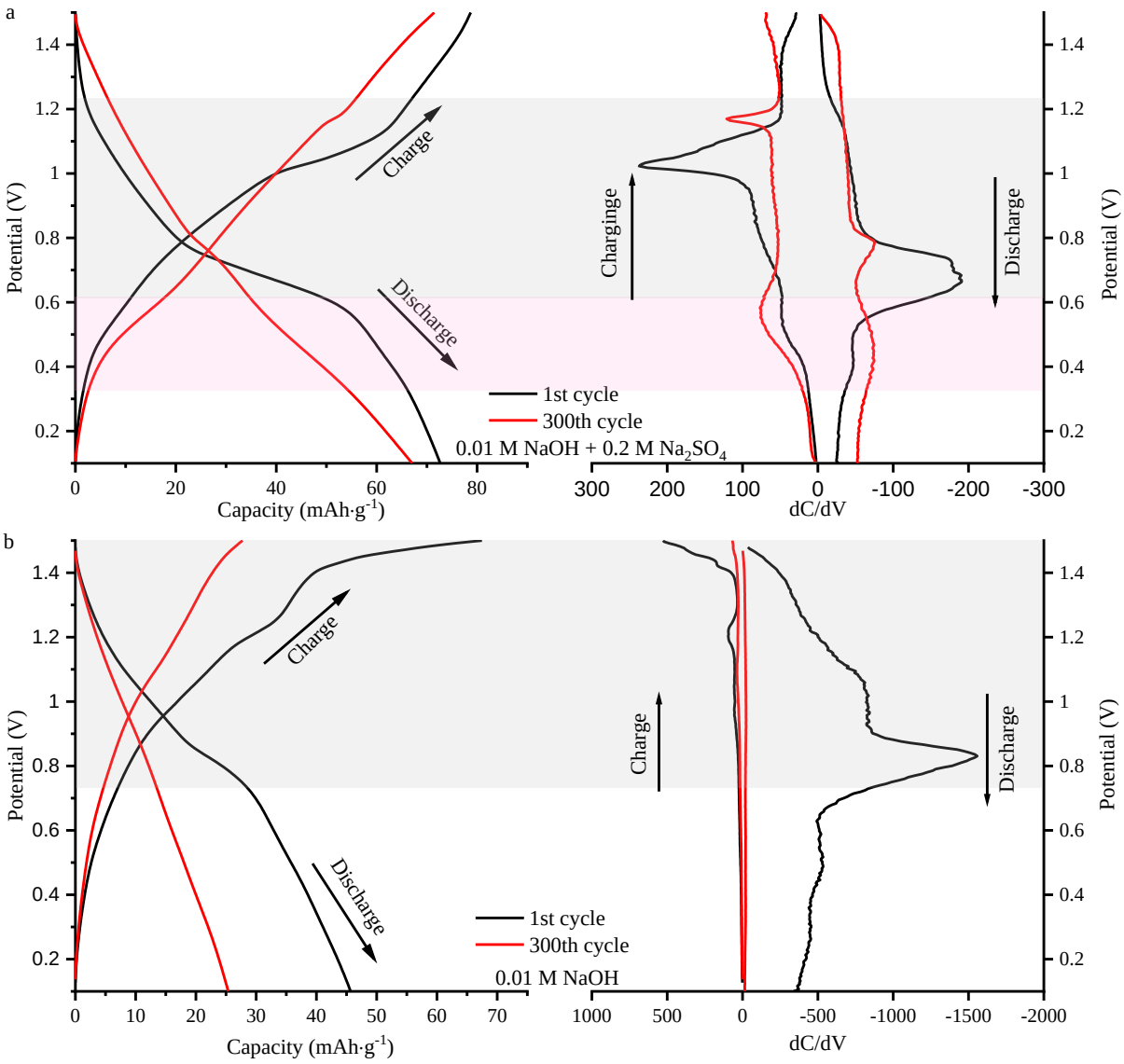

Figure 4.22 CP profiles of the full cells and the corresponding dC/dV curve with two different electrolytes: **(a)** 0.01 M NaOH with 0.2 M Na_2SO_4; **(b)** 0.01 M NaOH,

In the full-cell measured with pure NaOH electrolyte in **Figure 4.22 (b)**, there was only one major redox couple at 0.8 V (discharge) /1.4 V (charge) in the initial cycle and almost diminished after 300 cycles. The low coulombic efficiency in the initial cycles could possibly result from gas evolution at 1.4 V. At 1.4 V (the potential difference between anode and cathode), the anode was at reduced state (and HER could happen), while the cathode was at oxidized state (and OER could happen).

4.2.3 RATE CAPABILITY OF LEPIDOCROCITE IN FULL CELLS

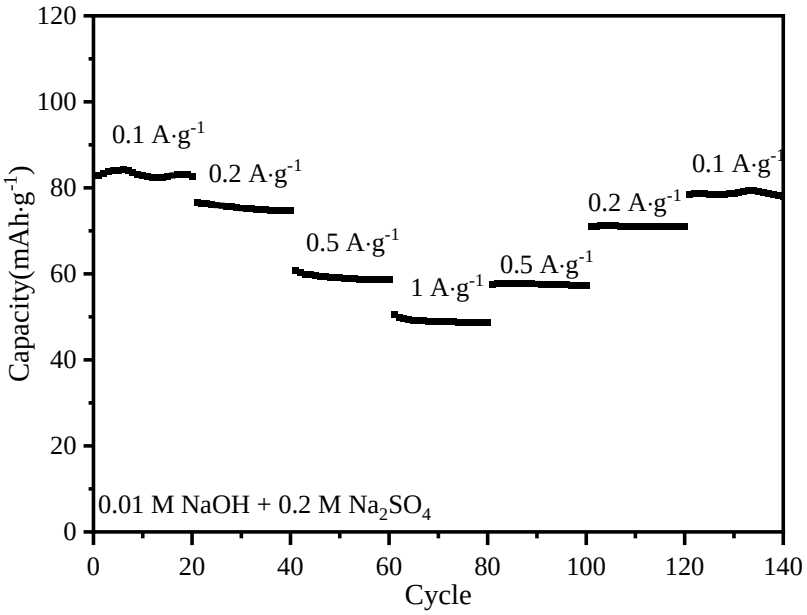

Figure 4.23 The discharge capacity of the γ-FeOOH anode in rate capability measurement in full-cells with the cocktail electrolytes consisting of 0.01 M NaOH and 0.2 M Na_2SO_4.

Another essential feature of a suitable battery device was excellent rate capability. A good battery should still be able to deliver good charge/discharge capacity even at high current densities. Since the γ-FeOOH measured with cocktail electrolyte showed much-improved capacity and better retention compared with full-cells measured with pure NaOH electrolyte, the

rate capability measurements of γ-FeOOH were conducted with the cocktail electrolyte only. The results were shown in **Figure 4.23**.

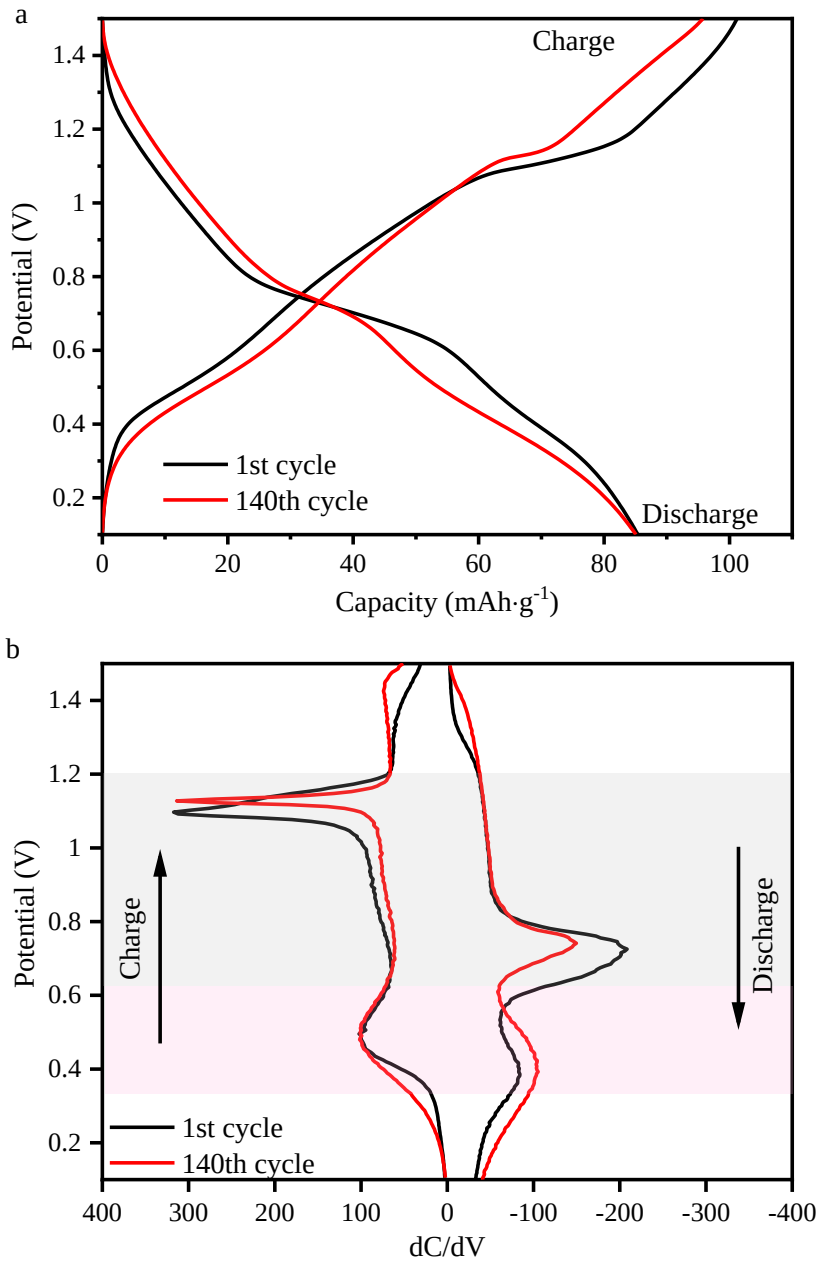

Figure 4.24 (a) CP profiles of first and last cycle from rate capability measurement of γ-FeOOH with the cocktail electrolyte consisting of 0.01 M NaOH and 0.2 M Na_2SO_4 and **(b)** the corresponding dC/dV curves.

The measurement was conducted with a series of current densities starting from 0.1 $A \cdot g^{-1}$ to 1 $A \cdot g^{-1}$ and then back to 0.1 $A \cdot g^{-1}$. A total of twenty charge and discharge cycles were measured under each step with a constant current density. The first twenty cycles showed an average capacity of 76.4 $mAh \cdot g^{-1}$ for the γ-FeOOH anode. When the current density increased to 1 $A \cdot g^{-1}$, the discharge capacity dropped to an average value of 42.3 $mAh \cdot g^{-1}$, maintaining 55.4% of the discharge capacity after the current density increased by one-fold. After the current density gradually decreased back to 0.1 $A \cdot g^{-1}$, an averaged discharge capacity of 71.9 $mAh \cdot g^{-1}$ was kept, about 6% of capacity loss compared with the starting stage of the measurement at the same current density. Thus, unlike in the half-cell CP measurements where lowering current density did not result in a capacity increase, discharge capacities for the γ-FeOOH anode in full-cells increased with decreasing current densities.

The CP profile of the first cycle and the 140^{th} cycle and their derivatives are shown in **Figure 4.24**. Compared to the first cycle data, the discharge capacity at the 140^{th} cycle was benefited greatly from the plateau around 0.4 V, though the overall capacity from the 1^{st} and the 140^{th} cycles stayed roughly the same. The dC/dV curve also showed the relative intensity of the peak at 0.4 V became larger compared with the peak at 0.7 V from the first cycle to the last cycle.

The contribution from the background of the full cells are measured, and the results are shown in **Figure 4.25**. The discharge capacity shown in **Figure 4.21** and **Figure 4.23** were all obtained after subtracting the contribution from the background. The background was majorly contributed from the carbon black used to improve the conductivity. The measurement of the background was done by excluding the active material and everything else was kept the same. The current density was calculated based on the 'imaginary' loading of active materials. For example, if in the full-cell measurement with 0.4 mg loading of γ-FeOOH and 1.6 mg of carbon black, the

absolute current would be set to 0.08 mA to set the current density as 0.2 $A \cdot g^{-1}$ based on the mass of γ-FeOOH, the measurement on the background would be conducted only with 1.6 mg loadings of carbon black but with the same absolute current. The result could thus be directly used as the contribution from the background. Following the observation from half-cell measurements, γ-FeOOH showed a higher initial discharge capacity and better capacity retention over 300 cycles in full-cell measurements when cocktail electrolyte was used than when pure NaOH was used as electrolyte. The full-cell measurements also showed that γ-FeOOH had a good rate capability in the cocktail electrolyte.

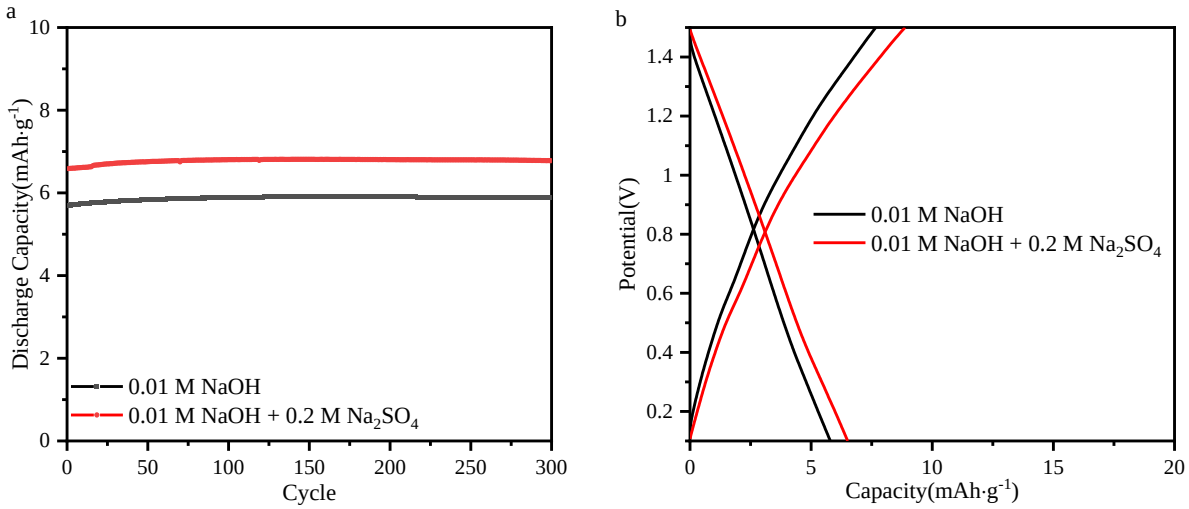

Figure 4.25 Background contributed from the carbon black with two different electrolytes: **(a)** the discharge capacity over 300 cycles; **(b)** the CP profiles of the 1st cycle.

4.3 ELECTROCHEMICAL PERFORMANCE OF LEPIDOCROCITE IN ALKALINE SYSTEM WITH DIFFERENT SALT

Our results showed that the improved electrochemical performance of γ-FeOOH in the cocktail electrolyte resulted from new GR formation in the oxidization process. As GR could form with different types of intercalated anions, it should be no surprise that the concept of adding

additional salt into the electrolyte to improve the electrochemical performance of γ-FeOOH was not limited to Na_2SO_4.

By replacing Na_2SO_4 with NaCl, a similar phenomenon was observed. Half-cell CP measurement of γ-FeOOH was done with a cocktail electrolyte of 0.01 M NaOH with 0.2 M NaCl, and the result was shown in **Figure 4.26** and **Figure 4.27**.

As shown in **Figure 4.26**, adding NaCl into NaOH electrolyte also incurred the new redox features at -0.46 V (discharging)/ -0.51 V (charging), roughly similar potentials in $NaOH/Na_2SO_4$ electrolytes. As a result, the overall capacity was 205.1 $mAh \cdot g^{-1}$, close to the value obtained from $NaOH/Na_2SO_4$ system (210.7 $mAh \cdot g^{-1}$). It also showed a similar change in the distribution of capacity, but with a slightly higher initial contribution at the 2nd cycle from the second discharge plateau: 45.6% of the total discharge capacity, compared with 36.2% with $NaOH/Na_2SO_4$ as electrolyte.

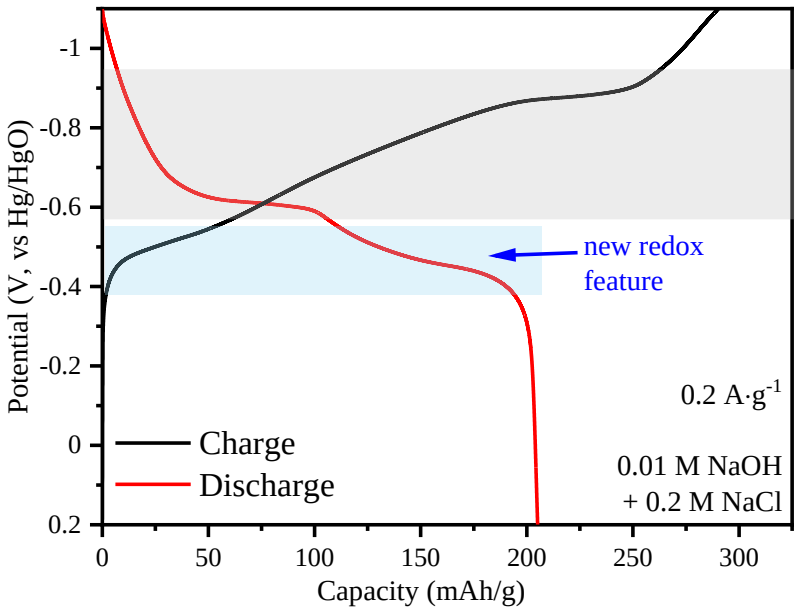

Figure 4.26 2nd cycle of charge/discharge profile of γ-FeOOH measured at 0.2 $A \cdot g^{-1}$ in 0.01 M NaOH with 0.2 M NaCl.

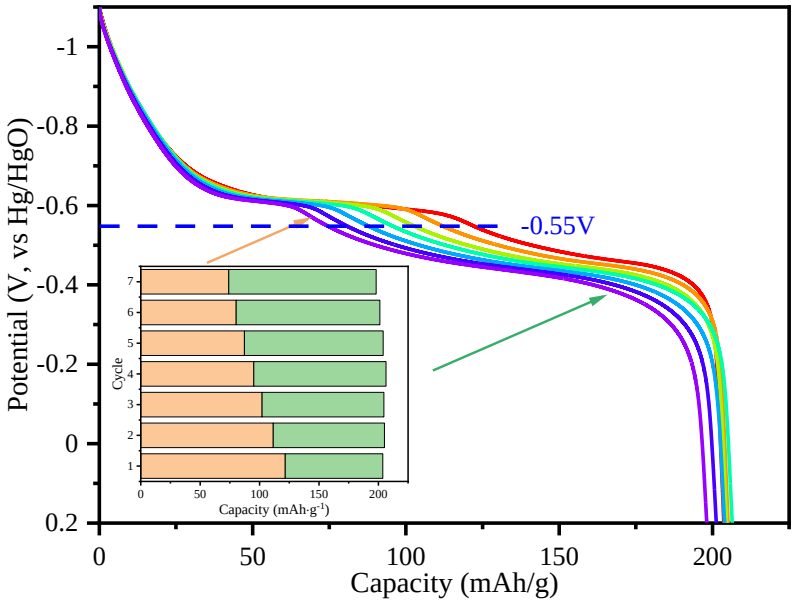

Figure 4.27 First 7 discharge curves of γ-FeOOH measured at 0.2 A·g^{-1} in 0.01 M NaOH with 0.2 M NaCl.

CHAPTER 5 CONCLUSIONS AND FUTURE WORK

5.1 CONCLUSIONS

This project focused on the application of iron-based materials in an aqueous system. The electrochemical performance of synthesized of γ-FeOOH in an alkaline environment was thoughtfully studied in a three-electrode half-cell system and asymmetric full-cell system. In addition, the phase transitions during the reactions were investigated with in-situ XRD measurements, and a reaction mechanism was proposed.

The results showed that γ-FeOOH as cathode materials could deliver a limited discharge capacity and poor capacity retention, possibly due to the formation of an electrochemically inert Fe_3O_4 phase. The cocktail electrolytes containing Na_2SO_4 and NaOH resulted in a higher initial discharge capacity and improved capacity retention. This was likely due to another reaction pathway that was made possible by the addition of Na_2SO_4. The intermediate species of green rust formed in the oxidization made it possible for the oxidization of $Fe(OH)_2$ to FeOOH through a reaction pathway of $Fe(OH)_2 \rightarrow GR \rightarrow FeOOH$, in addition to the less reversible reaction pathway of $Fe(OH)_2 \rightarrow Fe_3O_4$. $Fe(OH)_2 \rightarrow GR \rightarrow FeOOH$ pathway led to a higher charger transfer number and better discharge capacity. The results also showed that the green rust formation was favored in lower pH environments, which justified why mild alkaline electrolytes were used in this research.

5.2 FUTURE WORK

As discussed previously, the cocktail electrolyte was not limited to Na_2SO_4/NaOH. Salts that could provide anions to form green rust would likely serve as an excellent additive to pure NaOH

solution. More kinds of salts could be investigated to study the effect on the electrochemical performance of γ-FeOOH in future work.

As the starting material of γ-FeOOH did not exist in the following cycles, it was also possible that more iron-based materials could be used in this system. As this study showed that the reduction product was $Fe(OH)_2$, ion-based materials that could be reduced to $Fe(OH)_2$ were worthwhile to study under this system in future work.

The results showed that the formation of green rust was favored in lower pH environments. Therefore, it was meaningful to investigate the performance of iron-based materials under the pH range below 12, where more green rust could form and lead to a higher capacity.

LIST OF REFERENCES

[1] Wall, Staffan. "The history of electrokinetic phenomena." *Current Opinion in Colloid & Interface Science* 15.3 (2010): 119-124.
[2] Beck, Fritz, and Paul Rüetschi. "Rechargeable batteries with aqueous electrolytes." *Electrochimica Acta* 45.15-16 (2000): 2467-2482.
[3] Halpert, Gerald. "Past developments and the future of nickel electrode cell technology." *Journal of power sources* 12.3 (1984): 177-192.
[4] Shukla, A. K., M. K. Ravikumar, and T. S. Balasubramanian. "Nickel/iron batteries." *Journal of power sources* 51.1-2 (1994): 29-36.
[5] Manthiram, Arumugam. "An outlook on lithium ion battery technology." *ACS central science* 3.10 (2017): 1063-1069.
[6] Zubi, Ghassan, et al. "The lithium-ion battery: State of the art and future perspectives." *Renewable and Sustainable Energy Reviews* 89 (2018): 292-308.
[7] Wakihara, Masataka. "Recent developments in lithium ion batteries." *Materials Science and Engineering: R: Reports* 33.4 (2001): 109-134.
[8] Blomgren, George E. "The development and future of lithium ion batteries." *Journal of The Electrochemical Society* 164.1 (2016): A5019.
[9] Amrouche, S. Ould, et al. "Overview of energy storage in renewable energy systems." *International journal of hydrogen energy* 41.45 (2016): 20914-20927.
[10] Nasiri, Adel. "Integrating energy storage with renewable energy systems." 2008 *34th Annual Conference of IEEE Industrial Electronics*. *IEEE*, 2008.
[11] Barton, John P., and David G. Infield. "Energy storage and its use with intermittent renewable energy." *IEEE transactions on energy conversion* 19.2 (2004): 441-448.
[12] Suberu, Mohammed Yekini, Mohd Wazir Mustafa, and Nouruddeen Bashir. "Energy storage systems for renewable energy power sector integration and mitigation of intermittency." *Renewable and Sustainable Energy Reviews* 35 (2014): 499-514.
[13] Van der Linden, Septimus. "Bulk energy storage potential in the USA, current developments and future prospects." *Energy* 31.15 (2006): 3446-3457.
[14] Chen, Haisheng, et al. "Progress in electrical energy storage system: A critical review." *Progress in natural science* 19.3 (2009): 291-312.
[15] U.S. Energy Information Administration. *Monthly Energy Review*, July 2021.
[16] Cho, Jaephil, Sookyung Jeong, and Youngsik Kim. "Commercial and research battery technologies for electrical energy storage applications." *Progress in Energy and Combustion Science* 48 (2015): 84-101.
[17] Boebinger, Matthew G., et al. "Understanding transformations in battery materials using in situ and operando experiments: progress and outlook." *ACS Energy Letters* 5 (2020): 335-345.
[18] Palacin, M. Rosa. "Recent advances in rechargeable battery materials: a chemist's perspective." *Chemical Society Reviews* 38.9 (2009): 2565-2575.
[19] Bhatt, Mahesh Datt, and Colm O'Dwyer. "Recent progress in theoretical and computational investigations of Li-ion battery materials and electrolytes." *Physical Chemistry Chemical Physics* 17.7 (2015): 4799-4844.
[20] Daniell, John Frederic. "X. On Voltaic Combinations. In a letter addressed to Michael Faraday, DCL, FRS, Fullerian Prof. Chem. Royal Institution, Corr. Memb. Royal & Imp. Acadd. of Science, Paris, Petersburgh, &c. By J. Frederic Daniell, FRS, Prof. Chem. in King's College, London." *Philosophical Transactions of the Royal Society of London* 126 (1836): 107-124.

[21] Ma, Hua, et al. "α-CuV_2O_6 nanowires: Hydrothermal synthesis and primary lithium battery application." *Journal of the American Chemical Society* 130.15 (2008): 5361-5367.
[22] Dickinson, Edmund JF, and Andrew J. Wain. "The Butler-Volmer equation in electrochemical theory: Origins, value, and practical application." *Journal of Electroanalytical Chemistry* 872 (2020): 114145.
[23] Zhang, Dong, Branko N. Popov, and Ralph E. White. "Modeling lithium intercalation of a single spinel particle under potentiodynamic control." *Journal of the Electrochemical Society* 147.3 (2000): 831.
[24] Janek, Jürgen, and Wolfgang G. Zeier. "A solid future for battery development." *Nature Energy* 1, 16141 (2016).
[25] Tarascon, J-M., and Michel Armand. "Issues and challenges facing rechargeable lithium batteries." *Nature* 414 (2001): 359-367.
[26] Bachman, John Christopher, et al. "Inorganic solid-state electrolytes for lithium batteries: mechanisms and properties governing ion conduction." *Chemical Reviews* 116.1 (2016): 140-162.
[27] Huang, Jianhang, et al. "Recent progress of rechargeable batteries using mild aqueous electrolytes." *Small Methods* 3.1 (2019): 1800272.
[28] Guo, Fenghua, Nivedita Gupta, and Xiaowei Teng. "Enhancing pseudocapacitive process for energy storage devices: analyzing the charge transport using electro-kinetic study and numerical modeling." *Supercapacitors: Theoretical and Practical Solutions* 87 (2018).
[29] Wu, Y. P., E. Rahm, and R. Holze. "Carbon anode materials for lithium ion batteries." *Journal of Power Sources* 114.2 (2003): 228-236.
[30] Guo, Yanpeng, et al. "Layer structured materials for advanced energy storage and conversion." *Small* 13.45 (2017): 1701649.
[31] Zhang, Yufei, et al. "Interlayer Chemistry of Layered Electrode Materials in Energy Storage Devices." *Advanced Functional Materials* 31.4 (2021): 2007358.
[32] Yuan, Li-Xia, et al. "Development and challenges of $LiFePO_4$ cathode material for lithium-ion batteries." *Energy & Environmental Science* 4.2 (2011): 269-284.
[33] Nightingale Jr, E. R. "Phenomenological theory of ion solvation. Effective radii of hydrated ions." *The Journal of Physical Chemistry* 63.9 (1959): 1381-1387.
[34] Heyrovska, R. "Effective radii of alkali halide ions in aqueous solutions, crystals and in the gas phase and the interpretation of stokes radii." *Chemical Physics Letters* 163.2-3 (1989): 207-211.
[35] Wu, Xianyong, Daniel P. Leonard, and Xiulei Ji. "Emerging non-aqueous potassium-ion batteries: challenges and opportunities." *Chemistry of Materials* 29.12 (2017): 5031-5042.
[36] Chayambuka, Kudakwashe, et al. "Sodium‐ion battery materials and electrochemical properties reviewed." *Advanced Energy Materials* 8.16 (2018): 1800079.
[37] Slater, Michael D., et al. "Sodium‐ion batteries." *Advanced Functional Materials* 23.8 (2013): 947-958.
[38] Wang, X. P., Z. J. Cheng, and Q. F. Fang. "Influence of potassium doping on the oxygen-ion diffusion and ionic conduction in the $La_2Mo_2O_9$ oxide-ion conductors." *Solid State Ionics* 176.7-8 (2005): 761-765.
[39]] Kiriukhin, Michael Y., and Kim D. Collins. "Dynamic hydration numbers for biologically important ions." *Biophysical chemistry* 99.2 (2002): 155-168.
[40] Aricò, A., Bruce, P., Scrosati, B. et al. "Nanostructured materials for advanced energy conversion and storage devices." *Nature Materials* 4 (2005): 366–377.

[41] Bruce, Peter G., Bruno Scrosati, and Jean‐Marie Tarascon. "Nanomaterials for rechargeable lithium batteries." *Angewandte Chemie International Edition* 47.16 (2008): 2930-2946.
[42] Osada, Minoru, and Takayoshi Sasaki. "Exfoliated oxide nanosheets: new solution to nanoelectronics." *Journal of Materials Chemistry* 19.17 (2009): 2503-2511.
[43] Coleman, Jonathan N., et al. "Two-dimensional nanosheets produced by liquid exfoliation of layered materials." *Science* 331.6017 (2011): 568-571.
[44] Wang, Jiangyan, Yi Cui, and Dan Wang. "Design of hollow nanostructures for energy storage, conversion and production." *Advanced Materials* 31.38 (2019): 1801993.
[45]] Fleischmann, Simon, et al. "Pseudocapacitance: from fundamental understanding to high power energy storage materials." *Chemical Reviews* 120.14 (2020): 6738-6782.
[46] Jiang, Yuqi, and Jinping Liu. "Definitions of pseudocapacitive materials: a brief review." *Energy & Environmental Materials* 2.1 (2019): 30-37.
[47] Verma, Ram U. "Generalized relaxed proximal point algorithms involving relative maximal accretive models with applications in Banach spaces." *Communications of the korean mathematical society* 25.2 (2010): 313-325.
[48] Conway, Brian Evans, and Eliezer Gileadi. "Kinetic theory of pseudo-capacitance and electrode reactions at appreciable surface coverage." *Transactions of the Faraday Society* 58 (1962): 2493-2509.
[49] Wu, Zhong–Shuai, et al. "Graphene-based in-plane micro-supercapacitors with high power and energy densities." *Nature communications* 4, 2487 (2013).
[50] Goodenough, John B., and Youngsik Kim. "Challenges for rechargeable Li batteries." *Chemistry of materials* 22.3 (2010): 587-603.
[51] Pourbaix, Marcel. "Atlas of Electrochemical Equilibria in Aqueous Solutions." Houston, *NACE*, 1974
[52] Suo, Liumin, et al. "“Water-in-salt” electrolyte enables high-voltage aqueous lithium-ion chemistries." *Science* 350.6263 (2015): 938-943.
[53] Agrawal, R. C., and G. P. Pandey. "Solid polymer electrolytes: materials designing and all-solid-state battery applications: an overview." *Journal of Physics D: Applied Physics* 41.22 (2008): 223001.
[54] Ponrouch, A., et al. "Non-aqueous electrolytes for sodium-ion batteries." *Journal of Materials Chemistry A* 3.1 (2015): 22-42.
[55] Zhang, Huang, et al. "Challenges and Strategies for High‐Energy Aqueous Electrolyte Rechargeable Batteries." *Angewandte Chemie International Edition* 60.2 (2021): 598-616.
[56] Zheng, Jiaxin, et al. "Understanding thermodynamic and kinetic contributions in expanding the stability window of aqueous electrolytes." *Chem* 4.12 (2018): 2872-2882.
[57] Shan, Xiaoqiang, et al. "Bivalence Mn_5O_8 with hydroxylated interphase for high-voltage aqueous sodium-ion storage." *Nature communications* 7, 13370 (2016).
[58] Kalhoff, Julian, et al. "Safer electrolytes for lithium‐ion batteries: state of the art and perspectives." *ChemSusChem* 8.13 (2015): 2154-2175.
[59] Xu, Kang. "Nonaqueous liquid electrolytes for lithium-based rechargeable batteries." *Chemical reviews* 104.10 (2004): 4303-4418.
[60] Pinson, Matthew B., and Martin Z. Bazant. "Theory of SEI formation in rechargeable batteries: capacity fade, accelerated aging and lifetime prediction." *Journal of the Electrochemical Society* 160.2 (2012): A243.
[61] Cheng, Xin-Bing, et al. "Toward safe lithium metal anode in rechargeable batteries: a review." *Chemical reviews* 117.15 (2017): 10403-10473.

[62]] Li, Sa, et al. "Developing high-performance lithium metal anode in liquid electrolytes: challenges and progress." *Advanced Materials* 30.17 (2018): 1706375.
[63] An, Seong Jin, et al. "The state of understanding of the lithium-ion-battery graphite solid electrolyte interphase (SEI) and its relationship to formation cycling." *Carbon* 105 (2016): 52-76.
[64] Wang, Aiping, et al. "Review on modeling of the anode solid electrolyte interphase (SEI) for lithium-ion batteries." *npj Computational Materials* 4, 15 (2018).
[65] Verma, Pallavi, Pascal Maire, and Petr Novák. "A review of the features and analyses of the solid electrolyte interphase in Li-ion batteries." *Electrochimica Acta* 55.22 (2010): 6332-6341.
[66] Takahashi, T. "Early history of solid state ionics." *MRS Online Proceedings Library (OPL)* 135 (1988).
[67] Zhang, Bingkai, et al. "Mechanisms and properties of ion-transport in inorganic solid electrolytes." *Energy Storage Materials* 10 (2018): 139-159.
[68] Ma, Qianli, and Frank Tietz. "Solid-State Electrolyte Materials for Sodium Batteries: Towards Practical Applications." *ChemElectroChem* 7.13 (2020): 2693-2713.
[69] Fleischer, Michael. "The abundance and distribution of the chemical elements in the earth's crust." *Journal of Chemical Education* 31.9 (1954): 446.
[70] Thackeray, Michael M. "Manganese oxides for lithium batteries." *Progress in Solid State Chemistry* 25.1-2 (1997): 1-71.
[71] Mai, Liqiang, et al. "Nanoflakes-Assembled Three-Dimensional Hollow-Porous V_2O_5 as Lithium Storage Cathodes with High-Rate Capacity." *Small* 10.15 (2014): 3032-3037.
[72]] Lee, Ji Hoon, et al. "Superlattice Formation of Crystal Water in Layered Double Hydroxides for Long-Term and Fast Operation of Aqueous Rechargeable Batteries." *Advanced Energy Materials* 8.18 (2018): 1703572.
[73] Young, Matthias J., et al. "Discovery of anion insertion electrochemistry in layered hydroxide nanomaterials." *Scientific reports* 9, 2462 (2019).
[74] Alfaruqi, Muhammad Hilmy, et al. "A layered δ-MnO_2 nanoflake cathode with high zinc-storage capacities for eco-friendly battery applications." *Electrochemistry Communications* 60 (2015): 121-125.
[75] Su, Dawei, and Guoxiu Wang. "Single-crystalline bilayered V_2O_5 nanobelts for high-capacity sodium-ion batteries." *ACS nano* 7.12 (2013): 11218-11226.
[76] Wang, Na, et al. "Reversible (De) Intercalation of Hydrated Zn^{2+} in Mg^{2+}-Stabilized V_2O_5 Nanobelts with High Areal Capacity." *Advanced Energy Materials* 10.41 (2020): 2002293.
[77] Yin, Qing, et al. "CoFe–Cl Layered Double Hydroxide: A New Cathode Material for High-Performance Chloride Ion Batteries." *Advanced Functional Materials* 29.36 (2019): 1900983.
[78] Yin, Qing, et al. "High-performance, long lifetime chloride ion battery using a NiFe–Cl layered double hydroxide cathode." *Journal of Materials Chemistry A* 8.25 (2020): 12548-12555.
[79] Yan, Lijin, et al. "Modulating the electronic structure and pseudocapacitance of δ-MnO_2 through transitional metal M (M= Fe, Co and Ni) doping." *Electrochimica Acta* 306 (2019): 529-540.
[80] Kim, Hyunjin, et al. "Effects of Ni doping on the initial electrochemical performance of vanadium oxide nanotubes for Na-ion batteries." *ACS applied materials & interfaces* 6.14 (2014): 11692-11697.

[81] Shan, Xiaoqiang, et al. "Framework Doping of Ni Enhances Pseudocapacitive Na-Ion Storage of (Ni) MnO_2 Layered Birnessite." *Chemistry of Materials* 31.21 (2019): 8774-8786.
[82] Guyomard, D., et al. "New amorphous oxides as high capacity negative electrodes for lithium batteries: the Li_xMVO_4 (M= Ni, Co, Cd, Zn; $1< x\leqslant 8$) series." *Journal of Power Sources* 68.2 (1997): 692-697.
[83] Yang, Gongzheng, et al. "Self-assembly of $Co_3V_2O_8$ multilayered nanosheets: controllable synthesis, excellent Li-storage properties, and investigation of electrochemical mechanism." *ACS nano* 8.5 (2014): 4474-4487.
[84] Shen, Laifa, et al. "Mesoporous $NiCo_2O_4$ nanowire arrays grown on carbon textiles as binder‐free flexible electrodes for energy storage." *Advanced Functional Materials* 24.18 (2014): 2630-2637.
[85] Zhang, Yufei, et al. "Binary metal oxide: advanced energy storage materials in supercapacitors." *Journal of Materials Chemistry A* 3.1 (2015): 43-59.
[86] Mai, Liqiang, et al. "Nanowire electrodes for electrochemical energy storage devices." *Chemical reviews* 114.23 (2014): 11828-11862.
[87] Shi, Yanmei, et al. "Recent advances in nanostructured transition metal phosphides: synthesis and energy-related applications." *Energy & Environmental Science* 13.12 (2020): 4564-4582.
[88] Balogun, Muhammad-Sadeeq, et al. "Recent advances in metal nitrides as high-performance electrode materials for energy storage devices." *Journal of materials chemistry A* 3.4 (2015): 1364-1387.
[89] Kulkarni, Pranav, et al. "Nanostructured binary and ternary metal sulfides: synthesis methods and their application in energy conversion and storage devices." *Journal of Materials Chemistry A* 5.42 (2017): 22040-22094.
[90] Cheng, Xin-Bing, et al. "Sulfurized solid electrolyte interphases with a rapid Li^+ diffusion on dendrite-free Li metal anodes." *Energy Storage Materials* 10 (2018): 199-205.
[91] Xu, Wu, et al. "Lithium metal anodes for rechargeable batteries." *Energy & Environmental Science* 7.2 (2014): 513-537.
[92] Flamme, Benjamin, et al. "Guidelines to design organic electrolytes for lithium-ion batteries: environmental impact, physicochemical and electrochemical properties." *Green Chemistry* 19.8 (2017): 1828-1849.
[93] Yang, Huijun, et al. "Recent progress and perspective on lithium metal anode protection." *Energy Storage Materials* 14 (2018): 199-221.
[94] Ma, Qiang, et al. "Improved cycling stability of lithium-metal anode with concentrated electrolytes based on lithium (fluorosulfonyl)(trifluoromethanesulfonyl) imide." *ChemElectroChem* 3.4 (2016): 531-536.
[95] Qian, Jiangfeng, et al. "High rate and stable cycling of lithium metal anode." *Nature communications* 6, 6362 (2015).
[96]] Li, Shuo, et al. "Recent progress on electrolyte additives for stable lithium metal anode." *Energy Storage Materials* 32 (2020): 306-319.
[97] De las Casas, Charles, and Wenzhi Li. "A review of application of carbon nanotubes for lithium ion battery anode material." *Journal of Power Sources* 208 (2012): 74-85.
[98] Nguyen, Tuyen, and M. Fátima Montemor. "γ-FeOOH and amorphous Ni–Mn hydroxide on carbon nanofoam paper electrodes for hybrid supercapacitors." *Journal of Materials Chemistry A* 6.6 (2018): 2612-2624.

[99] Qu, Qunting, Shubin Yang, and Xinliang Feng. "2D sandwich-like sheets of iron oxide grown on graphene as high energy anode material for supercapacitors." *Advanced materials* 23.46 (2011): 5574-5580.
[100] Wei, Guijuan, et al. "Integrated FeOOH nanospindles with conductive polymer layer for high-performance supercapacitors." *Journal of Alloys and Compounds* 728 (2017): 631-639.
[101] Génin, Jean-Marie R., et al. "Thermodynamic equilibria in aqueous suspensions of synthetic and natural Fe (II)− Fe (III) green rusts: Occurrences of the mineral in hydromorphic soils." *Environmental Science & Technology* 32.8 (1998): 1058-1068.
[102] Tamaura, Yutaka, Takashi Yoshida, and Takashi Katsura. "The synthesis of green rust II (Fe^{III}_1–Fe^{II}_2) and its spontaneous transformation into Fe_3O_4." *Bulletin of the Chemical Society of Japan* 57.9 (1984): 2411-2416.
[103] Refait, Ph, and J-MR Génin. "The oxidation of ferrous hydroxide in chloride-containing aqueous media and Pourbaix diagrams of green rust one." *Corrosion science* 34.5 (1993): 797-819.
[104] Ona-Nguema, Georges, et al. "Iron (II, III) hydroxycarbonate green rust formation and stabilization from lepidocrocite bioreduction." *Environmental science & technology* 36.1 (2002): 16-20.
[105] Williams, Aaron GB, and Michelle M. Scherer. "Kinetics of Cr (VI) reduction by carbonate green rust." *Environmental Science & Technology* 35.17 (2001): 3488-3494.
[106] O'Loughlin, Edward J., et al. "Reduction of uranium (VI) by mixed iron (II)/iron (III) hydroxide (green rust): formation of UO_2 nanoparticles." *Environmental science & technology* 37.4 (2003): 721-727.
[107] Wang, Hailiang, et al. "An ultrafast nickel–iron battery from strongly coupled inorganic nanoparticle/nanocarbon hybrid materials." *Nature communications* 3, 917 (2012).
[108]] Liu, Jilei, et al. "A flexible alkaline rechargeable Ni/Fe battery based on graphene foam/carbon nanotubes hybrid film." *Nano letters* 14.12 (2014): 7180-7187.
[109] Chen, Ying-Chu, et al. "Novel iron oxyhydroxide lepidocrocite nanosheet as ultrahigh power density anode material for asymmetric supercapacitors." *Small* 10.18 (2014): 3803-3810.
[110] Hurlbutt, Kevin, et al. "Prussian blue analogs as battery materials." *Joule* 2.10 (2018): 1950-1960.
[111] Padhi, Akshaya K., Kirakodu S. Nanjundaswamy, and John B. Goodenough. "Phospho-olivines as positive-electrode materials for rechargeable lithium batteries." *Journal of the electrochemical society* 144.4 (1997): 1188.
[112] You, Ya, et al. "High-quality Prussian blue crystals as superior cathode materials for room-temperature sodium-ion batteries." *Energy & Environmental Science* 7.5 (2014): 1643-1647.
[113] Nai, Jianwei, and Xiong Wen Lou. "Hollow structures based on prussian blue and its analogs for electrochemical energy storage and conversion." *Advanced Materials* 31.38 (2019): 1706825.
[114] Zhang, Wei-Jun. "Structure and performance of $LiFePO_4$ cathode materials: A review." *Journal of Power Sources* 196.6 (2011): 2962-2970.
[115] Wang, Jiajun, and Xueliang Sun. "Understanding and recent development of carbon coating on $LiFePO_4$ cathode materials for lithium-ion batteries." *Energy & Environmental Science* 5.1 (2012): 5163-5185.
[116] Zhu, Yujie, et al. "Comparison of electrochemical performances of olivine NaFePO 4 in sodium-ion batteries and olivine $LiFePO_4$ in lithium-ion batteries." *Nanoscale* 5.2 (2013): 780-787.

[117] Oh, Seung-Min, et al. "Reversible $NaFePO_4$ electrode for sodium secondary batteries." *Electrochemistry communications* 22 (2012): 149-152.
[118]] Majzlan, Juraj, et al. "Thermodynamics of Fe oxides: Part I. Entropy at standard temperature and pressure and heat capacity of goethite (α-FeOOH), lepidocrocite (γ-FeOOH), and maghemite (γ-Fe_2O_3)." *American Mineralogist* 88.5-6 (2003): 846-854.
[119] Holzwarth, Uwe, and Neil Gibson. "The Scherrer equation versus the'Debye-Scherrer equation'." *Nature nanotechnology* 6.9 (2011): 534-534.
[120] P. Scherrer, "Bestimmung der Grosse und der inneren Struktur von Kolloidterilchen mittels Rontgestrahlen," *Nachrichten von der Gesellschaft der Wissenschaften zu Göttingen, Math. Klasse*, (26) 1918: 98–100.
[121] Nath, Debojyoti, Fouran Singh, and Ratan Das. "X-ray diffraction analysis by Williamson-Hall, Halder-Wagner and size-strain plot methods of CdSe nanoparticles-a comparative study." *Materials Chemistry and Physics* 239 (2020): 122021.
[122] Amaral, S. T., and I. L. Muller. "Effect of silicate on passive films anodically formed on iron in alkaline solution as studied by electrochemical impedance spectroscopy." *Corrosion* 55.01 (1999).
[123]] Salasi, M., et al. "The electrochemical behaviour of environment-friendly inhibitors of silicate and phosphonate in corrosion control of carbon steel in soft water media." *Materials Chemistry and Physics* 104.1 (2007): 183-190.
[124] Lahodny-Šarc, O., and L. Kaštelan. "The influence of pH on the inhibition of corrosion of iron and mild steel by sodium silicate." *Corrosion Science* 21.4 (1981): 265-271.
[125] Toby, Brian H., and Robert B. Von Dreele. "*GSAS-II*: the genesis of a modern open-source all purpose crystallography software package." *Journal of Applied Crystallography* 46.2 (2013): 544-549.
[126] Lebedev, Yu A., et al. "X-ray powder diffraction study of polytetrafluoroethylene." *Crystallography Reports* 55.4 (2010): 609-614.
[127] Kang, Weimin, et al. "Fabrication of porous Fe_2O_3/PTFE nanofiber membranes and their application as a catalyst for dye degradation." *RSC advances* 6.39 (2016): 32646-32652.
[128] Wyckoff, R.W. G.. "Crystal Structures", New York, *Interscience Publishers*, 1963.
[129] Shan, Xiaoqiang, et al. "Framework Doping of Ni Enhances Pseudocapacitive Na-Ion Storage of (Ni)MnO_2 Layered Birnessite." *Chemistry of Materials* 31.21 (2019): 8774-8786.
[130] Lindström, Henrik, et al. "Li^+ ion insertion in TiO_2 (anatase). 1. Chronoamperometry on CVD films and nanoporous films." *The Journal of Physical Chemistry B* 101.39 (1997): 7710-7716.
[131] Amann-Winkel, Katrin, et al. "X-ray and neutron scattering of water." *Chemical reviews* 116.13 (2016): 7570-7589.
[132] Hura, Greg, et al. "Water structure as a function of temperature from X-ray scattering experiments and ab initio molecular dynamics." *Physical Chemistry Chemical Physics* 5.10 (2003): 1981-1991.
[133]] Simon, Lilian, et al. "Structure of the Fe(II-III) layered double hydroxysulphate green rust two from Rietveld analysis." *Solid State Sciences* 5.2 (2003): 327-334.
[134] Solano, Eduardo, et al. "Neutron and X-ray diffraction study of ferrite nanocrystals obtained by microwave-assisted growth. A structural comparison with the thermal synthetic route." *Journal of applied crystallography* 47.1 (2014): 414-420.
[135] Patrat, G., et al. "Structure locale de δ-FeOOH." *Acta Crystallographica Section B: Structural Science* 39.2 (1983): 165-170.

[136] Gualtieri, Alessandro F., and Paolo Venturelli. "In situ study of the goethite-hematite phase transformation by real time synchrotron powder diffraction." *American Mineralogist* 84.5-6 (1999): 895-904.
[137]] Momma, Koichi, and Fujio Izumi. "VESTA 3 for three-dimensional visualization of crystal, volumetric and morphology data." *Journal of Applied Crystallography* 44.6 (2011): 1272-1276.
[138] Fujii, Tatsuo, et al. "In situ XPS analysis of various iron oxide films grown by NO_2-assisted molecular-beam epitaxy." *Physical review B* 59.4 (1999): 3195.
[139] Yamashita, Toru, and Peter Hayes. "Analysis of XPS spectra of Fe^{2+} and Fe^{3+} ions in oxide materials." *Applied surface science* 254.8 (2008): 2441-2449.
[140] Li, Yibo, et al. "An ultra-long life aqueous full K-ion battery." *Journal of Materials Chemistry A* 9.5 (2021): 2822-2829.
[141] Zuo, Wenhua, et al. "A Novel Phase‐Transformation Activation Process toward Ni-Mn-O Nanoprism Arrays for 2.4 V Ultrahigh-Voltage Aqueous Supercapacitors." *Advanced Materials* 29.36 (2017): 1703463.
[142] Qin, Haigang, et al. "V_2O_5 hollow spheres as high rate and long life cathode for aqueous rechargeable zinc ion batteries." *Electrochimica Acta* 306 (2019): 307-316.

APPENDIX: LIST OF PUBLICATIONS

Book chapter

- **Guo, Fenghua**, Nivedita Gupta, and Xiaowei Teng. "Enhancing Pseudocapacitive Process for Energy Storage Devices: Analyzing the Charge Transport Using Electro-kinetic Study and Numerical Modeling." *Supercapacitors: Theoretical and Practical Solutions* 87 (2018).

Peer-Reviewed Journal Articles

- Charles, Daniel S., **Fenghua Guo**, Xiaoqiang Shan, SaeWon Kim, Zachary W. Lebens-Higgins, Wenqian Xu, Dong Su, Louis FJ Piper, and Xiaowei Teng. "Dual-stage K^+ ion intercalation in V_2O_5-conductive polymer composites." *Journal of Materials Chemistry. A* 9 (2021): 15629-15636.
- Shan, Xiaoqiang, **Fenghua Guo**, Daniel S. Charles, Zachary Lebens-Higgins, Sara Abdel Razek, Jinpeng Wu, Wenqian Xu et al. "Structural water and disordered structure promote aqueous sodium-ion energy storage in sodium-birnessite." *Nature Communications* 10, 4975 (2019).
- Shan, Xiaoqiang, **Fenghua Guo**, Katharine Page, Joerg C. Neuefeind, Bruce Ravel, AM Milinda Abeykoon, Gihan Kwon, Daniel Olds, Dong Su, and Xiaowei Teng. "Framework Doping of Ni Enhances Pseudocapacitive Na-Ion Storage of (Ni)MnO_2 Layered Birnessite." *Chemistry of Materials* 31, 21 (2019): 8774-8786.
- Shan, Xiaoqiang, **Fenghua Guo**, Wenqian Xu, and Xiaowei Teng. "High purity Mn_5O_8 nanoparticles with a high overpotential to gas evolution reactions for high voltage aqueous sodium-ion electrochemical storage." *Frontiers in Energy* 11, 3 (2017): 383-400.